東京大学　大学院新領域創成科学研究科 基盤科学研究系物質系専攻
平成２１年度　修士論文

Transport properties of embedded $LaTiO_3$ layers
- $LaTiO_3$界面における輸送特性 -

２０１０年1月２６日提出
指導教員：Mikk Lippmaa　准教授

086008：大塚　怜奈

Contents

Chapter 1

Introduction

1.1 General Introduction

1.1.1 Interfaces in materials

Interfaces, which are formed between two different materials or two different phases, have many interesting physical properties, such as the formation of quantum wells and are therefore at the center of attention as subjects for research. Most interface studies have been done with Si and other semiconductors. Interfaces are widely used by the semiconductor industry in electronic devices with Si-based transistors being the most widely used interface-based devices without which present-day life would be difficult to imagine. However, limitations of size and performance, and the desire to integrate more functions in microelectronic circuits, have moved interest beyond traditional semiconductors to other, more versatile materials, such as oxides.

1.1.2 Interfaces in oxide materials

Many of the interesting properties found in oxide materials, especially among the transition metal oxides, are related to various forms of ordering, such as magnetic order, charge order or orbital order due to the strongly correlated nature of electrons. Such correlated electron materials are being studied by many research groups. Oxides have presented the physics community with surprising and difficult physics problems. For example, the mechanism of high-temperature superconductivity is still not understood, more than two decades after the materials were discovered. In addition to problems of physics, oxides also offer the potential to contribute to be development of new types

of electronic devices. Due to the rich electronic phase diagram of many oxides, it is likely that some of the phase transitions that are known, can also be used for practical purposes, for example for data storage or as sensors. For applied work, therefore, interest has among others focused on oxide materials and heterostructures that exhibit very large magnetoresistive effects, which may be useful for developing higher-density magnetic storage devices. However, it has been recognized in recent years that translating known bulk properties of oxides into actual functioning devices is surprisingly difficult. The reason for this is partly hinted at by the same richness of electronic phases that make oxides so attractive in the first place. Small structural or composition changes can dramatically alter the physical properties of many oxides. Unfortunately for device design, this also means that the materials are extremely sensitive to defects, such as oxygen loss or the presence of various crystal defects.

For many device applications of oxides, it is necessary to use thin films. This means that the effects of interfaces and surfaces have to be considered when material properties are measured or devices are designed. This work is based on the understanding that it is practically impossible to grow thin films and oxide heterostructures that would yield a perfect single-crystal-like structure. This is partly due to the kinetic nature of thin film growth processes and partly due to intrinsic structural or electronic reconstruction phenomena that occur at interfaces. It is therefore critically important to study particular interface structure and account for the additional effects that occur in these semi two-dimensional structures. In many cases, it is actually appropriate to view such thin heterostructures or interface regions as separate compounds, where the properties of the individual materials that make up a heterostructures can only be used as an approximate guide to the expected properties.

Some spectacular examples of this can be seen among recent works on truly 2-dimensional oxide heterostructures, e.g. $LaAlO_3$ / $SrTiO_3$ [1] and Nb doped $SrTiO_3$ /$SrTiO_3$ [2]. These works have generated strong interest in interface phenomena in oxides and may provide the guiding light needed to design actual useful oxide electronic devices in the future.

The appearance of different electronic phases in oxides is often closely related to the number of carriers in the material [Fig. 1.1] [3]. Various techniques exist to control the carrier density, with chemical doping being the most common. In addition to bulk doping, however, there are various other ways to change the carrier density. For example, field effect, photocarrier injection, charge transfer at interfaces, and nanoscale carrier confinement. It is therefore very interesting to study the effect of variable carrier

density on the properties of oxide heterostructure with the aim of controlling electronic ordering.

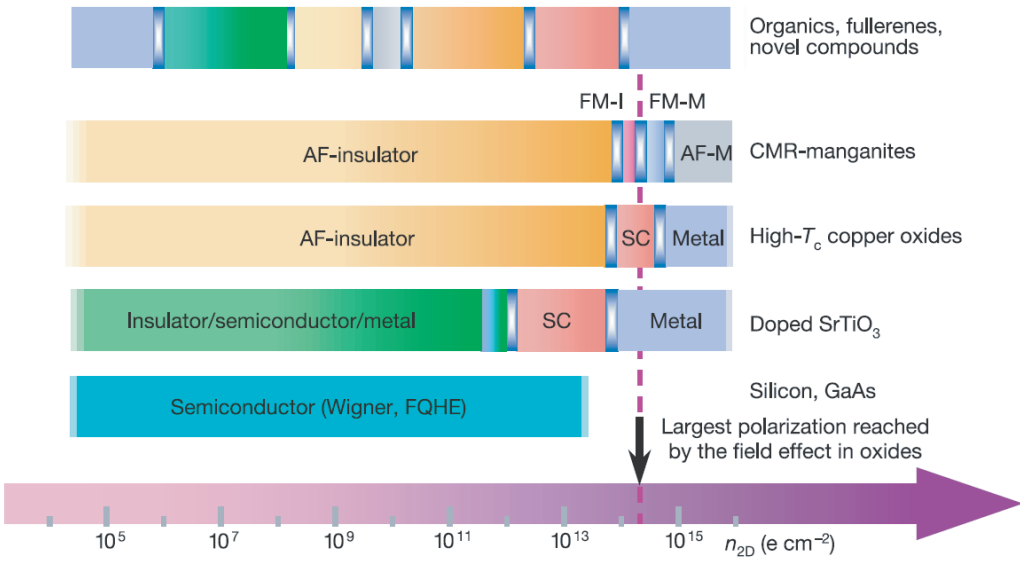

Figure 1.1: Illustration of the zero-temperature behavior of various correlated materials as a function of sheet charge density (n_{2D}). The example for high-T_c superconductors and for colossal magnetoresistance (CMR) manganites reflect $YBa_2Cu_3O_{7-\delta}$ and (La, Sr)MnO_3, respectively. AF, antiferomagnetic; FM, ferromagnetic; I, insulator; M, metal; SC, superconductor; FQHE, fractional quantum Hall effect; Wigner, Wigner crystal [3].

1.2 Scope of this thesis

In this study, the focus is on the $LaTiO_3$ / $SrTiO_3$ system. Recent theoretical works have shown that this type of heterostructure may support various forms of electronic ordering [4, 5]. Experimental evidence, however, is still lacking. The aim is to make the epitaxial oxide interface and study the possibility of tuning the carrier density and electronic phases in $LaTiO_3$ / $SrTiO_3$ heterostructures by changing temperature or applying magnetic or electric fields to have an evidence of existing the various phase at interface.

1.3 Outline

The outline of the thesis is the following. In Chapter 2, physical properties and a brief overview of earlier research on the materials used in this thesis work are described. Chapter 3 is devoted to the presentation of the main experimental equipment and techniques for fabricating and characterizing oxide heterostructures. Chapter 4 contains fabrication details of thin films grown by PLD. In the subsequent three Chapters, transport measurement results are shown and discussed. Temperature dependence of transport properties are in Chapter 5. In Chapter 6, resistivity behavior under magnetic field is presented together with analysis based on the multiple layer model. Finally, the possibility of conductivity in the $SrTiO_3$ capping layer is discussed in Chapter 7. A brief summary and conclusions can be found in Chapter 8.

References

[1] A. Ohtomo and H. Y. Hwang *Nature* **427**, 423 (2004).

[2] Y. Kozuka, M. Kim, C. Bell, B. G. Kim Y. Hikita and H. Y. Hwang *Nature* **462**, 487 (2009).

[3] C. H. Ahn, J. -M. Triscone and J. Mannhart *Nature* **424**, 1015 (2003).

[4] S. Okamoto, A. J. Mills and N. A. Spaldin *Physical Review Letters* **97**, 056802 (2006).

[5] R. Pentcheva and W. E. Pickett *Physical Review Letters* **99**, 016802 (2007).

Chapter 2

Physical properties of materials

This Chapter describes the physical properties of materials which were used in this study. The characteristic properties and earlier research on properties of $SrTiO_3$ are presented in the first section. The second Section is devoted to discussing the properties of $LaTiO_3$ bulk crystals and thin films. After that, a brief summary of other published work on $LaTiO_3$ / $SrTiO_3$ interfaces is reviewed. At last, the characteristic properties of two oxide materials which were used as capping layers are discussed.

2.1 $SrTiO_3$

$SrTiO_3$ is the most popular material as a substrate for growing epitaxial oxide thin films due to the availability of high quality single crystals and its interesting physical properties. $SrTiO_3$ has the perovskite crystal structure, which is shown in Fig. 2.1. The perovskite structure is usually expressed as ABO_3, where A is a rare-earth ion and B is a transition metal. As many other oxides, the crystal can be viewed as a repeating sequence of layers, in this case consisting of AO planes and BO_2 planes. In spite of this simple structure, in an electronic sense, perovskites form a group of materials with surprisingly varied properties and complex behavior. Among the best known properties that have prompted extensive research efforts are supercoductivity, magnetoresistance, ferroelectricity, etc. Our focus is on perovskites mainly because the same basic structure allows layers with different compositions in the AO and BO_2 layers to be easily combined, forming interesting heterostructures.

Nondoped $SrTiO_3$ is an insulator with a wide band gap of 3.2 eV. [1] The basic band structure is quite simple, as shown in Fig. 2.2. It shows the valence band, which has an oxygen $2p$ character and an empty conduction band with titanium $3d$ character. This

picture, however, is complicated by ease with which carriers can be doped in $SrTiO_3$, for example by replacing Ti with Nb [2] or Sr with La [3], by creating oxygen vacancies, and by field effect. In all of these cases, metallic conductivity appears.[4]. Even slight doping, in the $10^{17}cm^{-3}$ range, can turn the material into a semiconductor, metal or even a superconductor.[5] This is possible because the Fermi Level of intrinsic $SrTiO_3$ is located close to the bottom of the conduction band. Due to this, slightly doped $SrTiO_3$ shows a metallic phase. Partly because the metallic conduction appears at very low doping levels, Hall mobility of carriers can be very high, with 10^4 $cm^2V^{-1}s^{-1}$ being common at low temperature. It is possible to have very high Hall mobility in doped $SrTiO_3$ bulk crystals at low temperature but it is quite difficult to obtain such Hall mobilities with carriers doped in $SrTiO_3$ films or interfaces between oxide materials and $SrTiO_3$ bulk. In recent works, a few research groups have observed the Shubnikov-de Haas (SdH) oscillations, which is possible only for high Hall mobility 2-dimensional systems, notably in the $LaAlO_3$ / $SrTiO_3$ system [6] and in Nb: $SrTiO_3$ / $SrTiO_3$ heterostructures[2].

For these reasons, $SrTiO_3$ has attracted a great deal of research effort.

2.2 $LaTiO_3$

$LaTiO_3$ is another oxide with a perovskite structure, structurally similar to $SrTiO_3$. It is well known that the physical properties of $LaTiO_x$ for $(3 \leq x \leq 3.5)$ are very sensitive to the exact oxygen content [7]. the phase diagram of bulk $LaTiO_3$ has been studied quite well. It is known that $LaTiO_3$ shows several different phases, such as semiconducting, metallic and ferroelectric insulator at room temperature.[7] The lattice parameters also change with oxygen content in bulk $LaTiO_x$ [8]. Moreover $LaTiO_3$ is known to be a Mott insulator containing Ti^{3+}, and shows weak ferromagnetism below 140 K when oxygen contents is between about 3.0 and 3.1 [9]. Slight doping by introducing extra oxygen causes an immediate disappearance of the Mott gap and results in metallic conductivity.

When oxygen content in $LaTiO_x$ reaches 3.5, electronic properties evolve from a Mott insulator (Ti^{3+}) to a band insulator (Ti^{4+}) which can be written as a distinct phase, $La_2Ti_2O_7$. $La_2Ti_2O_7$ has a monoclinic structure and a stable ferroelectric phase [7]. It is an insulating oxide.

Especially in thin film studies, stoichiometric $LaTiO_3$ is difficult to grow because an extremely reducing atmosphere is needed. During the initial growth stage, the first few monolayers of $LaTiO_3$ can be formed due to a stabilizing effect of epitaxial lattice

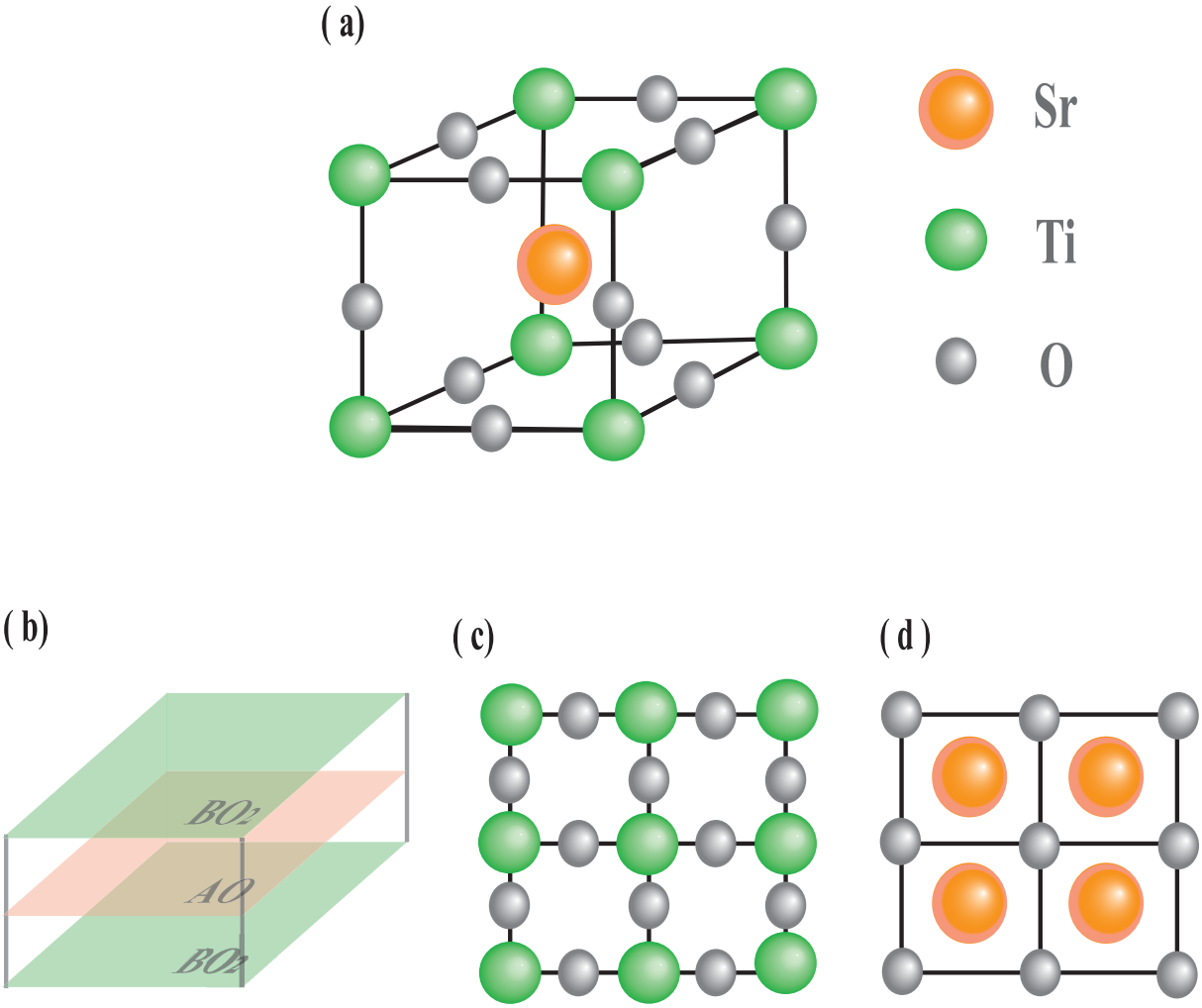

Figure 2.1: (a) ABO_3 perovskite crystal structure, using $SrTiO_3$ as an example. $SrTiO_3$ has cubic structure and lattice parameter is ~ 3.905 $\dot{A}$. (b) possible terminating planes of the (001) surface, in this case A-site is Strontium and B-site is Titanium, (c) TiO_2-terminated surface and (d) SrO-terminated surface.

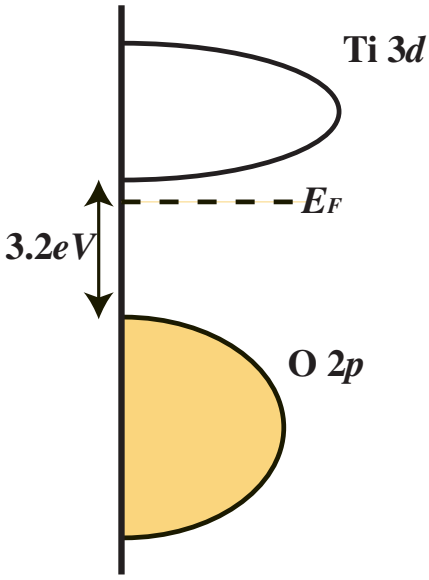

Figure 2.2: Band structure of $SrTiO_3$

strain from the $SrTiO_3$ substrate. In thicker layers, however, $La_2Ti_2O_7$ phase starts to form [10].

Moreover, this materials can be doped not only by changing oxygen stoichiometry but also by substituting Sr onto La sites. $Sr_{1-x}La_xTiO_3$ shows metallic behavior even for $x = 0.95$, as shown in Fig. 2.3 [3] due to filling of the $3d$ electron conduction band [11].

2.3 $LaTiO_3$ / $SrTiO_3$ heterostructure

The physical properties of a Mott insulator $LaTiO_3$ and a band insulator $SrTiO_3$, which have many interesting properties on their own, were introduced in the above sections. Several groups have also studied the properties of $LaTiO_3$ / $SrTiO_3$ heterostructures and superlattices. The justification is usually to study the electronic state at an interface between a Mott insulator material and a band insulator material. It has been predicted and observed that such heterostructures can behaves quite differently from the corresponding bulk materials and may exhibit typical correlated electron properties such as colossal magnetoresistance.

Based on calculations, Okamoto *et al.* showed that various ordered phase may exist in the $LaTiO_3$ / $SrTiO_3$ superlattices [Fig. 2.4]. The rich phase diagram is due to the effect of the large ferroelectric-like distortions of the TiO_6 octahedra, which

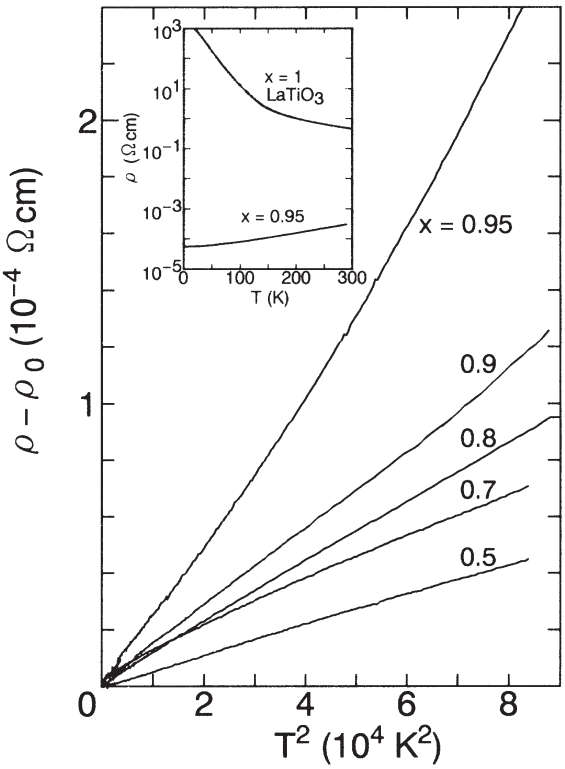

Figure 2.3: Resistivity of $Sr_{1-x}La_xTiO_3$ bulk [3]

substantially affect the Ti *d*-electron density [12]. In addition to magnetic phases, charge disproportionation, or charge ordering, has been suggested by Pentcheva *et al.* to occur at the interfaces of ideal $LaTiO_3$ / $SrTiO_3$ superlattices [Fig 2.5]. The charge-ordered phase would avoiding highly charged d^0 ions being nearest neighbors [13].

In experiments, Ohtomo *et al.* observed that the distribution of extra electrons can be seen in a fractional Ti^{3+} signal [Fig. 2.6]. It was suggested that the Ti sites exhibit mixed valence between 3+ and 4+ [14].

These reports have shown the a large difference in physical properties existes between bulk materials, films, and interfaces, even when the same component materials are used.

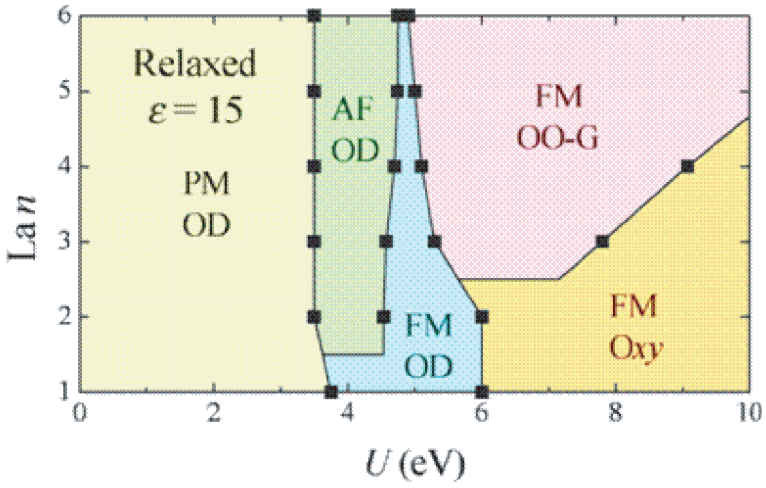

Figure 2.4: Spin and orbital phase diagram of $[LaTiO_3]_n$ / $SrTiO_3$ superlattices [12]

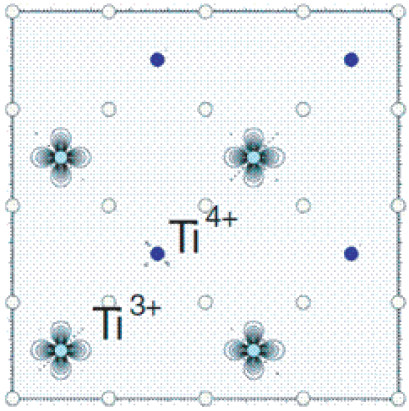

Figure 2.5: Charge density distribution of the occupied 3*d* states in the charge-ordered TiO_2 layer [13]

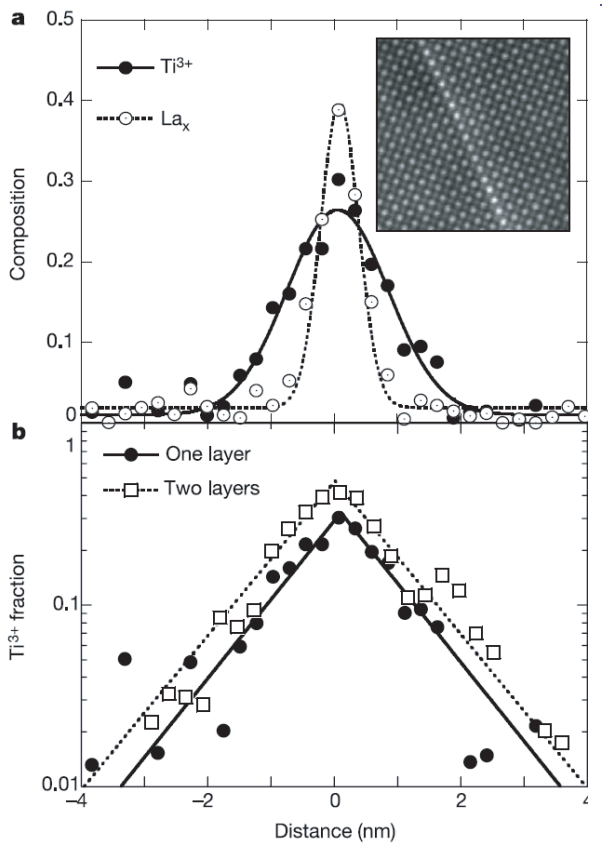

Figure 2.6: Spatial distribution of the Ti^{3+} signal in **a** the vicinity of the $LaTiO_3$ layer and **b** bilayer [14]

2.4 $CaHfO_3$

$CaHfO_3$ was used as a capping layer film in some of the heterostructures used in this study. $CaHfO_3$ has an orthorhombic structure with $a = 0.5719$, $b = 0.7982$, and $c = 0.5578$ nm. The pseudocubic unit cell has on average a 2.3 % lattice mismatch with $SrTiO_3$ but it can still be grown epitaxially on $SrTiO_3$ substrates. For this reason, and due to its relatively high dielectric constant and wide gap, it has been used as a gate insulator for field effect transistor [15]. The band gap of $CaHfO_3$ is not well defined, especially in thin films but estimated based on the values published for HfO_2 put the gap width above 5eV [16].

2.5 $BaTiO_3$

$BaTiO_3$ is another cap layer material used in this work, in addition to $CaHfO_3$ and $SrTiO_3$. The lattice mismatch with $SrTiO_3$ is approximately 2.4 % in bulk case. When $BaTiO_3$ is grown epitaxially on $SrTiO_3$, it forms a strained film for layer thicknesses below about 10 nm [17]. $BaTiO_3$ has almost the same band-gap as $SrTiO_3$ (3.2 eV). The band gap depends on the composition for compounds where the A site consists of a mixture of Ba and Sr atoms, $Ba_xSr_{1-x}TiO_3$ [18]

References

[1] J. A. Norland *Physical Review Letters* **94**, 724 (1954).

[2] Y. Kozuka, M. Kim, C. Bell, B. G. Kim Y. Hikita and H. Y. Hwang *Nature* **462**, 487 (2009).

[3] Y. Tokura, Y. Taguchi, Y. Okada, Y. Fujimori, T. Arima, K. Kumagai and Y. Iye *Physical Review Letters* **70**, 2126 (1993).

[4] K. Shibuya, T. Ohnishi, T. Uozumi, M. Lippmaa and H. Koinuma *Thin Solid Films* **486**, 195 (2005).

[5] C. H. Ahn, J. -M. Trisconr and J. Mannhart *Nature* **424**, 1015 (2003).

[6] A. Ohtomo and H. Y. Hwang *Nature* **427**, 423 (2004).

[7] F. Lichtenberg, D. Widmer, J. G. Bednorz, T. Williams and A. REeler *Z. Phycs. B - COndenced Matter*, **82**, 211 (1991).

[8] D. A. Maclean, Hok-Kam NG and J. E. Greedan *Journal of Solid State Chemistry* **30**, 35 (1979).

[9] Y. Taguchi, T. Okuda, M. Ohashi, C. Murayama, N. Mori, Y. Iye and Y. Tokura *Physical Review B* **59**, 7917 (1999).

[10] A. Ohtomo, D. A. Muller, J. L. Grazul and H. Y. Hwang *Applied Physics Letters* **80**, 3922 (2002).

[11] Y. Fujishima, Y. Tokura, T. Arima and S. Uchida *Physical Review B* **46**, 11167 (1992).

[12] S. Okamoto, A. J. Mills and N. A. Spaldin *Physical Review Letters* **97**, 056802 (2006).

[13] R. Pentcheva and W. E. Pickett *Physical Review Letters* **99**, 016802 (2007).

[14] A. Ohtomo, D. A. Muller, J. L. Grazul and H. Y. Hwang *Nature* **419**, 378 (2002).

[15] K. Shibuya, T. Ohnishi, T. Uozumi, T. Sato, M. Lippmaa, M. Kawasaki, K. Nakajima T. Chikyow and H. Koinuma *Applied Physics Letters* **88**, 212116 (2006).

[16] J. Robertso *Journal of Vacuum Science and Technology B* **18**, 1785 (2000).

[17] H. Terauchi, Y. Watanabe, H. Kasatani, K. Kamigaki, Y. Yano and T. Terashima *Journal of The Physical Society of Japan* **61**, 2194 (1992).

[18] K. Ohara, T. Ohsawa, H. Koinuma and Y. Matsumoto *Japanese Journal of Applied Physics* **45**, L339 (2006).

Chapter 3

Equipment and techniques

This Chapter described the fabrication and the characterization of oxide thin films used in this study. All oxide thin films were fabricated by pulsed laser deposition (PLD). Reflection High-Energy Electron Diffraction (RHEED) and a stylus profilometer (Dektak) were used for estimating the film thickness. The atomic-scale structure of the surface of the films was analyzed with atomic force microscopy (AFM) and scaning tunneling microscopy (STM). Conductivity of the films under magnetic field were measured with a physical property measurement system (PPMS).

3.1 Pulsed laser deposition

3.1.1 PLD instrumentation

There are several techniques that can be used to deposit atomic or molecule scale layers in vacuum on a solid surface. These can be roughly divided into two types, chemical vapor deposition (CVD) and physical vapor deposition (PVD). CVD is a good process for industrial use because it is possible to deposit homogeneous films on large areas and the deposition rate is fast. In contrast, PVD involves the formation of a physical vapor in vacuum, such as plasma sputtering or high temperature vacuum evaporation. It is easy to grow high-quality and multilayer films. Pulsed laser deposition is the one of the PVD techniques. It is a widely used technique and it is particularly suitable for growing multi-component and multilayer oxide structures and high-quality functional oxide films.Moreover, PLD is an efficient thin film growth technique for oxides, many of which have very high melting points and contain many different elements in a unit cell. Many oxide studies have been done by growing

films by PLD. However, the PLD technique is known to have various limitations as well, especially in terms of experimental reproducibility [1]. The main reason for this may be the difficulty in reproducing the growth conditions, such as the ablation laser conditions, the substrate temperature and oxygen pressure etc. Among those parameters, the ablation laser fluence is found to have a very strong effect on the lattice constant and crystal structure [2].

In this study, the films were fabricated by the PLD system illustrated in Fig. 3.2. The PLD system has a pulsed KrF excimer laser with a wavelength of 248 nm and a pulse duration time of approximately 20 ns (ThinFilmStar, TuiLaser [Fig. 3.3]). The KrF excimer laser is used to ablate the oxide targets [Fig. 3.4] that may have very high melting points. The excimer laser light is introduced into the chamber, which is pumped by a turbo molecular pump (TMP) backed by rotary pumps to achieve a base pressure below 1×10^{-8} Torr. The laser enters the vacuum chamber through a synthetic quartz window and is focused onto the target surface. In order to avoid fast erosion of the target surface, the targets are continuously scanned by computer-controlled stepping motors so as to ablate evenly the whole surface of the target. To control the oxygen stoichiometry of films and kinetic and thermodynamic conditions during growth, oxygen partial pressure is tuned by leak valves that supply the O_2 gas into vacuum.

The substrate was clamped on a sample holder made of stainless steel. Platinum paste was applied between a substrate crystal and a Ni block which is a part of the sample holder. The nickel insert was oxidized and absorbs infrared light from a heating laser. The nickel block effectively diminishes temperature variation over the sample surface and the platinum paste improves the thermal contact between the substrate crystal and the nickel block. The substrate-target distance can be chosen according to experimental needs. In most experiments, a distance of about 54 mm was used. The chamber also had a set of masks that could be inserted in front of the sample crystal in order to limit the film growth to a specific region on the substrate surface. The masks were mounted on computer-controlled linear drives. In this work, the masking system was used to grow samples with linear film thickness gradients. A diode laser (λ = 808 nm) was used for substrate heating. The substrate temperature was monitored with an optical pyrometer.

The advantage of using a laser for sample heating is the high maximum temperature that can be reached (up to 1300°C) and rapid heating/cooling, which is possible due to the low heat capacity of the sample holder. Laser heating also helps to maintain a

clean chamber and a low background pressure because the heat source is outside of the chamber, so miniaturization of the chamber is possible and homogeneous heating is achieved.

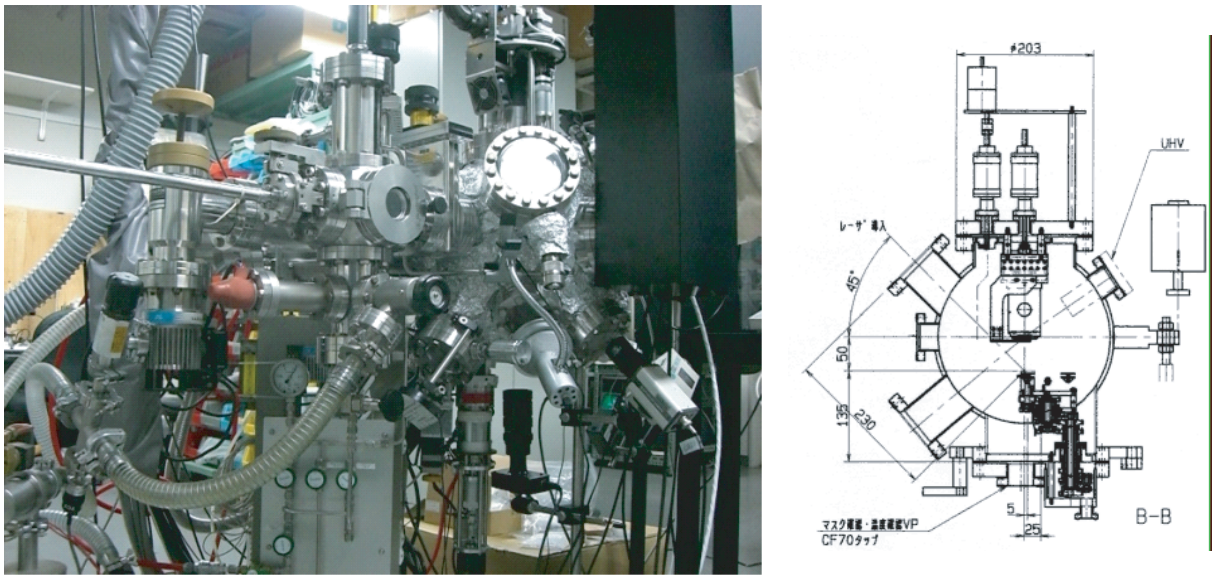

Figure 3.1: Overview of the PLD chamber

3.1.2 Reflection high-energy electron diffraction (RHEED)

The PLD system has a reflection high-energy electron diffraction (RHEED) system for surface analysis. It is used for in situ monitoring of growth dynamics and for atomic-level growth control [Fig. 3.5]. A special feature of this RHEED system is the ability to scan the electron beam across the sample surface under computer control. The RHEED gun was differentially pumped, and could be used at oxygen pressures of up to 1 mTorr. The electron beam energy used in this RHEED gun was approximately 25 keV. The electron beam touches the sample at an angle that is typically in the range of 0.5 to 2.5 degrees. The electron beam is scattered from the sample surface and forms a diffraction pattern on a phosphor screen. The image is captured with a high-sensitivity CCD camera and analyzed in real time on an attached computer. The RHEED patterns on the phosphor screen are very sensitive to the topmost surface of the material. Moreover during layer-by-layer deposition, oscillations of the RHEED intensity are observed since the RHEED intensity strongly depends on the surface roughness. In this growth mode, one layer is essentially completed before material

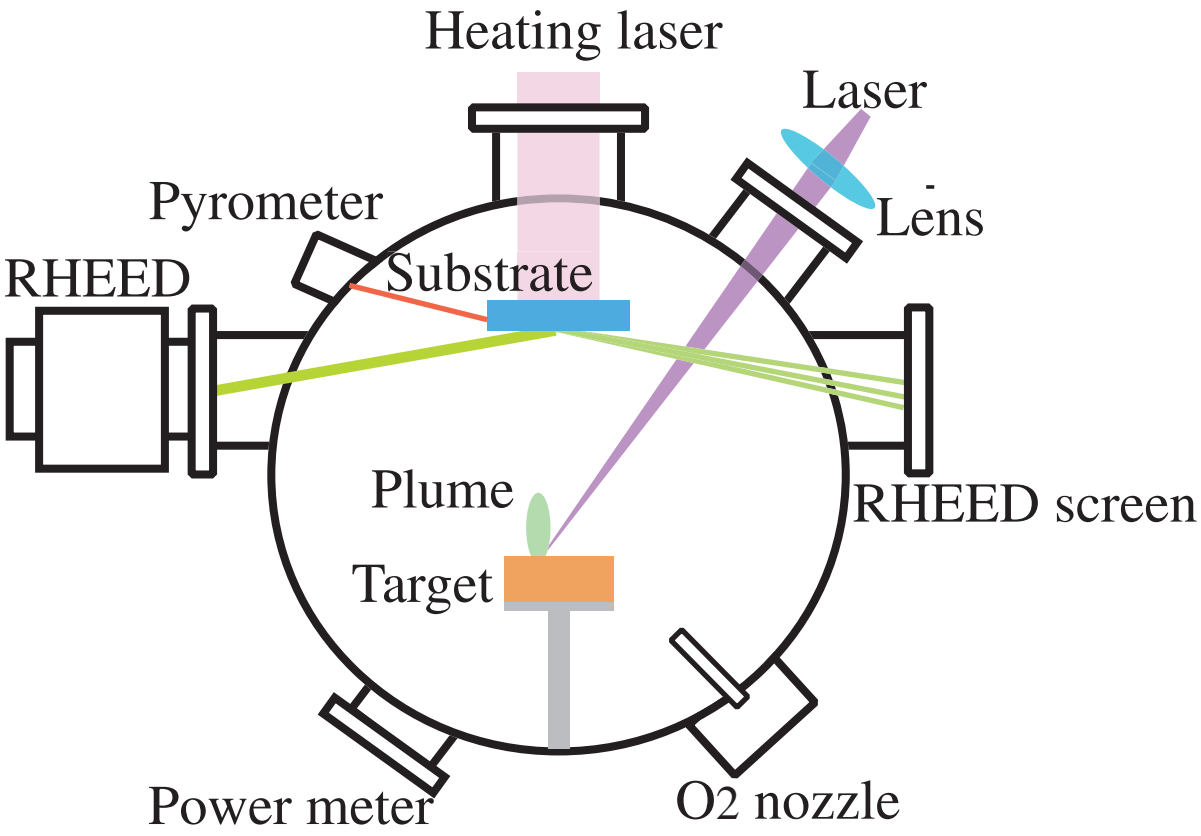

Figure 3.2: Schematic illustration of the PLD apparatus

Figure 3.3: KrF excimer laser

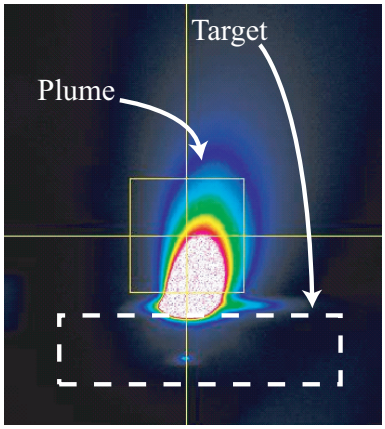

Figure 3.4: Plume image

is added to the following layer. This periodic variation of the surface morphology is generally accepted as the reason for RHEED oscillations [3]. In reality, the RHEED intensity can be strongly affected by other features, for example, the incident angle of the electron beam changing the phase of the RHEED oscillation dramatically [4]. However, the number of oscillations can still provide useful information on he thickness of the films during deposition.

In this study, the number of unit cells deposited for very thin layers was determined by counting oscillations observed in the RHEED specular beam intensity.

3.2 Measurement of surface properties

3.2.1 Atomic force microscopy

Atomic force microscopy (AFM) is one of the scanning probe microscopy techniques that is used to measure the surface morphology of samples with a nanometer-scale accuracy. In this method, the surface height information is obtained by keeping the force between a sharp tip and the sample surface constant while the tip is scanned in a raster over the surface. The feedback signal is used to construct a topographic image of the surface. The functioning of the microscope is illustrated in Fig. 3.6.[5] In a basic AFM setup, the sharp probe needle has a tip radius of about 10 nm and it is attached to a flexible cantilever. A piezoelectric drive is used to scan either the tip or the sample so that the tip can be placed anywhere within a rectangular scan area. The height of the tip is measured optically, by detecting the deflection of the elastic cantilever as the

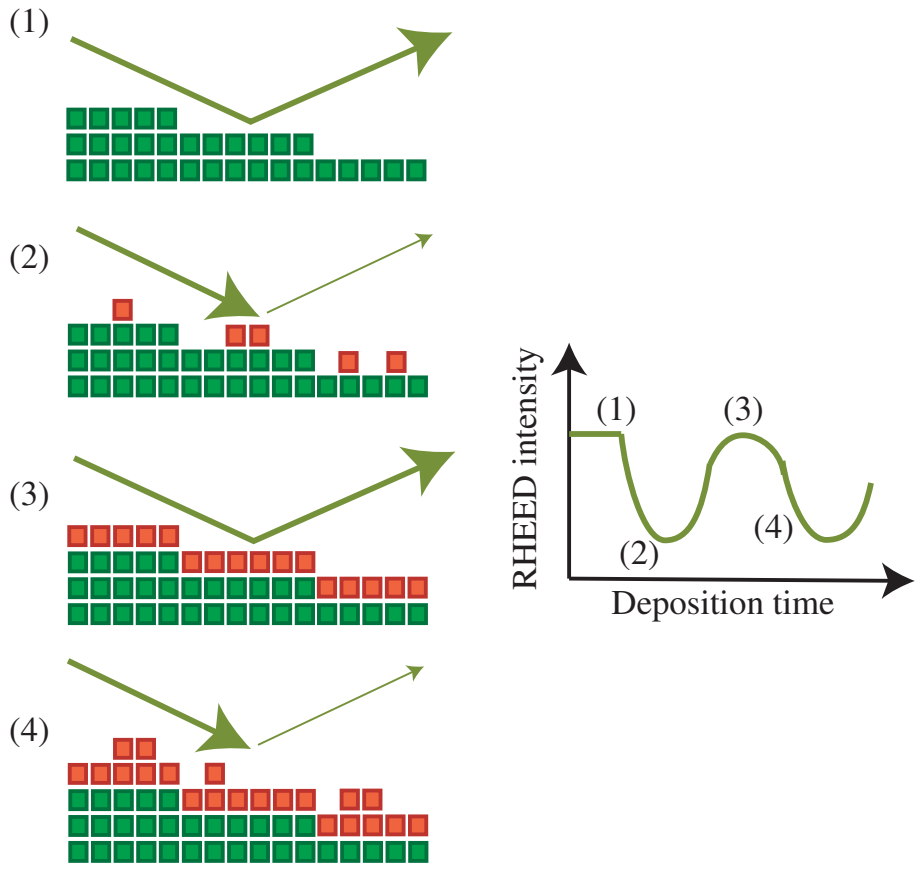

Figure 3.5: Schematic surface structures during layer-by-layer growth and RHEED intensity oscillations as a function of the deposition time

tip moves up or down. The optical detection is done with a segmented photodiode that can detect both vertical and lateral movement of the reflected light beam, where the vertical motion is used to determine the height signal and the lateral motion can be used to construct a simultaneous friction force image. The friction force image is useful for detecting chemical changes on the surface.

In this study, a SPM9600 (Shimadzu) microscope was used to measure the sample surface morphology. In order to obtain higher resolution surface morphology information, a dynamic force mode (DFM) was used. This is a non-contact measurement mode. In a DFM measurement, the probe needle is also placed on a flexible cantilever, and the cantilever is vibrated by external oscillating force. As the AFM needle approaches the sample surface, the amplitude of the cantilever vibration decreases due to the interaction between the needle and the sample. The segmented photodetector detects the

vibration amplitude, and a horizontal scan is performed while keeping the amplitude constant. The resolution of the system is determined by the diameter of the tip and it is routinely possible to achieve a spatial resolution of about 10 nm. A big advantage of AFM is that the sample does not need to be conducting and therefore it was used to measure the morphology of all films used in this study.

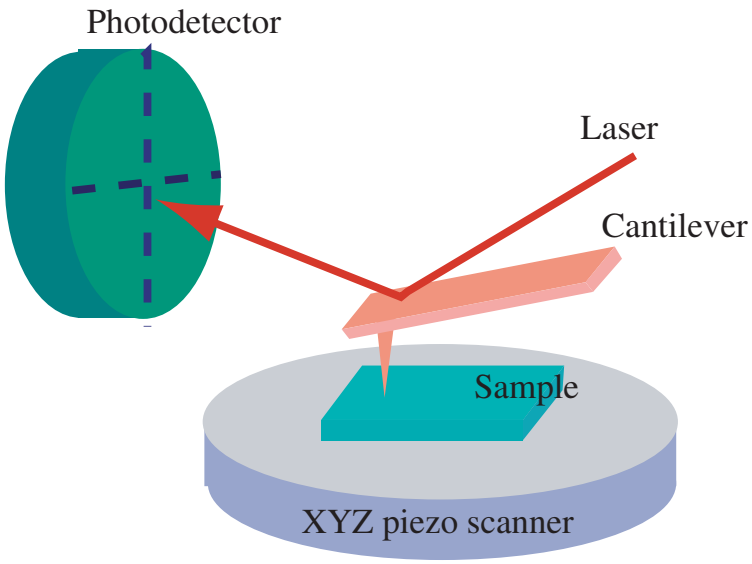

Figure 3.6: Schematic illustration of the AFM

3.2.2 Scanning tunneling microscopy (STM)

Scanning tunneling microscopy (STM) is another scanning probe microscopy technique that is used to measure the atomic scale morphology on a surface. The resolution of an image is much better than with AFM. For clean surfaces, it is possible to obtain atomic resolution. The STM is based on the effect of quantum tunneling between atoms on the tip and surface [Fig. 3.7]. When the conducting tip is brought close enough to the surface, a bias applied between the tip and the sample can allow electrons to tunnel between them. Because of this, STM can measure only conductive samples. A piezoelectric drive is used to keep the constant tunnel current and scan either the tip or the sample so that the tip can be placed anywhere within a rectangular scan area. Although an STM can detect even less than 1 pm surface roughness it should be remembered that an STM measures the electronic density of the surface and can not be guaranteed to show the actual configuration of atoms on the surface.[5].

In this study, the STM measurements were done with the help of Prof. Komori's group. For STM measurements, a 0.05 wt.% Nb-doped $SrTiO_3$ substrate was used instead of a normal nondoped $SrTiO_3$ crystal.

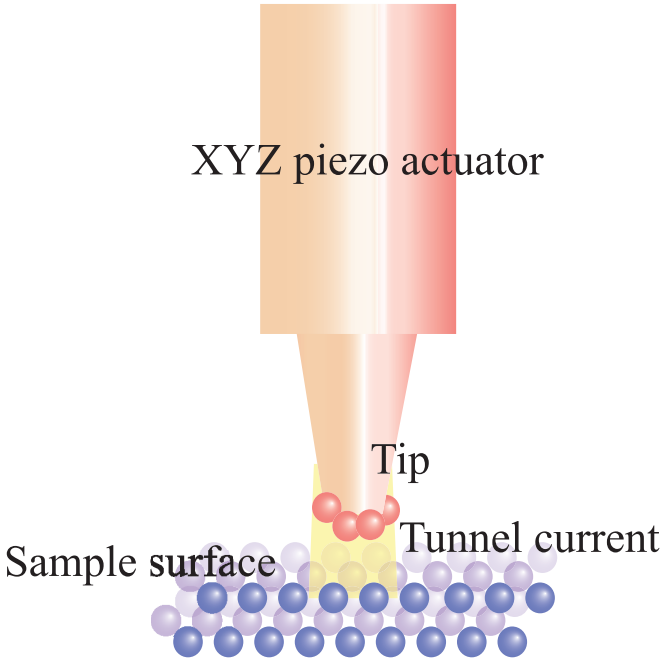

Figure 3.7: Schematic illustration of the STM

3.3 Transport measurements

3.3.1 Resistance and Hall measurement

The resistance and Hall effect were measured by the commonly-used four probe measurement technique. In some cases, such as gradient samples, where a 4-point geometry was not practical, 2-point measurements were used. Ohmic contacts to the samples were made by aluminum wire using ultrasonic wire bonding.

The resistance and Hall voltage measurements of the samples were done at various temperatures and magnetic fields. To control these conditions, a superconducting magnet cryostat (Physical Property Measurement System, PPMS : Quantum Design Inc.) was used. The main measurement conditions in this study were: temperature 5 K to 300 K and magnetic field 0 T to ±5 T. A few measurements were also performed at lower temperatures, down to 2 K and up to 7 T, also in PPMS [Fig. 3.8].

Figure 3.8: PPMS

Hall bar shape

Hall bar shapes were formed by a mechanical milling machine (FP-21T : MITS Electronics Inc.) [Fig. 3.9]. Since it is very easy to induce metallic conductivity in $SrTiO_3$, it is difficult to find a surface patterning technique that does not result in extrinsic conduction paths close to a Hall bar. If the Hall bar were formed with normal lithography technique, $SrTiO_3$ substrate would need to be etched, usually by ion milling. This would result in a conducting surface layer [6]. For avoiding $SrTiO_3$ conductivity, a mechanical milling technique was used. This milling machine allows cuts to be made with a cutting path width of down to approximately 50 μm.

Another important point for measuring Hall effect is the shape of the Hall bar. Two basic geometries can be used for performing Hall measurements: a bridge or a (usually)square sample. In the latter case, as long as the electrodes are placed on the edge of the sample area, any shape can be used, but a symmetric configuration is preferred. The sample must be free of geometrical holes for contact. A bridge-type specimen needs extensions out of the bridge for electrode attachment. For other geometries, like the van der Pauw technique, the contacts should be point contacts located symmetrically on the periphery. There is always some error in electrode placement and this can affect Hall resistance measurements. To simplify contact placement, most measurements were done with bridge-shaped samples that had 6 arms [7]. The 6 arm type bridge Hall

bars were cur in the sample surface by mechanical milling technique [Fig. 3.10].

Figure 3.9: Desk top type milling processing machine : MITS

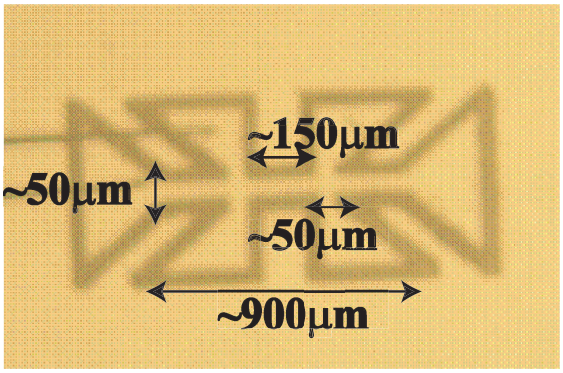

Figure 3.10: Hall bar on a crystal surface

References

[1] T. Ohnishi, H. Koinuma and M. Lippmaa *Applied Surface Science* **252**, 2466 (2006).

[2] T. Ohnishi, M. Lippmaa, T. Yamamoto, S. Meguro and H. Koinuma *Applied physics letters* **87**, 241919 (2005).

[3] W. Braun *Applied RHEED -Refraction High-Energy Electron Diffraction During Crystal Growth* (2004).

[4] T. Ohnishi and M. Lippmaa *Surface Science* **28**, 223 (2007).

[5] C. Kittel *Introduction to Solid State Physics*.

[6] J. H. Nagi. Y. Segal, F. J. Walker, S. Ismail-Beigi, K. Le Hur and C. H. Ahn *Condmat material*, arXiv:0909.2834v1 (2009).

[7] D. K. Schroder *SEMICONDUCTOR MATERIAL AND DEVICE CHARACTERIZATION*.

Chapter 4

Sample fabrication

This Chapter describes the procedure and details of fabricating the oxide thin films that were used in this study. Selection of growth conditions is an extremely important factor for growing films or heterostructures with the desired physical properties. The PLD technique in general is known for limited experimental reproducibility [1]. The main reason for this is the difficulty in reproducing the growth conditions. Among the more difficult parameters to control are the ablation laser conditions, and the substrate temperature. Other parameters, such as oxygen pressure, are easier to set accurately. The PLD system used in this study has been designed to allow accurate laser power density control. Due to this, in the experiments described in this work, the growth rate is also under accurate control. The largest source of uncertainty is probably the growth temperature. Most thin film samples, however, were grown at relatively low temperatures, where substrate temperature deviations are small. While being mindful of such experimental difficulties, the growth parameters were carefully optimized.

4.1 $SrTiO_3$ / $LaTiO_3$ / $SrTiO_3$ heterostructures

4.1.1 $SrTiO_3$ substrate

the thin film samples were grown on 0.2° miscut $SrTiO_3$ (100) single crystal substrates from Shinkosha Co. Ltd. The substrates were chemically etched by the vendor. The etching process is important, because it leads to surfaces that have atomically flat terraces and regular single unit cell steps.[2]. Another advantage of etching is that it helps to control the cation ratio at the surface of the substrate and thus reduces the variability that would otherwise be seen in the growth of very thin films. Sufficiently

smooth surfaces are also needed for depositing various oxide materials epitaxially, because the film quality depends on the surface quality of the substrate. Moreover the $SrTiO_3$ substrate surface by chemical etched were known to have TiO_2 termination [2]. The $SrTiO_3$ substrates as supplied were cleaned in acetone (5 min. ultrasonic agitation) to remove organic contamination from the surface.

Before deposition, the substrates were annealed at high temperature, typically at approximately 900 °C for 30 minutes in 10^{-6} Torr of oxygen. High-temperature annealing can remove contamination form the surface and also produces a smooth surface with straight step edges due to rapid migration of surface atmos [3, 4] and a regular terrace structure. The reason for using miscut substrates was to obtain a surface with regular step spacings. The annealed surfaces are mostly terminated by the TiO_2 atomic layer, although some segregates SrO is also present on the surface. [5]

In some cases 0.05 wt% Nb-doped $SrTiO_3$ substrate were also used. These substrates are metallic and can be used, among other things, for STM measurements. $LaTiO_3$ thin films with submonolayer coverage were deposited on the Nb-doped $SrTiO_3$ substrates annealed under the same conditions as the nondoped substrates. The growth conditions of the $LaTiO_3$ films were also the same as those used for fabricating all the other samples.

4.1.2 $LaTiO_3$ and $SrTiO_3$ deposition

$LaTiO_3$ films were deposited on $SrTiO_3$ substrates that had been treated as discussed in the previous Section. It is well known from published data that the physical properties of $LaTiO_x$ ($3 \leq x \leq 3.5$) are very sensitive to the exact oxygen content [6]. The literature on the growth of $LaTiO_3$ is very sparse. Even the synthesis of stoichiometric bulk $LaTiO_3$ is quite difficult, primarily due to the extremely reducing conditions necessary to stabilize Ti^{3+}. Only a few reports on the synthesis of bulk have been published [7]. A few research groups have reported the growth of $LaTiO_3$ films [8, 9] and Shibuya *et al.*. [10] have studied $LaTiO_3$ / $SrTiO_3$ superlattice structures grown under low oxygen pressures of 10^{-6} Torr using PLD. Ohtomo *et al.*. have also reported $LaTiO_3$ / $SrTiO_3$ superlattice growth, also at low oxygen partial pressure of 10^{-6} Torr [11].

In this work, a sintered $La_2Ti_2O_7$ target was used. This phase is stable and convenient for use as an ablation target. The deposition conditions were selected based on earlier published work on $LaTiO_3$ growth [Fig. 4.1][8]. $LaTiO_3$ films with an approximate thickness of 6 unit cells were grown under 10^{-6} Torr oxygen to avoid the formation of the insulating $La_2Ti_2O_7$ pahse. The excimer laser pulse rate was 2 Hz. Since the purpose was

to grow films in a layer-by-layer mode, the substrate temperature had to be relatively low. This also helps to stabilize the $LaTiO_3$ pahse. For initial growth test, the substrate temperature was set at either 500°C, 600°C or 700°C. The growth mode was verified to be layer-by-layer for all cases based on the time dependence of the RHEED specular reflection intensity [12]. AFM images of the film surfaces after $LaTiO_3$ deposition on annealed $SrTiO_3$ substrates are shown in Fig. 4.2. The surfaces mostly showed a step-and-terrace morphology, except for the sample grown at 700°C, which showed the presence of additional island-like features on the surface. This may be caused by the formation of the $La_2Ti_2O_7$ phase instead of $LaTiO_3$ at high temperature. Since the surface was no longer atomically flat, this growth temperature was not considered further and 500°C was chosen as the optimal deposition temperature for growing flat epitaxial $LaTiO_3$ films in this study.

All $LaTiO_3$ samples were grown at 500°C at an oxygen pressure of 10^{-6} Torr and an ablation laser fluence of 0.4 J/cm^2. This resulted in a growth rate of 46 pulses per unit cell when the laser was operated at 1 Hz. The deposition rate was checked by counting the number of RHEED specular spot intensity oscillations during growth and calibrating the growth rate determined from RHEED measurements against film thickness measurements performed by Dektak for thicker test films.

It is known that Sr vacancies can form in the $SrTiO_3$ substrate during high temperature annealing. Additionally, oxygen vacancies can form during film growth, even at low temperatures. Since oxygen vacancies in $SrTiO_3$ work as dopants, donating mobile carriers, it is necessary to eliminate the oxygen vacancies before the transport properties of the heterostructures can be measured. To fill the oxygen vacancies created during $LaTiO_3$ deposition, the films were post-annealed in a furnace in air at 400°C for 6 hours. However, it has been reported that $LaTiO_3$ / $SrTiO_3$ structures may show insulating behavior after annealing. It is unlikely that the annealing produces a perfect insulating $LaTiO_3$ phase. In general, it would be expected that Sr segregation in the substrate would lead to a slight Sr doping of the interface layer. This would be expected to result in a conducting (La,Sr)TiO_3 layer at the interface. And the observed insulating behavior may be caused by two mechanisms: the formation of the $La_2Ti_2O_7$ phase during the oxidizing post anneal, and the presence of a surface depletion layer that is commonly observed in thin oxide films.[14] To avoid these problems, an approximately 25 unit cell thick $SrTiO_3$ film was grown on top of the $LaTiO_3$ heterostructure as a protective capping layer [Fig. 4.3] [13]. The final structure thus contains a continuous titanate perovskite lattice, where only the *A* site cation is varied between Sr (in the substrate

and the cap layer) and La (in the interface layer). Since the role of the cap layer was to protect the heterostructure, it was necessary to suppress conductivity in the cap layer. To do this, the $SrTiO_3$ capping layer was also deposited at 500°C at an oxygen pressure of 10^{-6} Torr. The cap layer was deposited immediately after growing the $LaTiO_3$ film, using the same ablation conditions as for $LaTiO_3$ film. The laser fluence for $SrTiO_3$ capping layer deposition was approximately 0.4 J/cm^2, giving a growth rate of roughly 28 pulses per $SrTiO_3$ unit cell. The laser pulse rate was increased to 2 Hz. It is known that it is actually very difficult to grow $SrTiO_3$ films with bulk-like mobilities. In most cases, unoptimized growth of $SrTiO_3$ leads to films that are flat, but electronically very dirty. The $SrTiO_3$ films grown under the same conditions as $LaTiO_3$, was thus considered to be a perfect capping layer that would not contribute significantly to the heterostructure transport properties at low temperature.

Finally after all depositions were done, the films on were post-annealed in air at 400°C for 6 hours.

4.2 $CaHfO_3$ deposition for capping layer

Although the $SrTiO_3$ capping layer was grown at conditions that were far from optimal for $SrTiO_3$ growth, the capping layer may still affect the conductivity of the $LaTiO_3$ / $SrTiO_3$ substrate interface. Different capping layer materials were therefore considered. One possibility was to use $CaHfO_3$ films. This material is known to be a wide-gap insulator and thus cannot be doped to a conducting state by vacancies. Since $CaHfO_3$ has been used as a gate insulator for field effect transistor in the same research group previously, there was also extensive experience in growing $CaHfO_3$ films. It is known that despite a mismatch of about 2.3 % with $SrTiO_3$, thin $CaHfO_3$ layers can still be grown epitaxially on $SrTiO_3$ and the layers are reasonably flat [15, 16].

The $CaHfO_3$ cap layers were deposited under several conditions in this study to get a good insulating capping layer film. First, deposited was attempted under the same condition as the $SrTiO_3$ capping layer, at 500 °C substrate temperature, 10^{-6} Torr oxygen pressure, and a laser fluence of approximately 0.4 J/cm^2 at a laser pulse rate of 2 Hz. Under these conditions, there should be no change in the phase of the $LaTiO_3$ layer, as was the case for the growth of $SrTiO_3$ capping layer. For comparison, other cap layer samples was also grown under 10^{-5} Torr and 10^{-3} Torr of oxygen, while keeping the substrate temperature and laser conditions the same as for $SrTiO_3$.

After deposition, the films were post-annealed in air at 400 °C for 6 hours.

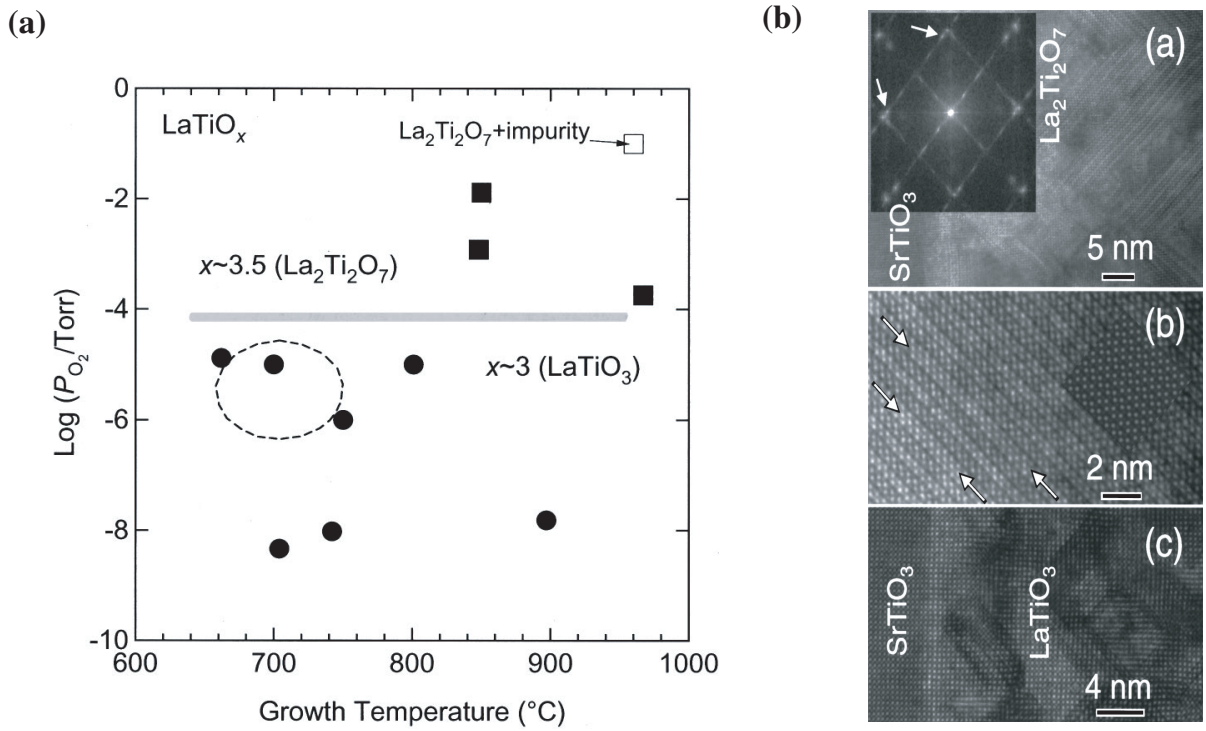

Figure 4.1: **(a)**: Growth phase diagram in terms of oxygen partial pressure and temperature for 200 nm thick $LaTiO_x$ films. **(b)**: Annular dark-field scanning transmission electron microscope images for $La_2Ti_2O_7$ (a) and (b), and $LaTiO_3$ (c) grown on (001) $SrTiO_3$ substrates taken along a $SrTiO_3$ [100] zone axis. Inset in (a) depicts a Fourier transform of the image, and the arrows indicate the tilting twin microstructure of $La_2Ti_2O_7$. Inset in (b) shows a simulated image obtained assuming the bulk structure. Stacking faults in the $La_2Ti_2O_7$ film are indicated by arrows [8]

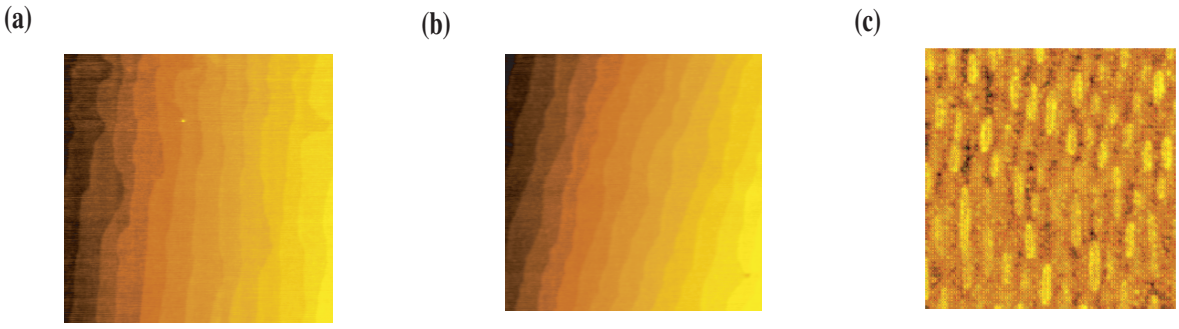

Figure 4.2: AFM surface images of $LaTiO_3$ films that were grown at different substrate temperatures: (a) 500°C, (b) 600°C and (c) 700°C

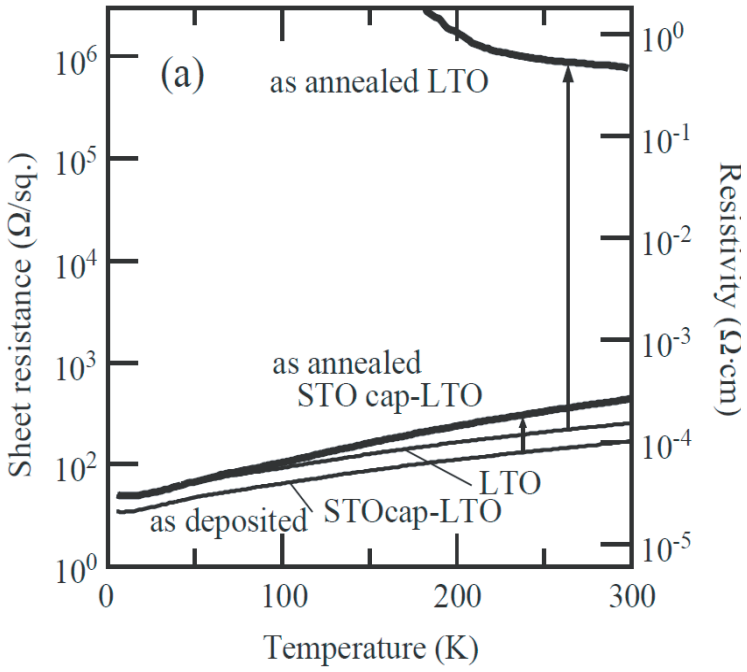

Figure 4.3: Resistivity of $LaTiO_3$ films on $SrTiO_3$ with $SrTiO_3$ capping layer and without a capping layer [13]

4.3 $BaTiO_3$ deposition for capping layer

Although the $CaHfO_3$ films are insulating and certainly do not contribute to conductivity, there is still a large mismatch with $SrTiO_3$ and additional Ca and Hf cations are introduced to the heterostructure. In order to maintain a continuous titanate sublattice and only vary the *A*-site composition, another insulating material, $BaTiO_3$ was also tried as a capping layer material instead of $SrTiO_3$. $BaTiO_3$ has almost the same band-gap energy as $SrTiO_3$. The lattice mismatch is approximately 2.4 percent, but it is known that epitaxial and strained $BaTiO_3$ can be grown on $SrTiO_3$ up to a thickness of about 10 nm.[17]

The $BaTiO_3$ cap layers were deposited at 500 °C under 10^{-6} Torr of oxygen and at a laser fluence of 0.4 J/cm^2. The growth rate was roughly 26 pulses per $BaTiO_3$ unit cell at a laser pulse rate of 2 Hz. These deposition condition were the same as those used for the growth of $SrTiO_3$ capping layers.

Films were also post-annealed at 400 °C for 6 hours in air after deposition to fill any oxygen vacancies formed in the films or the $SrTiO_3$ substrate.

References

[1] T. Ohnishi, H. Koinuma and M. Lippmaa *Applied Surface Science* **252**, 2466 (2006).

[2] M. Kawasaki, K. Takahashi, T. Maeda, R. Tsuchiya, M. Shinohara, O. Ishiyama, T. Yonezawa, M. Yoshimoto and H. Koinuma *Science* **266**, 1540 (1994).

[3] M. Lippmaa, M. Kawasaki, A. Ohtomo, T. Sato, M. Iwatsuki and H. Koinuma *Applied Surface Science* **130**, 582 (1998).

[4] M. Lippmaa, K. Tkahashi, A. Ohtomo, S. Ohashi, T. Ohnishi, N. Nakagawa, T. Sato, M. Iwatsuki, H. Koinuma and M. Kawasaki *Materials Science and Engineering* **B56**, 111 (1998).

[5] T. Ohnishi, K.Shibuya, M. Lippmaa, D. Kobayashi, H. Kumigashira, M. Oshima and H. Koinuma *Applied Physics Letters* **85**, 2 (2004).

[6] F. Lichtenberg, D. Widmer, J. G. Bednorz, T. Williams and A. REeler *Z. Phycs. B - COndenced Matter*, **82**, 211 (1991).

[7] M. Kestigian and R. Ward *Journal of the American Chemical Society* **76**, 6027 (1954).

[8] A. Ohtomo, D. A. Muller, J. L. Grazul and H. Y. Hwang *Applied Physics Letters* **80**, 3922 (2002).

[9] S. Havelia, K. R. Balasubramaniam, S. Spirgeon, F. Cormack and P. A. Salvador *Journal of Crystal Growth* **310**, 1985 (2008).

[10] K. Shibuya, T. Ohnishi, M. Kawasaki, H. Koinuma and M. Lippmaa *Japan Journal of Applied Physics* **43**, 1178 (2004).

[11] A. Ohtomo, D. A. Muller, J. L. Grazul and H. Y. Hwang *Nature* **419**, 378 (2002).

[12] M. Lipomaa, N. Nakagawa, M. Kawasaki S. Ohashi, Y. Inaguma, M. Itoh and H. Koinuma *Applied Physics Letters* **74**, 3543 (1999).

[13] T. Mihara, K. Shibuya, T. Ohnishi, H. Koinuma and M. Lippmaa *Thin Solid Films* **486**, 63 (2005).

[14] A. Ohtomo and H. Y. Hwang *Applied Physics Letters* **84**, 1716 (2004).

[15] K. Shibuya, T. ohnishi, T. Uozumi, H. Koinuma and M. Lippmaa *Applied Surface Science* **252**, 8147 (2006).

[16] K. Shibuya, T. Ohnishi, T. Uozumi, T. Sato, M. Lippmaa, M. Kawasaki, K. Nakajima T. Chikyow and H. Koinuma *Applied Physics Letters* **88**, 212116 (2006).

[17] H. Terauchi, Y. Watanabe, H. Kasatani, K. Kamigaki, Y. Yano and T. Terashima *Journal of The Physical Society of Japan* **61**, 2194 (1992).

Chapter 5

Temperature dependence of conductivity in $LaTiO_3$ / $SrTiO_3$

This Chapter describes the conductivity of $LaTiO_3$ layers embedded in $SrTiO_3$. The growth details of the heterostructures were detailed in Chapter 4. Particular attention in this Chapter is paid to the conductivity of fractional $LaTiO_3$ layer embedded in $SrTiO_3$, similar to the structures that have been proposed to give rise to ordered interface phases. As the doping layer thickness is reduced below a full unit cell coverage, it is not necessarily appropriate to consider such fractional layers as continuously doped quantum wells. Instead, possible spatial segregation, such as island formation, should also be considered. To address this issue, STM results of fractional $LaTiO_3$ layers are also included in this Chapter.

5.1 Introduction

It is known that there is a possibility of ordered electronic phases appearing at $LaTiO_3$ / $SrTiO_3$ interfaces, as discussed in Chapter 2. In addition to the two-dimensional geometry of a heterostructure, thin films also offer a way to tune the carrier density continuously within a single sample. It is therefore easier to study low doping level properties of the $La_xSr_{1-x}TiO_3$ system. Due to these reasons, it is interesting to make $La_xSr_{1-x}TiO_3$ films where x varies between 1 and 0 within a single interface layer. The idea is that a fractional $LaTiO_3$ layer could be deposited on a pre-annealed atomically flat step-and-terrace $SrTiO_3$ substrate. This would result in the formation of a doped $La_xSr_{1-x}TiO_3$ interface layer that has a physical thickness of a single unit cell [Fig. 5.1]. These experiments were also undertaken to determine the doping level where a two-

dimensional transition to an insulating state would occur on La-doped $SrTiO_3$. A critical doping level has been observed in earlier work for ultrathin $LaTiO_3$ layers by Mihara et al.. In general, metallic-like behavior was observed close to room temperature, followed by a sharp transition to an insulating state at temperatures ranging from 10 to 100 K [Fig. 5.2] [1].

The purpose was to map this transition behavior in more detail by using thickness or coverage-gradient heterostructures.

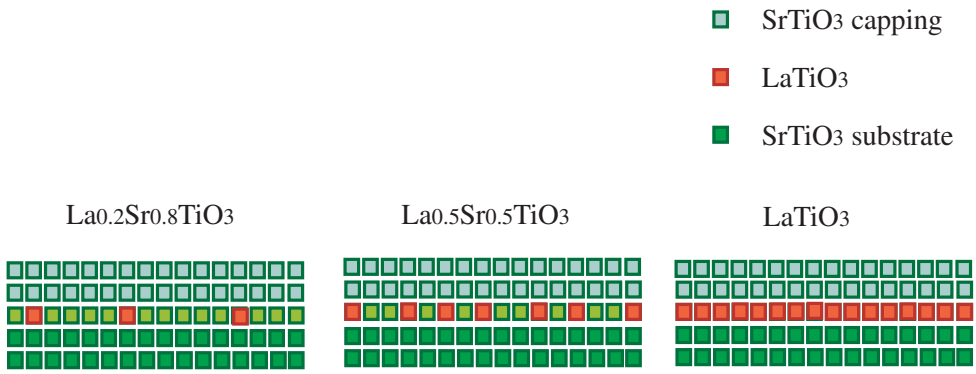

Figure 5.1: Structural cartoon of the assumed structure of fractional $LaTiO_3$ layers on an atomically flat pre-annealed $SrTiO_3$ substrate.

5.2 Experiment

The heterostructures were grown by PLD as described in Chapter 3. The $SrTiO_3$ (100) substrates were annealed at about 1000 °C to obtain flat terraces and approximately equidistant single unit cell steps. After annealing, a $LaTiO_3$ layer was deposited on the substrate. The growth conditions were shown in Chapter 4. The layer thickness was determined by monitoring RHEED specular spot intensity oscillations. Fig. 5.3 shows an example of RHEED intensity behavior during the growth of an approximately 0.4 unit cell $LaTiO_3$ layer. An AFM image of 0.5 unit cell $LaTiO_3$ layer on $SrTiO_3$ is shown in Fig. 5.4. It should be noted that the AFM image does not differ from an image of an annealed substrate surface. The AFM measurement was done in a dynamic force mode, where the phase shift experienced by the AFM tip would show a different contrast for surface regions that have different terminating chemistries, such as segregated La-rich islands on a $SrTiO_3$ surface. Such features are not visible after

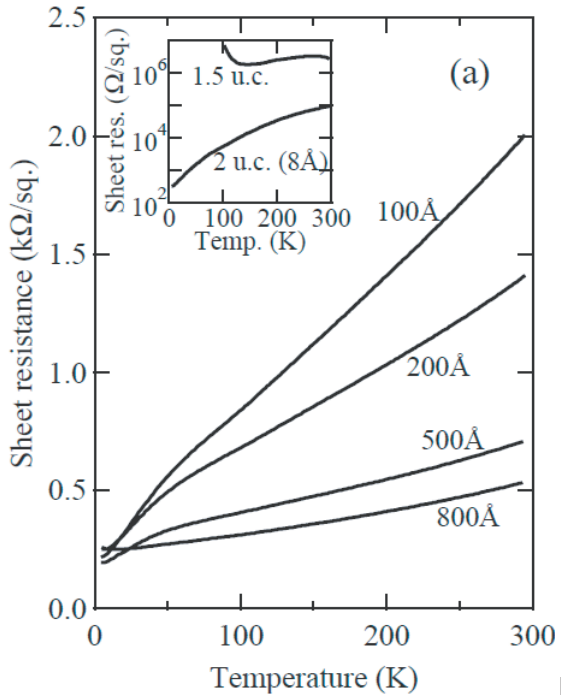

Figure 5.2: Sheet resistance of an ultra-thin $LaTiO_3$ layer on a pre-annealed $SrTiO_3$ [1]. The films were un-capped.

the deposition of a fractional $LaTiO_3$ layer. Considering that the growth temperature was relatively low, and looking at the RHEED intensity oscillation data, it is clear that the fractional $LaTiO_3$ layer corresponds to a classical nucleation layer of a layer-by-layer growth. The surface would thus be expected to be covered by a large number of very small, nanometer-scale islands. Since the AFM measurement spatial resolution is limited by the finite tip radius to about 10 nm, it is clear that such islands would not be resolved in an AFM image, and thus the 'atomically flat' morphology of the surface in Fig. 5.4 is deceptive. This point will be addressed later, when the AFM image is compared with a STM scan of a similar surface.

For transport measurement, samples were always postannealed and contact to the interface layer was made by ultrasonic wire bonding.

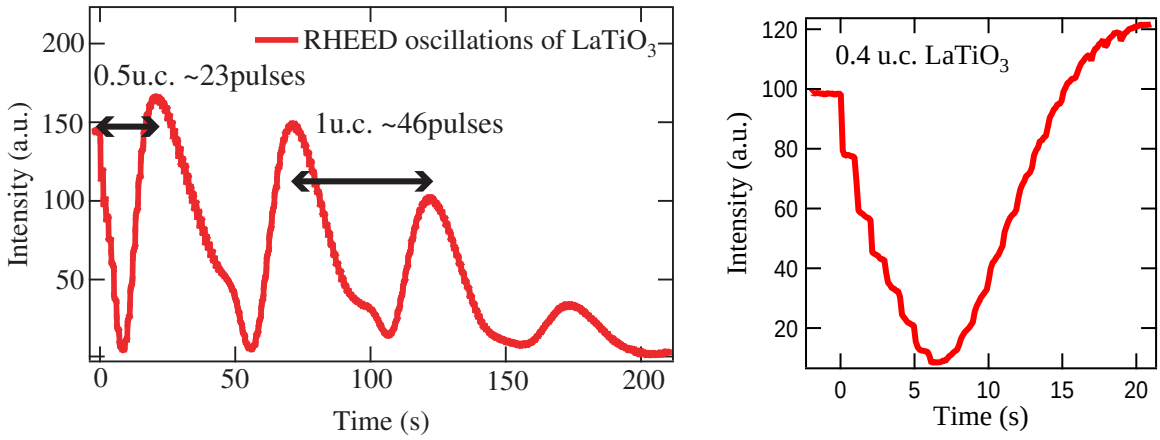

Figure 5.3: RHEED specular intensity oscillation during the initial growth of approximately 0.4 unit cell $LaTiO_3$ layer on a pre-annealed $SrTiO_3$ substrate surface.

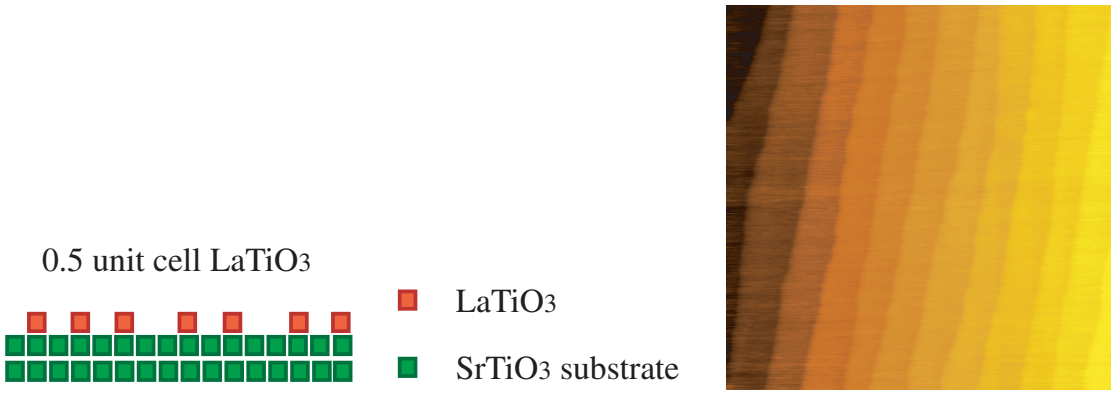

Figure 5.4: A cross-section diagram of the expected surface structure of a fractional $LaTiO_3$ layer and an AFM image of an approximately 0.5 unit cell $LaTiO_3$ layer on a pre-annealed $SrTiO_3$. The image was taken before cap layer deposition. Image size is 1 μm^2.

5.3 Results and discussion

Result of resistance measurement for a thickness gradient $LaTiO_3$ layer sample is shown in Fig 5.5. By using a moving mask in the deposition chamber during film growth, a wedge-shaped film was grown on a single $SrTiO_3$ substrate. The $LaTiO_3$ layer thickness varied from about 0.1 unit cells on one edge of the substrate to about 2 unit cells on the opposite edge. The $LaTiO_3$ was capped with $SrTiO_3$ and post-annealed. By bonding probe wires to different parts of the sample along the $LaTiO_3$ thickness gradient, it was possible to perform 2-point resistance measurements for different $LaTiO_3$ layer thicknesses. The local thickness could be calculated simply from the bonding wire position, since the $LaTiO_3$ layer thickness gradient was linear.

As can be seen in Fig 5.5, films that were thicker than about 0.5 unit cells of $LaTiO_3$, showed metallic behavior down to about 10 K. Films thinner than one full monolayer started to show a slight upturn of resistance at the lowest temperature. A dramatic upturn and a transition to insulating state was seen for a $LaTiO_3$ thickness of less than 0.4 unit cells of $LaTiO_3$. The upturn occurred at around 50 K for a 0.2 unit cell $LaTiO_3$ layer. It is interesting to note that the high-temperature sheet resistance that separates the metallic $LaTiO_3$ layers from the insulating sample is about 20 kΩ, although it is possible that this is a coincidence, since this is a 2-point measurement at it may involve a significant contribution from contact resistance.

In order to understand better the influence of layer morphology on the conductivity behavior, a separate 0.4 unit cell $LaTiO_3$ film sample was grown on a metallic 0.05 wt% Nb-doped $SrTiO_3$ substrate. The Nb-doped substrates are also chemically etched and annealed. In terms of AFM images, the surface morphology of the Nb-doped substrate is identical to non-doped crystals.

Fig. 5.6 shows an STM surface image of the 0.4 unit cell $LaTiO_3$ layer. The image shows an ideal fractional $LaTiO_3$ layer on $SrTiO_3$, containing homogeneous islands with a typical height of unit cell, although some apparently higher islands can also be seen. This surface is equivalent to the surface shown in Fig. 5.4 and it is clear that AFM images of fractional layers are not reliable for discussing the layer morphology.

Fig. 5.6 **(b)** shows the height profile of the STM image. The image does not contain a convenient height calibration feature, like a step edge, but it is clear that some islands have a larger than unit cell height, as illustrated in Fig. 5.7. The $LaTiO_3$ coverage in the STM image is about 2 times higher than the coverage where a transition to the insulating state was observed in Fig. 5.5.

Careful observation of the STM image shows that the smallest islands on the surface

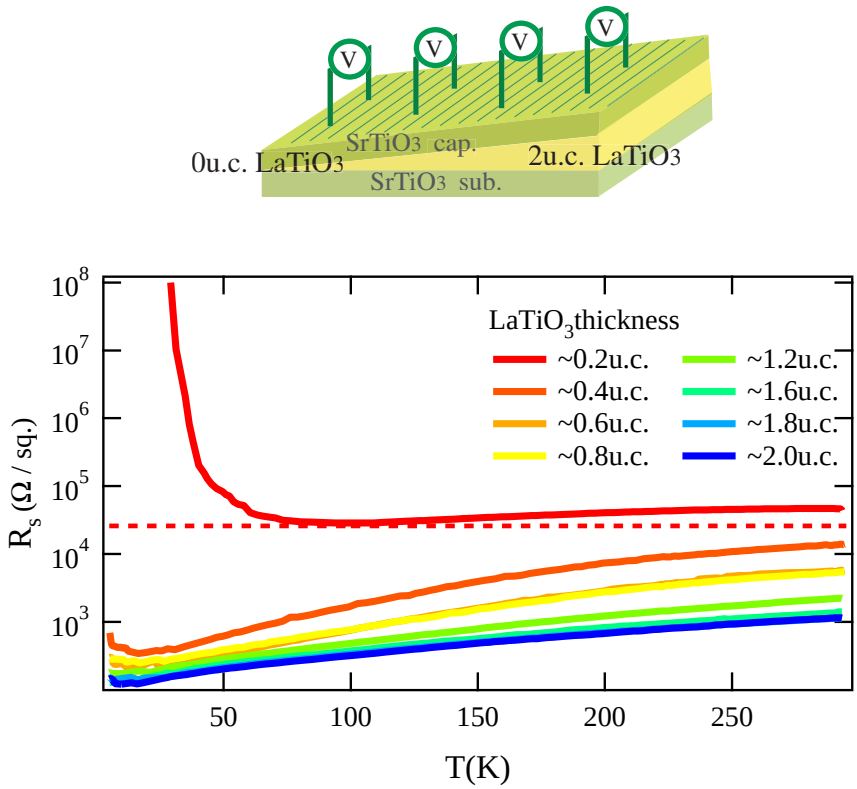

Figure 5.5: Sheet resistance of embedded $LaTiO_3$ layers in $SrTiO_3$ as a function of doping layer thickness. The dotted line corresponds to quantum resistance $h/e^2 \sim 25.8$ kΩ.

have a width of about 1 nm. It thus appears that the smallest stable size of a $LaTiO_3$ island grown at about 500 °C contains 4 to 9 unit cells of $LaTiO_3$.

From the sheet resistance result, it was clear that more than 0.5 unit cell $LaTiO_3$ coverage on $SrTiO_3$ resulted in metallic behavior. In contrast, less than 0.5 unit cell $LaTiO_3$ in $SrTiO_3$ showed a metal-insulator transition at about 50 K. The questions thus arises as to what the conduction mechanism is in the metallic state and what is the mechanism of the metal insulator transition (MIT). As for the metallic conductivity, the resistance ratio between 300 K and the minimum resistance point is at most about 20. This ratio is much lower than that of electron doped $SrTiO_3$, such as the oxygen-deficient samples, where a resistance ratio of R_{300K}/R_{4K} typically exceeds 1000.

Rough estimate of Hall mobility and carrier density for 0.5 unit cell $LaTiO_3$ layer in $SrTiO_3$ at different temperature was shown in Eq. 5.1 and Eq. 5.2. These number were calculated from Hall coefficient from $-1\ T$ to $1\ T$ and sheet resistance at each

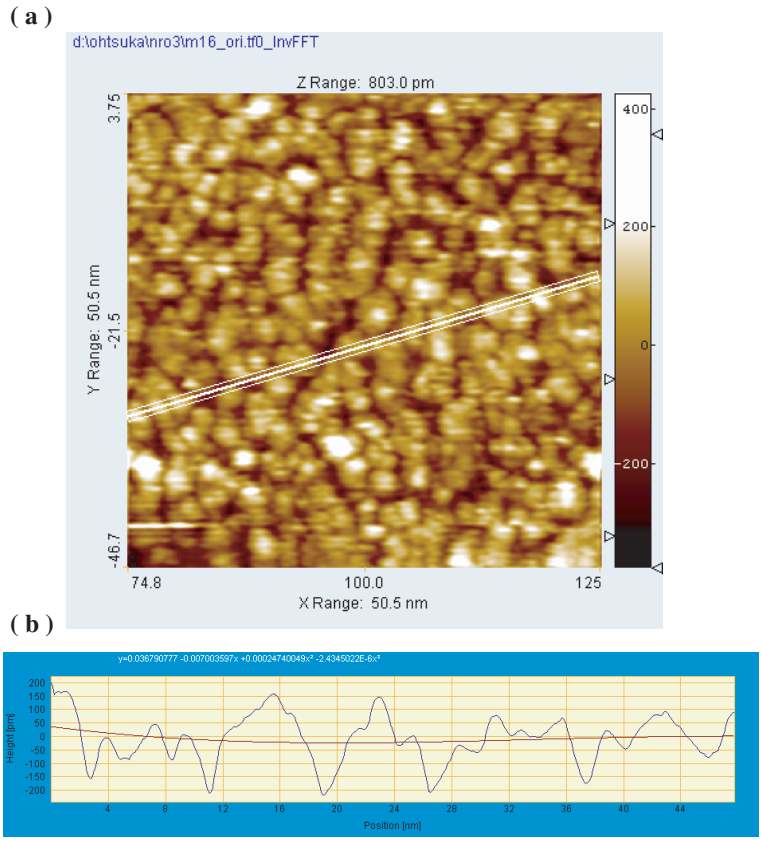

Figure 5.6: **(a)** STM surface morphology and **(b)** height profile of a 0.4 unit cell $LaTiO_3$ layer

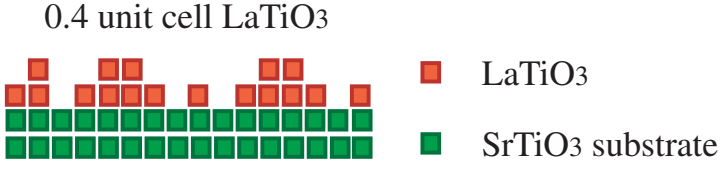

Figure 5.7: Unit cell block image of a 0.4 unit cell film based on the observed STM morphology.

temperature by

$$n = \frac{1}{qR_H} \qquad [cm^{-2}] \tag{5.1}$$

$$\mu_H = \frac{R_H}{R_S} \quad [cm^2/V \cdot s] \tag{5.2}$$

n: carrier density, q: elementary electric charge, R_H: Hall coefficient and R_S: Sheet resistance

these equations. From table 5.1, Hall mobility (μ_H) were increasing as decreasing temperature. Compared with that, carrier density (n) dropped slightly. It means that carrier density dropping might cause of MIT.

Temperature	n (cm^{-2})	μ ($cm^2/V \cdot s$)
50 K	2.9×10^{13}	290
20 K	2.5×10^{13}	920
10 K	2.3×10^{13}	1200
5 K	2.2×10^{13}	1300
2 K	2.2×10^{13}	1400

Table 5.1: Rough estimate of Hall mobility and carrier density for 0.5 unit cell $LaTiO_3$ layer in $SrTiO_3$ at different temperature.

Looking at the 0.4 unit cell resistivity data in Fig. 5.5, the sheet resistance appears to follow an approximate T^2 dependence below about 200 K, which would be expected for (La,Sr)TiO_3 bulk [2] and superlattices [3].

For $LaTiO_3$ layer thickness above 1 unit cell, the resistance dependence was nonlinear on the T^2 scale [Fig. 5.8].

Considering the detached island morphology of the doping layer, the transition to an insulating state could likely be attributed to a percolative transition, although further work would be needed to prove this.

Various mechanisms that can result in a resistivity upturn at low temperatures were considered. One possibility is the Kondo effect, which has been studied metals doped with magnetic impurities and recently also considered in the case of $LaAlO_3$ / $SrTiO_3$ system by Brinkman et al. [4]. The $LaTiO_3$ heterostructures may support a magnetic impurity model if La ions at the interface are responsible for Ti atoms with a single

unpaired electron in a two-dimensional interface layer. In Kondo effect, the crossover temperature scale is given by

$$R_S = a\, ln(\frac{T}{T_{eff}}) + b\, T^2 + c\, T^5, \tag{5.3}$$

where b is related to electron-electron interaction and c to electron-phonon interaction [4, 5].

An attempt to fit the sheet resistance data Fig. 5.5 with this model did not appear to produce satisfactory curve shapes close to the minimum resistance point.

Other possibilities include various localization phenomena, such as Anderson localization due to the loss of carrier mobility at the edge of the conduction band. However, this is an unlikely mechanism due to the high temperature where the conductivity is lost.

Among other predictions, it would be necessary to consider the effect of defects in $SrTiO_3$ and perhaps, charge ordering. Defects such as Sr vacancies can trap carriers in $SrTiO_3$[6]. However, if this were the case, it would not result in a sharp loss of conductivity at an intermediate temperature and would equally affect heterostructures with larger La coverage. Even when the $logR_S$ data in Fig. 5.5 was plotted against $(\frac{1}{T^{\frac{1}{4}}})$, where a linear dependence would suggest three-dimensional variable-range hopping of localized carriers [Fig. 5.9], no linearity was found [7].

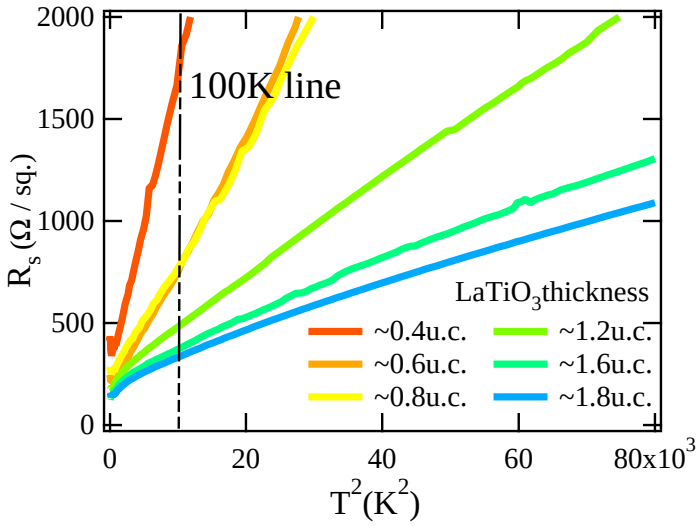

Figure 5.8: Sheet resistance of embedded $LaTiO_3$ layers in $SrTiO_3$ [Fig. 5.5] is replotted vs T^2.

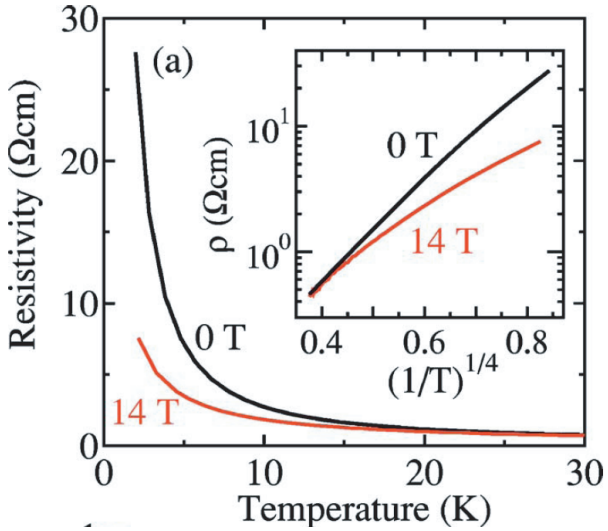

Figure 5.9: Temperature dependence of resistivity at 0 T and 14 T for $Sr_{0.7}La_{0.3}Ti_{0.8}Cr_{0.2}O_3$. The inset shows the plot of ρ vs $(1/T)^{1/4}$ [7].

Charge ordering at $LaTiO_3$ / $SrTiO_3$ interfaces has been predicted.[8] At present, there is no experimental evidence of a charge-ordered state at the interface.

Since many possibilities for the observed behavior have been suggested, it was considered that simple resistivity experiments do not yield sufficient data to draw definite conclusions.

A technically obvious extension of simple transport measurements is to look at the magnetotransport properties of the heterostructures. Magnetotransport can also be used to estimate the dimensionality of conduction at the interface. Magnetotransport results obtained by measuring the low-temperature behavior of metallic samples are discussed in the next Chapter. An attempt was made to test if the apparent localization behavior in the insulating samples can be broken by applying an external magnetic field, similar behavior to Fig. 5.9. However, regardless of the orientation of the applied field, only positive magnetoresistance was seen for a sample where the $LaTiO_3$ coverage was about 0.3 unit cells. The experimental data is shown in Figs. 5.10 and 5.11. The result is certainly different from the proposed magnetic ordering as has been discussed for the $LaAlO_3$ / $SrTiO_3$ interface [4].

One conclusion from the magnetoresistance data is that there appears to be no anisotropy between the magnetoresistance behavior for the magnetic field applied either in the in-plane or the out-of-plane direction. The magnetoresistance also persist

up to 300 K. It is possible that for the nearly insulating sample, conductivity in the capping layer may contribute to the measurement. Forthe case of metallic films at low temperature, it is known that the mobility in the capping layer is very low and conductivity in the cap layer can be safely ignored. For insulating samples, this is not necessarily true.

5.4 Summary

As a summary of this Chapter, a metal-insulator transition was observed when the $LaTiO_3$ layer thickness in a $SrTiO_3$ / $LaTiO_3$ / $SrTiO_3$ heterostructure was reduced to below 0.5 unit cells. The $LaTiO_3$ thickness was estimated by monitoring RHEED oscilations. However, the actual deposited amount appeared to be significantly higher than what was predicted from RHEED measurements when the assumed coverage was compared to STM images. Several mechanisms that might be responsible for the MIT were considered but at least there was no clear signature of magnetic or charge ordering phenomena based on transport measurements.

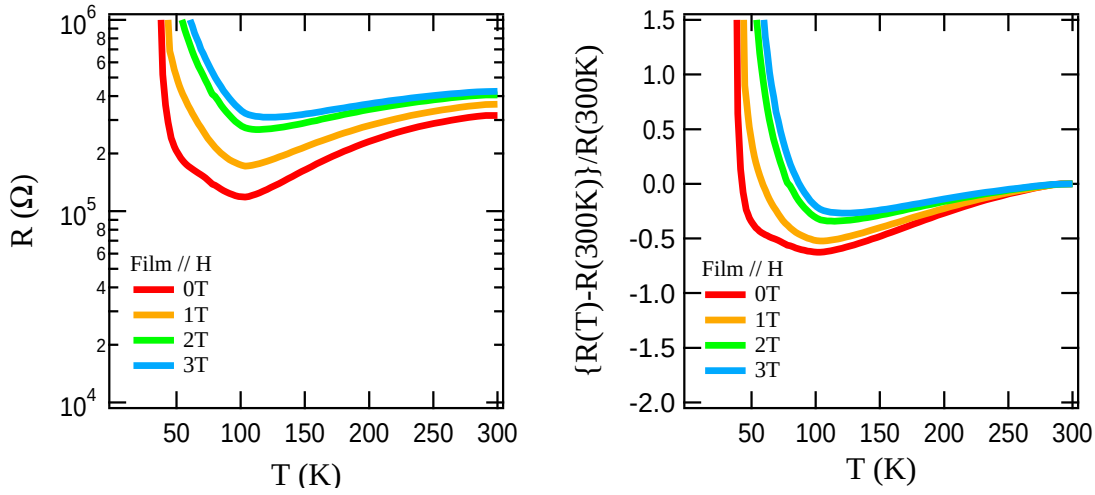

Figure 5.10: Resistance of approximately 0.3 unit cell $LaTiO_3$ layer in $SrTiO_3$ in a magnetic field. The magnetic field was applied parallel to the film.

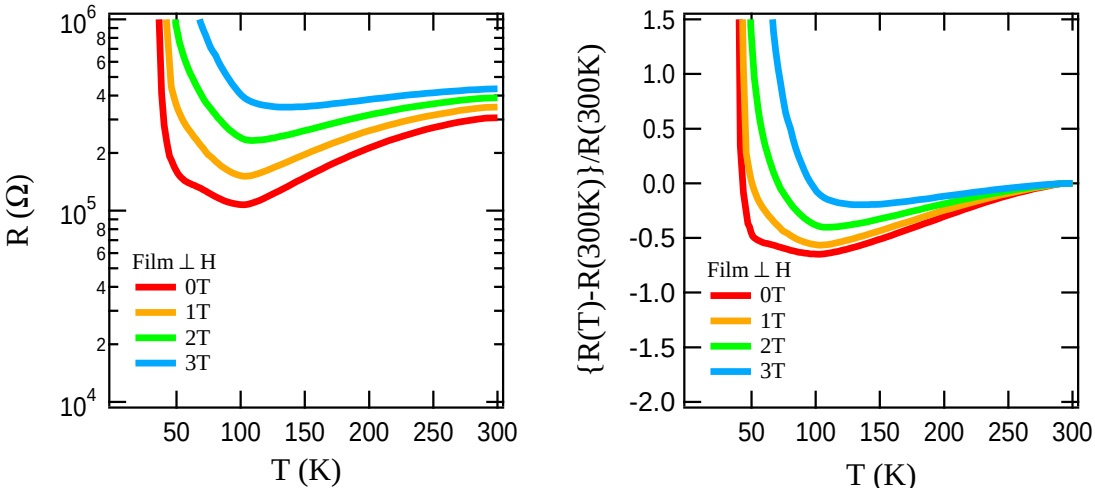

Figure 5.11: Resistance of approximately 0.3 unit cell $LaTiO_3$ in $SrTiO_3$ under a magnetic field. The magnetic field was applied perpendicular to the film.

References

[1] T. Mihara, K. Shibuya, T. Ohnishi, H. Koinuma and M. Lippmaa *Thin Solid Films* **486**, 63 (2005).

[2] Y. Tokura, Y. Taguchi, Y. Okada, Y. Fujimori, T. Arima, K. Kumagai and Y. Iye *Physical Review Letters* **70**, 2126 (1993).

[3] K. Shibuya, T. Ohnishi, M. Kawasaki, H. Koinuma and M. Lippmaa *Japanese Journal of Applied Physics* **43**, L1178 (2004).

[4] A. Brinkman, M. Huijben, M. Van Zalk, J. Huijben, U. Zeitler, J. C. Maan, W. G. Van Der Wiel, G. Rijnders, D. H. A. Blank and H. Hilgenkamp *Nature* **6**, 493 (2007).

[5] C. Kittel *INTRODUCTION TO SOLID STATE PHYSICS 8th ed*.

[6] T. Ohnishi, K. Shibuya, T. Yamamoto and M. Lippmaa *Journal of Applied Physics* **103**, 103703 (2008).

[7] J. Inaba and T. Katsufuji *Physical Review B* **72**, 052408 (2005).

[8] R. Pentcheva and W. E. Pickett *Physical Review Letters* **99**, 016802 (2007).

Chapter 6

Transport properties of $LaTiO_3$ / $SrTiO_3$ in magnetic field

In the previous Chapter, the possibility of localization at $LaTiO_3$ interfaces was discussed. This Chapter is devoted to the discussion of transport properties, magnetoresistance and Hall resistance of embedded $LaTiO_3$ layers in $SrTiO_3$ for $LaTiO_3$ thicknesses above 0.5 unit cells. All of these samples are metallic.

6.1 Introduction

Metallic conductors in an external magnetic field show ceratin characteristic features, such as magnetoresistance. For ferromagnetic materials, a magnetic field dependent hysteresis may also be seen. If conductivity is limited to a thin two-dimensional layer or the measurement temperature is sufficiently low, other phenomena may become observable, such as various quantum effects, Shubnikov-de Haas oscillations, etc.

Magnetotransport properties of four different metallic $LaTiO_3$ heterostructures were studied. The samples differed by the thickness of the $LaTiO_3$ layer. Although the original aim was to ascertain the origin of the metal insulator transition that was described in Chapter 5, it became apparent that aspects other than possible interface ordering need to be understood first. Among these, the thickness of the conducting layer and the mobility behavior of carriers was of primary interest.

One advantage of measuring magnetotransport in thin heterostructures is the possibility of measuring the thickness and dimensionality of the conducting layer. Current-carrying electrons moving through a heterostructure in a magnetic field are forced by the Lorentz force to follow a cycloid path, which increases the chance of scattering and

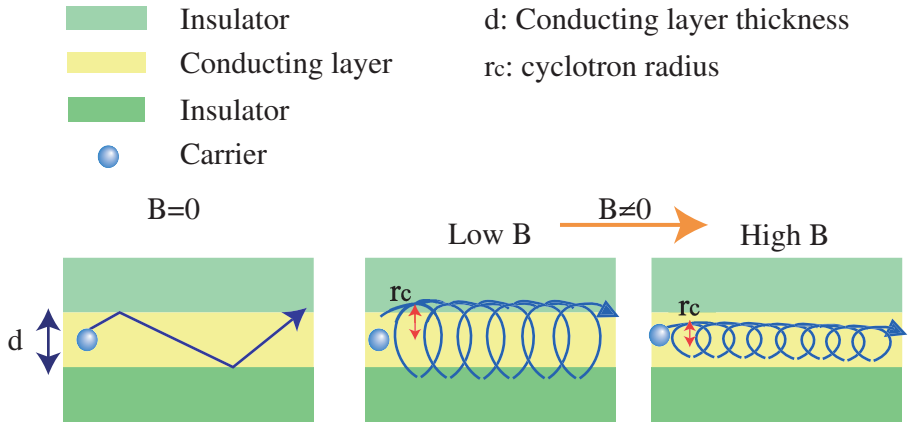

Figure 6.1: Illustration of carrier behavior in a magnetic field.

thus the apparent resistance of a sample. For a magnetic field applied perpendicuar to a heterostructure, the resistance increase would be proportional to the magnetic field and thus a positive magentoresistance response would be expected. When the magnetic field is applied in the plane of the heterostructure, a similar behavior would occur if the conducting layer is thick enough for the electrons to follow a similar circular path. If, however, the heterostructure is considerably thinner than the cyclotron motion radius, this mechanism would not contribute, and the positive magnetoresistance behavior would vanish or at least be diminished. Since the cyclotron radius is given by

$$r_c = \frac{mv}{qB} = \frac{hk}{2\pi qB}, \tag{6.1}$$

where m is the effective mass of an electron and v is the velocity of the electron, it is possible to estimate the cyclotron radius for a given field strength B [Fig. 6.1]. By comparing the positive magnetoresistance component in the resistance behavior of a sample, it would thus be possible to say if the effective thickness of a metallic layer is larger or smaller than the cyclotron radius. By changing the magnetic field, and thus reducing the cyclotron radius at high fields, it may be possible to measure the conducting layer thickness if the appearance of positive magnetoresistance is observed only above a certain critical field strength.

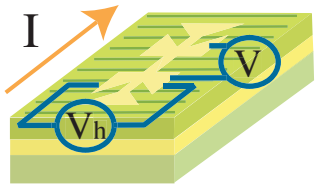

Figure 6.2: Illustration of a Hall bar sample, showing the electrical connections and the orientation relative to the surface steps.

6.2 Experiment

The heterostructures were grown under the conditions described in Chapter 4. For magnetoresistance measurement, four samples with different $LaTiO_3$ layer thicknesses embedded in $SrTiO_3$ were prepared. Since only metallic samples could be measured, the minimum $LaTiO_3$ layer thickness was 0.5 unit cells. Other samples had $LaTiO_3$ thicknesses of 1, 4, and 10 unit cells. The thickness was estimated by RHEED oscillations and calibrated agains thick layer deposition rate. The samples were post-annealed in air after $LaTiO_3$ and $SrTiO_3$ capping layer deposition to eliminate the effect of oxygen vacancies in $SrTiO_3$. For all samples, the surface of the $SrTiO_3$ capping layer showed straight steps sand flat terraces, at least when measured by AFM. Hall bars were cut in the sample surface by mechanical milling as shown in Fig. 6.2. Details of the process are presented in Chapter 2. Contacts to the Hall bars were made by Al wire bonding through the $SrTiO_3$ capping layer to the embedded $LaTiO_3$ layer. In order to check the effect of surface steps on the transport properties, three Hall bar were milled into each sample crystal. The step direction on each sample was checked by AFM and the Hall bars were oriented so that the current flow was either parallel to steps, perpendicular to steps or at an intermediate 45° angle. The terrace width was approximately 120 nm for all samples.

The four samples were measured by PPMS, as outlined in Chapter 2. The temperature dependence of sheet resistance is shown in Fig. 6.3. All samples showed metallic behavior. This result is qualitatively similar to earlier results obtained by Mihara et al. [1]. For most samples, magnetoresistance and Hall resistance were measured at 300 K ~ 5 K and in the magnetic field range from -5 T to 5 T. In the following discussion, magnetoresistance is defined as $\Delta R\ (H)\ /\ R\ (0)$, where $\Delta R\ (H) = R\ (H) - R\ (0)$ for all samples. Angle dependence of magnetoresistance was measured below 2 K while applying a magnetic field of 0 ~ 3 T.

In order to study the effect of carrier density on transport properties independently of the $LaTiO_3$ layer thickness, magnetoresistance and Hall resistance were also measured for a 10 unit cell sample while applying a back-gate bias. Contact between the $SrTiO_3$ substrate and a copper metal plate was made by silver paste. Leakage current was less than 1 nA in this system. The source and drain contacts were also made by Al wire bonding. The current path in the Hall bars was chosen to be parallel to the step edges, i.e. the current could flow along the terraces without being affected by scattering at the step edges.

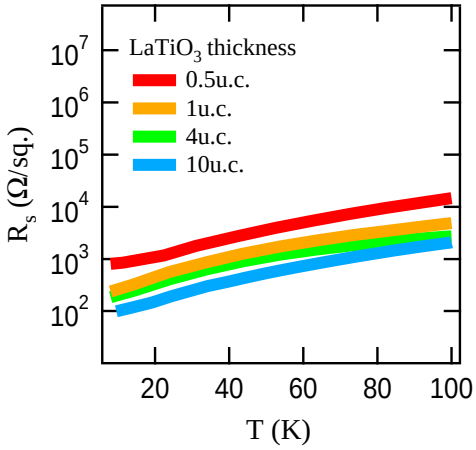

Figure 6.3: Sheet resistance temperature dependence for different $LaTiO_3$ layer thicknesses embedded in $SrTiO_3$.

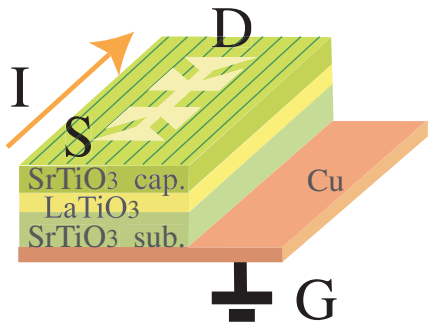

Figure 6.4: Measurement geometry used in the back-gated field-effect magnetoresistance measurements.

6.3 Results and discussion

6.3.1 Out-of-plane magnetoresistance

Magnetoresistance (MR) was measured for different $LaTiO_3$ thickness samples while applying a magnetic field in the out-of-plane direction, perpendicular to the surface [Fig. 6.5]. As expected, a strong positive MR was seen in all four samples. It is clear that the slope of the MR curves, which scales with carrier mobility, increased in samples with a thicker $LaTiO_3$ layer. As will be discussed later in this Chapter, all of these samples show multiple conducting layers, with very high mobility carriers being present in the $SrTiO_3$ substrate. The MR slope dependence can thus be understood as reflecting the increase of the density of deep high-mobility carriers in the substrate part of the heterostructure.

From the point of view of observing the presence of a magnetically ordered phase, as has been suggested for the $LaAlO_3$ / $SrTiO_3$ heterostructure [Fig. 6.6] [2], it would be important to look for hysteretic field-dependent resistance curves. In terms of zero-field resistance, there is at least a superficial resemblance between the lowest carrier density $LaAlO_3$ / $SrTiO_3$ interfaces and the $LaAlO_3$ / $SrTiO_3$ heterostructures in that both show an upturn of resistance below about 100 K. However, the functional shape of the resistance is quite different, i.e. the $LaTiO_3$ heterostructure do not show a linear resistance region in a log(T) plot. None of the $LaTiO_3$ samples showed any hysteretic behavior, either in magnetoresistance or Hall resistance data. Although $LaTiO_3$ / $SrTiO_3$ superlattices have been considered to possibly show magnetic order [3, 4], the current data does not appear to support the presence of ferromagnetic order.

It should also be noted that at least for the thinnest $LaTiO_3$ / $SrTiO_3$ heterostructures, the doping layer would presumably contain a sizeable fraction of Sr cations at the A-site. For thicker heterostructures, where the $LaTiO_3$ layer thickness is 10 unit cells, the doping layer would consist of nearly pure $LaTiO_3$. Magnetic effects due to carrier doping or the presence of oxygen vacancies in $Sr_xLa_{1-x}TiO_3$ have been studied. It was reported by Tokura et al. that when almost all Sr is replaced by La, the Ti ions obtain a formal valence of 3+ with a spin -1/2 local moment [3]. It is not clear, though, how the bulk results translate to very thin films. The presence of negative magnetoresistance in $Sr_xLa_{1-x}TiO_3$ has been reported, but only when nearly 20% of the Ti atoms have been replaced by Cr. For the Cr-doped system, the negative MR behavior was attributed to a magnetic coupling between the Cr imputity ions, mediated by conduction electrons [5].

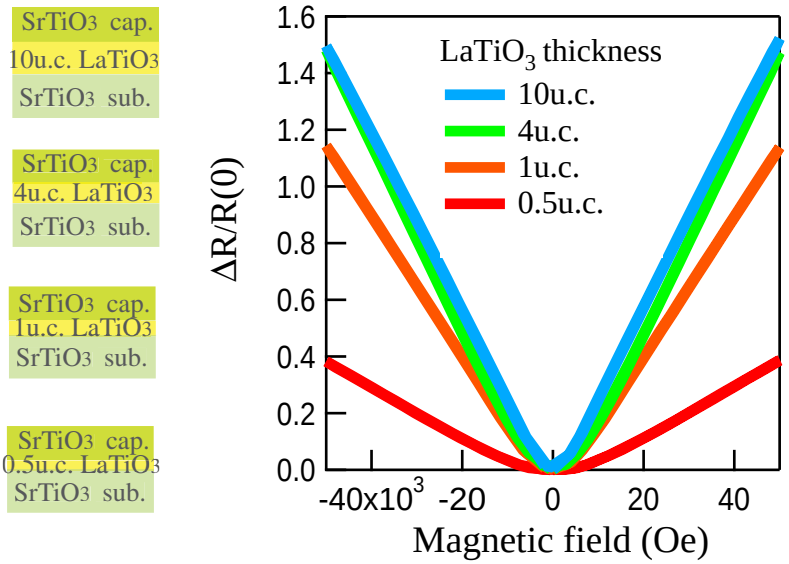

Figure 6.5: Magnetoresitance for a magnetic field applied in the out of plane direction for 0.5, 1, 4, and 10 u.c. $LaTiO_3$ layers embedded in $SrTiO_3$.

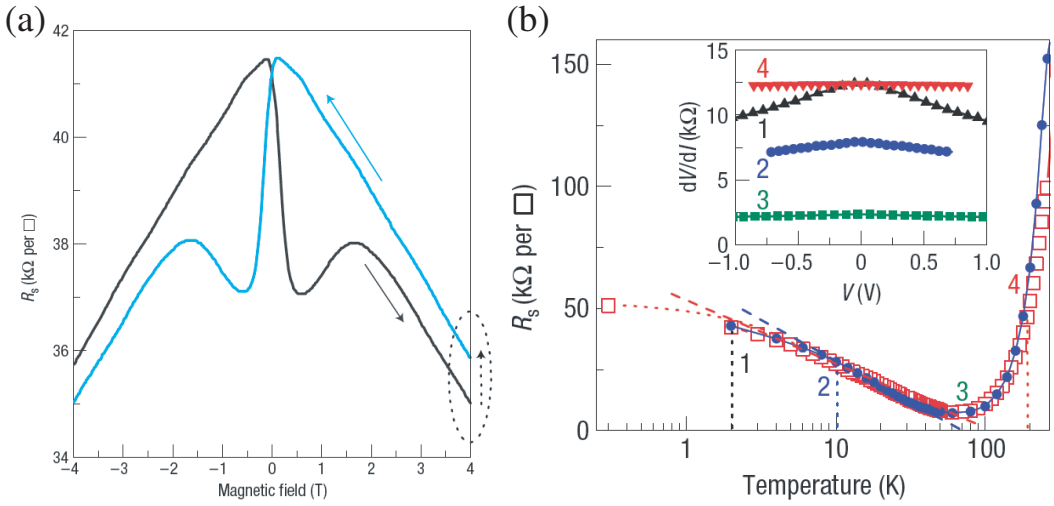

Figure 6.6: **(a)** Magnetic hysteresis of $LaAlO_3$ / $SrTiO_3$ conducting layer. The magnetoresistance is independent of field orientation. And **(b)** temperature dependence of sheet resistance, R_S, for two conducting interfaces, grown in different oxygen pressure. Th low temperature logarithmic dependences are indicated by dashed lines. Inset: Four-point differential resistance dV/dl as function of applied voltage, at a constant temperature of 2.0 K (1), 10.0 K (2), 50.0 K (3) and 180.0 K (4) [2].

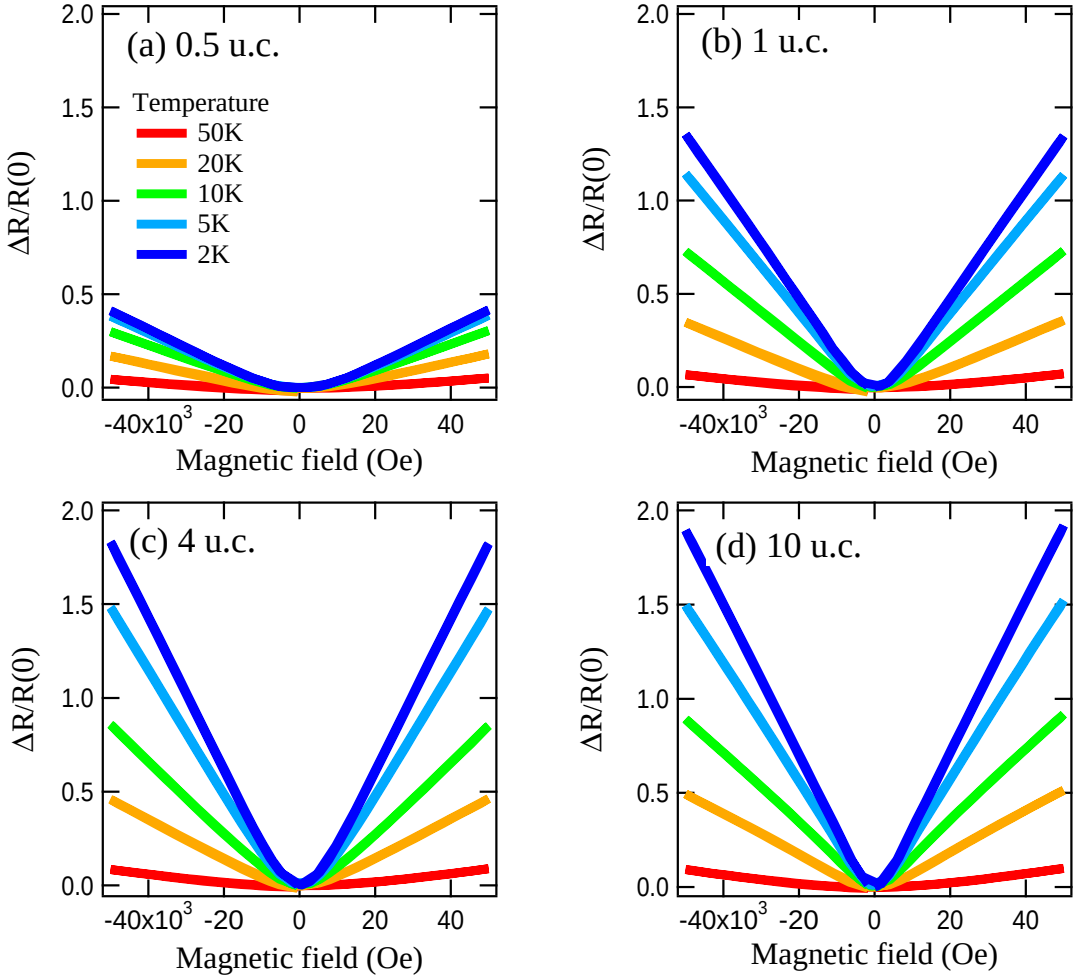

Figure 6.7: Temperature dependence of magnetoresistance for an out of plane magnetic field for different $LaTiO_3$ layer thicknesses in $SrTiO_3$.

Fig. 6.7 shows the temperature dependence of MR for the four samples. With decreasing temperature, the MR response increased in all samples. The temperature effect was larger in thicker $LaTiO_3$ samples. The cause for this appears to be the larger number of carriers that were injected into the $SrTiO_3$ substrate from the $LaTiO_3$ doping layers in those samples. High-mobility carriers in the clean $SrTiO_3$ crystals would be expected to show a stronger temperature dependence due to the strongly temperature-dependent mobility in bulk $SrTiO_3$ [6]. The bulk mobility is known to saturate below about 5 K [Fig. 6.8 **(a)**]. This effect is also evident in the MR data, with the difference in the slope of the MR curves becoming smaller between the curves measured at 2 K

and 5 K than, for example, the 20 K and 50 K curves, although the relative temperature change is the same. There is also a large drop in the MR amplitude in the 0.5 unit cell sample. These results show that thinner $LaTiO_3$ layers in $SrTiO_3$ do not contain high-mobility carriers but thicker $LaTiO_3$ layer do have high-mobility carrier that are associated with the $SrTiO_3$ substrate, rather than the $LaTiO_3$ layer itself [Fig. 6.8 **(b)**]. This feature will be discussed further in relation to the non-linear Hall resistance.

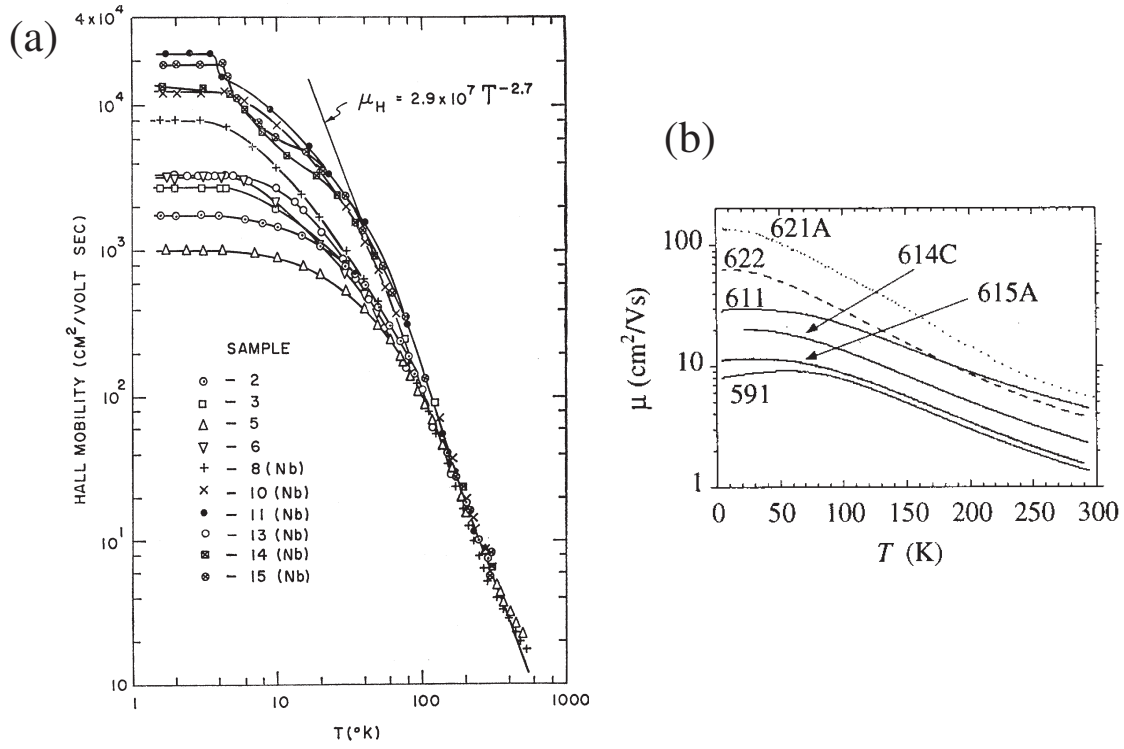

Figure 6.8: Temperature dependence of Hall mobility **(a)** in semiconducting $SrTiO_3$ [6] and **(b)** La-doped $SrTiO_3$ films on $SrTiO_3$ (dashed line) and on $LaAlO_3$ (solid line) substrate [7]

6.3.2 In-plane magnetoresistance

When the magnetic field was applied parallel to the film, a large negative MR was observed in thinner $LaTiO_3$ samples. The original assumption, that it would be possible to determine the effective conducting layer thickness by measuring the magnetoresistance response in a parallel magnetic field geometry, proved to be incorrect. Instead of observing a flat MR curve for low fields, a strong negative response was

seen, as shown in Fig. 6.9. It was therefore impossible to determine the conducting layer thickness. This result was already prompted by the measurements done in the out-of-plane field geometry, since it showed that carriers are distributed deep in the substrate. It is therefore reasonable to assume that the thickness of the conduction layer is not a well defined quantity.

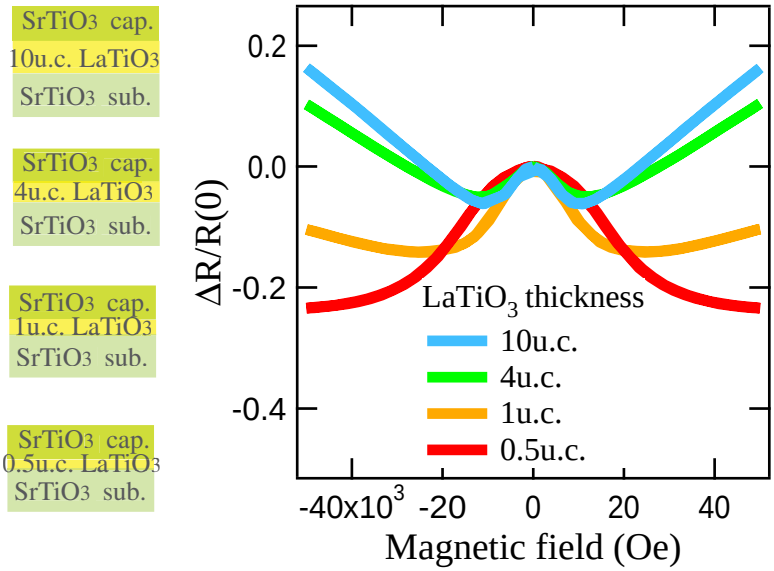

Figure 6.9: Magnetoresitance for an in-plane magnetic field in $LaTiO_3$ heterostructures with different doping layer thicknesses.

In order to evaluate possible mechanisms that could explain the negative magnetoresistance, temperature dependence was also measured for the in-plane MR behavior. The results are summarized in Fig. 6.10. What is obvious from the data, is the different temperature scale for the negative and positive MR components. The positive MR survives up to room temperature, although the resistance change becomes smaller at higher temperatures. The negative component, however, could only be observed at temperatures below 15 K. It appears from the data that positive MR dominates the thicker samples, whereas negative MR dominates the behavior in thinner $LaTiO_3$ layers. It may thus be possible to associate this behavior with the type of charge ordering that has been predicted by Pentcheva *et al.* [4].

It is obvious that the oxide heterostructures studied here can not be considered particularly clean systems. Among various impurity scattering studies, a somewhat similar impurity-related negative magnetoresistance response has been observed by

Kawaguchi *et al.* The MR behavior was attributed to conduction electron scattering from magnetic impurities in a quasi two-dimensional semiconductor [8]. However, the MR behavior vanished for a magnetic field applied in the plane of the sample and thus can not be directly applied to the case of $LaTiO_3$ heterostructures.

Regardless of the scattering mechanism that is responsible for the low-temperature negative magnetoresistance, it is clear that these films were 2 dimensional systems and definitely not 3 dimensional because of the large difference in the observed transport properties when the applied magnetic field was either normal or parallel to the heterostructure.

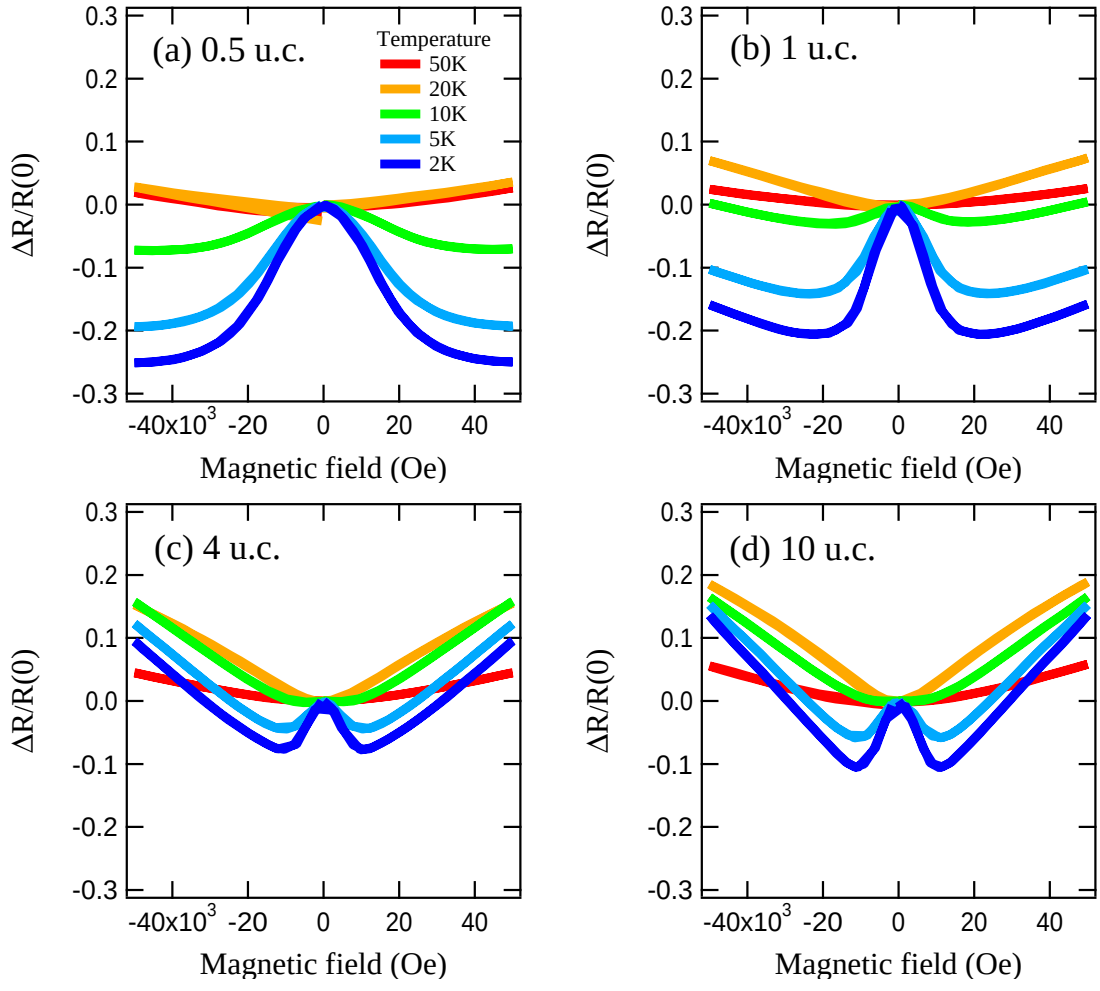

Figure 6.10: Temperature dependence of in-plane magnetoresitance for different $LaTiO_3$ layer thicknesses in $SrTiO_3$.

The thickness and temperature dependence data for the negative magnetoresistance in the $LaTiO_3$ / $SrTiO_3$ heterostructures appeared to show that the negative MR component is related to the $LaTiO_3$ doping layer, whereas the positive component is related to high-mobility carriers in the $SrTiO_3$ substrate. Generally, negative MR behavior in various impurity-related mechanisms is explained by scattering. Weak localization is one such mechanism, although it would apply for a measurement geometry where the magnetic field is applied perpendicular to the surface.

If the assumption that the different MR components originate in different parts of the heterostructure is true, it should be possible to prove this by artificially increasing on decreasing the density of scatterers in the interface layer. Since adding impurities to the system may have other unforeseen consequences, an attempt was made to use the surface steps of the substrate as additional scatterers in the $LaTiO_3$ layer.

For each sample, therefore, Hall bars were cut in three different orientations, perpendicular to the steps, at 45° to steps, and parallel to steps, as shown in Fig. 6.11 and Fig. 6.12. Negative MR was only observed when the current was directed along the terraces, where the additional scattering influence of the steps would be minimal. In other orientations, the positive MR associated with deep carriers in the substrate, appeared to dominate.

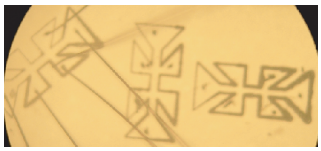

Figure 6.11: Hall bar on sample surface

A model that might explain the contributions of the different conducting layers in the system is shown in Fig. 6.13. Since the negative MR is strongly dependent on the direction of current flow relative to surface steps, it appears reasonable to expect that this component originates at the $LaTiO_3$ / $SrTiO_3$ substrate interface. Since the strong positive MR requires relatively high mobility to be visible, it can be assigned to current in the substrate crystal. The contribution of the capping layer should be quite small.

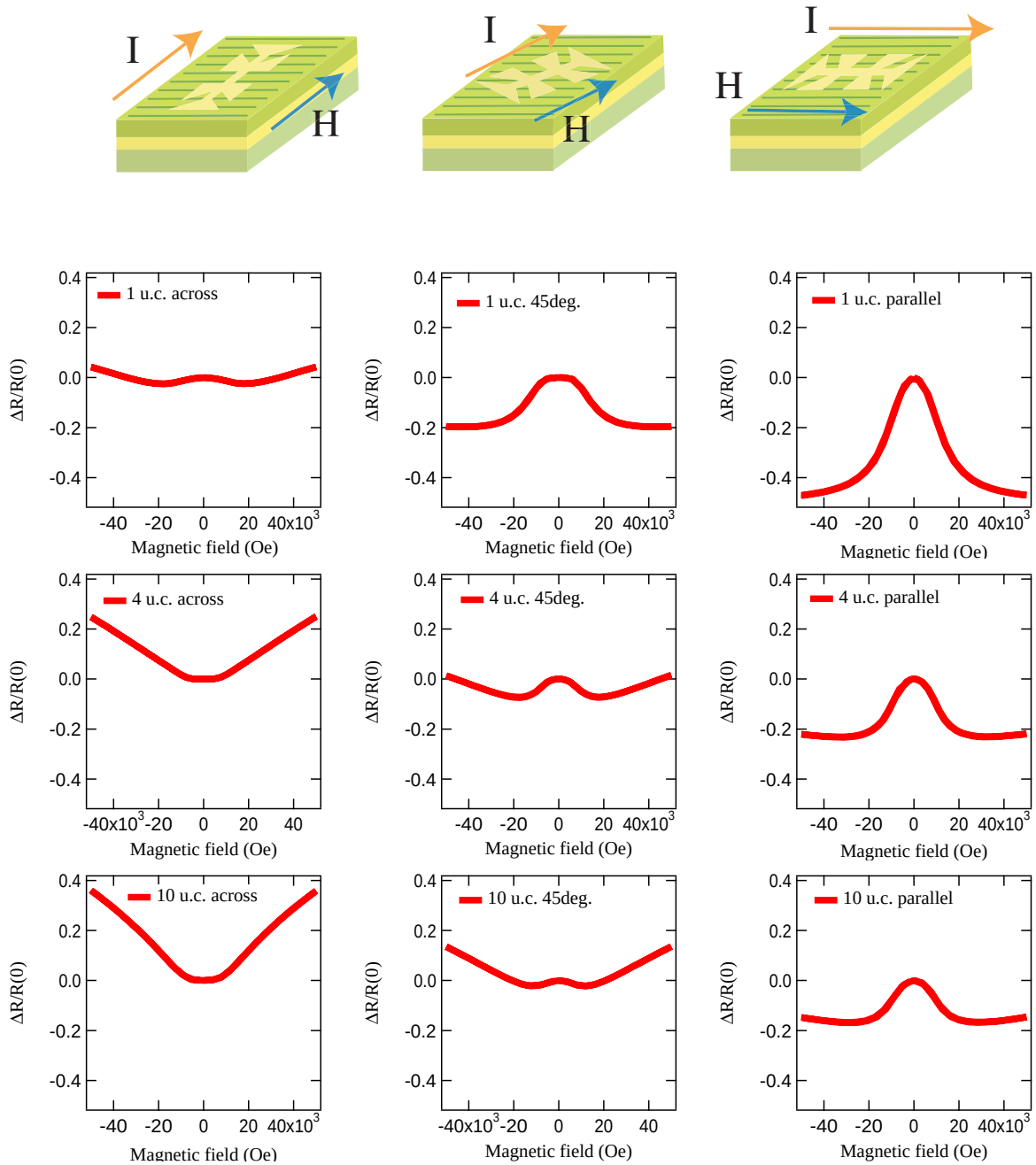

Figure 6.12: In plane magnetoresistance of 1, 4, and 10 unit cell $LaTiO_3$ layers in $SrTiO_3$ for three different angles between the current flow direction and the substrate surface steps. All measurements were done at 5 K.

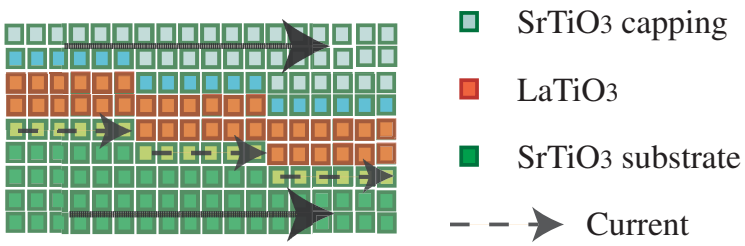

Figure 6.13: Illustration of different possible current paths close to the $LaTiO_3$ doping layer.

6.3.3 Angle dependence

Angle dependence of MR behavior was measured for a geometry where the current flow was perpendicular to the surface steps and the magnetic field was rotated in a plane perpendicular to the current flow, as shown in Fig. 6.14. Two heterostructures, with $LaTiO_3$ layer thicknesses of 1 and 4 unit cells were used in these measurements. The measurement was done in a pumped liquid helium cryostat, giving a temperature of slightly below 2 K, although due to technical problems, the actual sample temperature could not be measured. The maximum magnetic field strength was 3 T. The data in Fig. 6.14 clearly shows that transport in the heterostructures was two-dimensional. A strong angle-dependent MR change was seen, with a crossover from positive to negative MR as the magnetic field was rotated from the out-of-plane orientation to the in-plane orientation, perpendicular to current flow.

The angle dependence was measured by rotating the sample in a constant magnetic field of $B = 0.6$ T [Fig. 6.15]. For both samples, the angle dependence appeared to follow a simple cosine shape.

$$R \propto \cos \beta. \tag{6.2}$$

The angle scans were measured at a low field, where the positive MR component dominates. The angle-dependent resistance change thus mostly reflects the disappearance of the positive MR component. Since the resistance change follows a simple cosine law, it can be concluded that the positive MR part is simply proportional to the out-of-plane magnetic field component.

In thinner samples, where the $LaTiO_3$ layer thickness was either 1 or 4 unit cells, the negative MR behavior dominates and it is thus easier to use these heterostructures to probe the angle dependence of the negative MR component. The results are shown

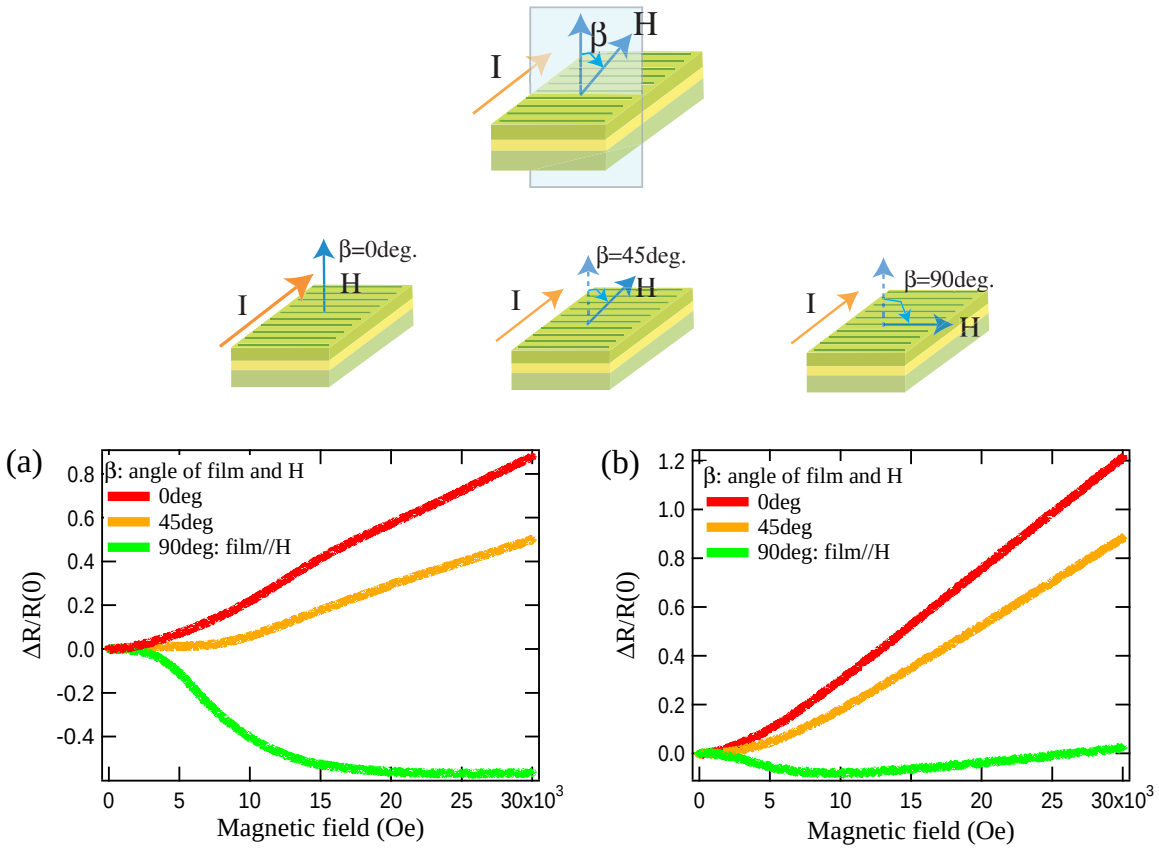

Figure 6.14: In-plane angle-dependent magnetoresistance for (a) 1 unit cell and (b) 4 unit cell $LaTiO_3$ layers embedded in $SrTiO_3$, measured at slightly below 2 K.

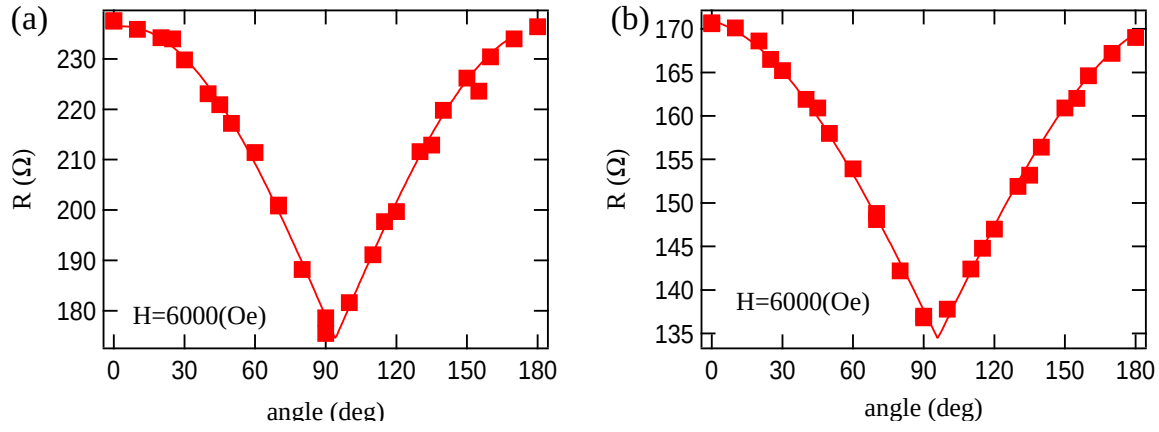

Figure 6.15: Angle dependence of 1 (a) and 4(b) unit cell $LaTiO_3$ layer resistances measured at 2 K and a fixed field of H = 6000 Oe.

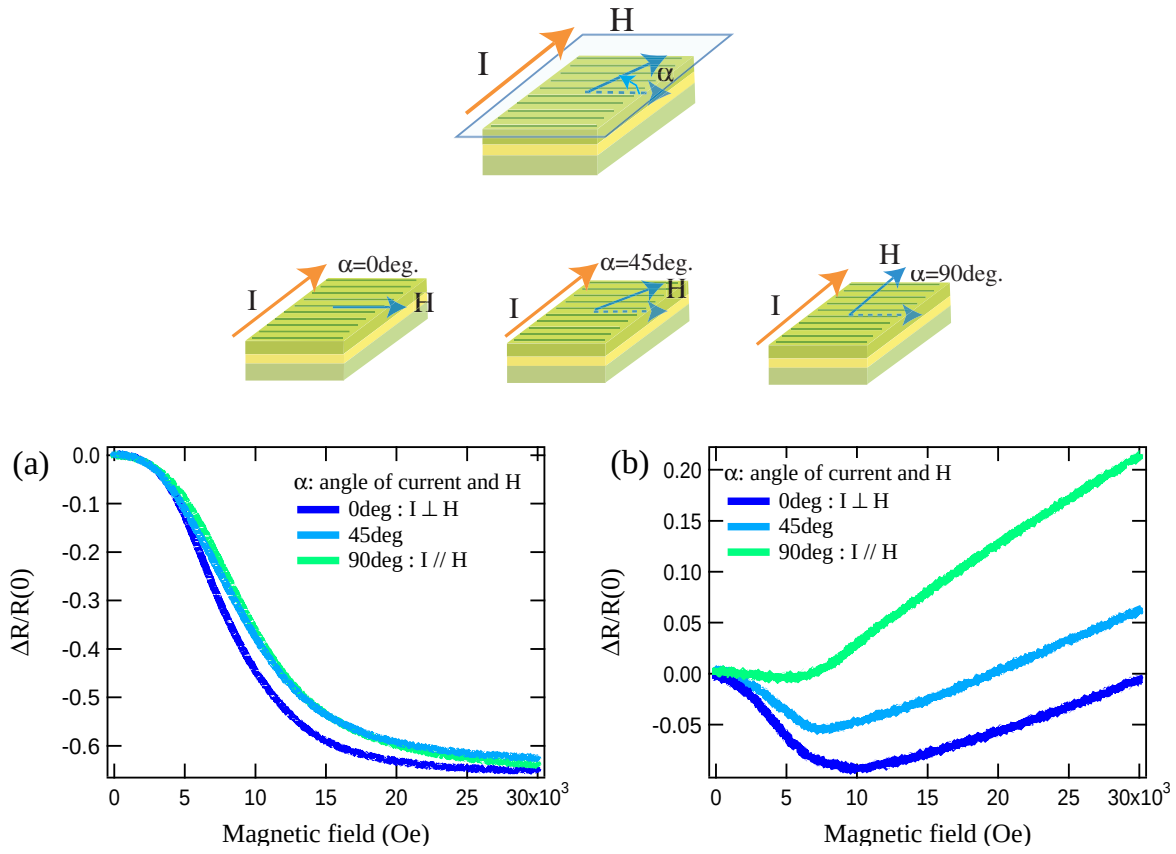

Figure 6.16: In plane angle dependence of in plane magnetoresitance for embedded $LaTiO_3$ layer in $SrTiO_3$ below 2 K, **(a)** 1 unit cell $LaTiO_3$ and **(b)** 4 unit cell $LaTiO_3$

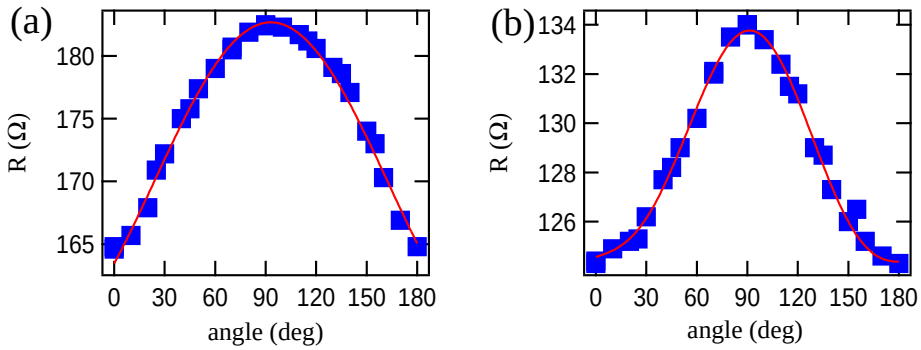

Figure 6.17: In plane angle dependence of magnetoresitance for embedded $LaTiO_3$ layers below 2 K, **(a)** 1 unit cell $LaTiO_3$ and **(b)** 4 unit cell $LaTiO_3$, H=6000Oe.

in Fig. 6.16. The measurements were done at fields of up to 3 T. For angle dependence measurement, the field was fixed at $B = 0.6$ T and rotated from being perpendicular to current flow ($\alpha = 0$ degrees) to parallel to current ($\alpha = 90$ degrees).

The thinnest sample, where the $LaTiO_3$ layer thickness was 1 unit cell, did not show a large difference in MR behavior as the field was rotated. The angle dependence of resistance, plotted in Fig. 6.17 **(a)** showed a cosine law dependence. However, the 4 unit cell $LaTiO_3$ sample had a larger angle dependence. The angular dependence of resistance $B = 0.6$ T could not be fitted by a simple cosine function. The functional shape is not particularly distinct, but fitting is possible with a cosine square function. The line in Fig. 6.17 **(b)** shows a fit by

$$R \propto \cos^2(\alpha) + \cos(\alpha) \tag{6.3}$$

These measurements appear to show that the magnetoresistance behavior is not related to a simple Lorentz force mechanisms but that more elaborate scattering mechanisms are involved.

Some research groups have reported negative MR, e.g. Herranz *et al.* showed it with Shubnikov-de Haas oscillations in $LaAlO_3$ / $SrTiO_3$ system [9] and Kozuka *et al.* observed negative MR in photocarrier-doped $SrTiO_3$, but that behavior was assigned to weak localization [10].

Among published data, the most similar experimental result has been recently reported by Shalom *et al.* for $LaAlO_3$ / $SrTiO_3$ interfaces [Fig. 6.18] [11]. In that case, positive MR was observed when the magnetic field was applied perpendicular to the film with no hysteresis down to hundreds *mK* order. Also, large negative MR was seen for fields applied parallel to the film and current flow. Shalom *et al.* suggested that the large negative MR and its strong anisotropy was caused by a magnetically ordered phase forming at the interface.

The magnetoresistance measurements were shown here leave open the possibility of a magnetically ordered phase appearing in the heterostructures. A negative response is seen in parallel field geometry, which appears to rule out weak localization mechanisms. Magnetic impurity scattering does not seem to offer a mechanism that would explain strong anisotropy. However, magnetoresistance itself cannot provide information on the type of magnetic order that would appear. The present experiments thus leave this problem open. A significant difference between the $LaTiO_3$ heterostructures and $LaAlO_3$ interfaces is that the $LaTiO_3$ system appears to have multiple parallel conduction layers. This aspect is explained in the next Section.

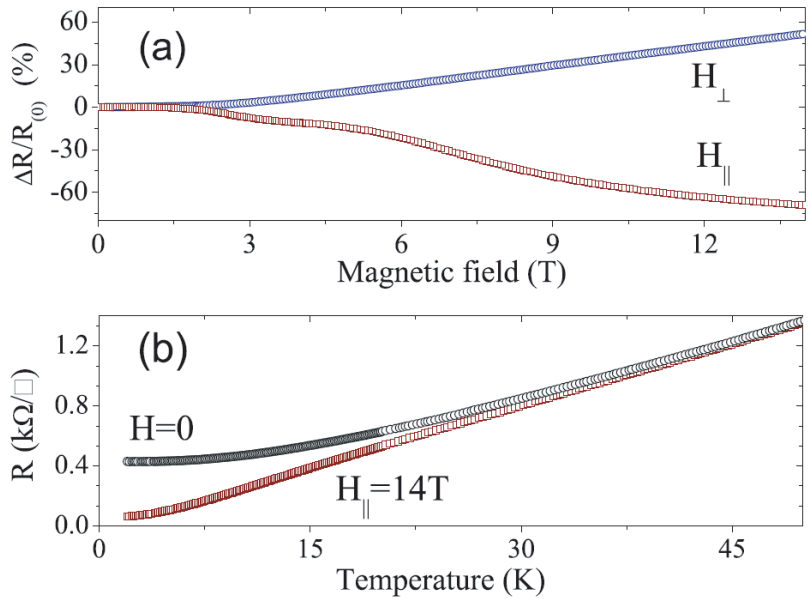

Figure 6.18: 8 u.c. $LaAlO_3$ film on $SrTiO_3$ grown at oxygen pressure of 5×10^{-5} Torr. **(a)** blue circles: the MR as a function of magnetic field applied perpendicular to the interface. Red squares are the MR data for field applied along the interface parallel to the current. **(b)** The sheet resistance as a function of temperature at zero field (black circles) and at 14 T applied parallel to the current (red squares) [11].

6.3.4 Hall resistance

Hall resistance measurements were done with the same four samples as the magnetoresistance work. The $LaTiO_3$ layer thickness was either 0.5, 1, 4 or 10 unit cells. The Hall measurements were done in a PPMS in a usual 4 point measurement geometry using Hall bars cut into the heterostructures by mechanical milling. The process was described in Chapter 3. The current direction was perpendicular to the step edge. In addition to measuring carrier densities and mobilities, the purpose was to look for nonlinearity in Hall resistance, as this had been seen before in $SrTiO_3$-based heterostructures and has been shown to be caused by the presence multiple parallel conducting layers with different mobilities.

All $LaTiO_3$ heterostructures showed nonlinearity in Hall resistance measurements. Some representative examples are shown in Fig. 6.19. Similar nonlineraity in Hall resistance has been reported by other research groups, for example for the $LaAlO_3$ / $SrTiO_3$ system by Bell *et al.* [12]. It is also well known for semiconductor systems like

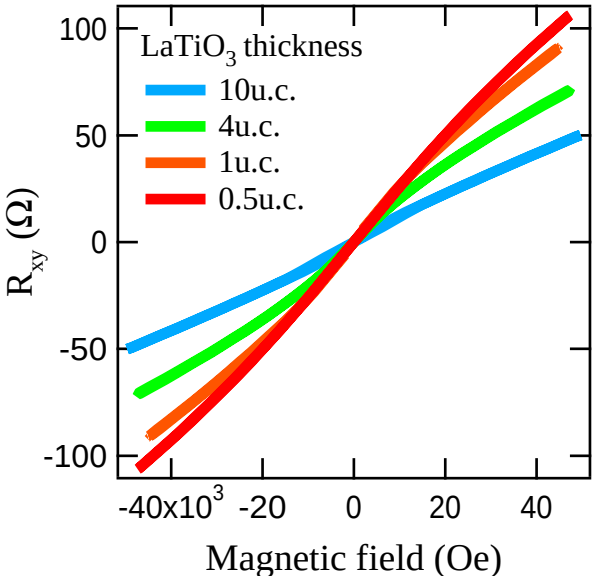

Figure 6.19: Hall resistance of 0.5, 1, 4, and 10 unit cell $LaTiO_3$ layers embedded in $SrTiO_3$, measured at 5 K.

AlInSb / InAsSb quantum wells [13], etc. It is generally interpreted as being a sign of the presence of multiple conducting layers that carry current in parallel and have comparable resistances but very different mobilities. The nonlinear behavior was generally seen at temperatures below 50 K, as shown in Fig. 6.20. It is known that the mobility of carriers in lightly-doped $SrTiO_3$ increases by more than an order of magnitude below 50 K and thus carriers transferred into the $SrTiO_3$ substrate from the $LaTiO_3$ layers could be responsible for a second, high-moblity conduction path in the otherwise nondoped and insulating substrate material. For further analysis, multiple conducting layers were approximated by a two-layer model that includes a high-carrier-density, low-mobility layer and a low-carrier-density high-mobility layer. These two layers could, for example, correspond to the $LaTiO_3$ layer and perhaps the first monolayer of $SrTiO_3$, which would have a high carrier density but likely a rather low mobility due to the large carrier density. Deeper carriers in the $SrTiO_3$ would correspond to the high-mobility layer in the two-layer model.

Two carrier model

When two types of carriers play comparable roles in conduction, it is possible to observe nonlinear Hall resistance in some semiconductors, such as GaAs and InAs. The

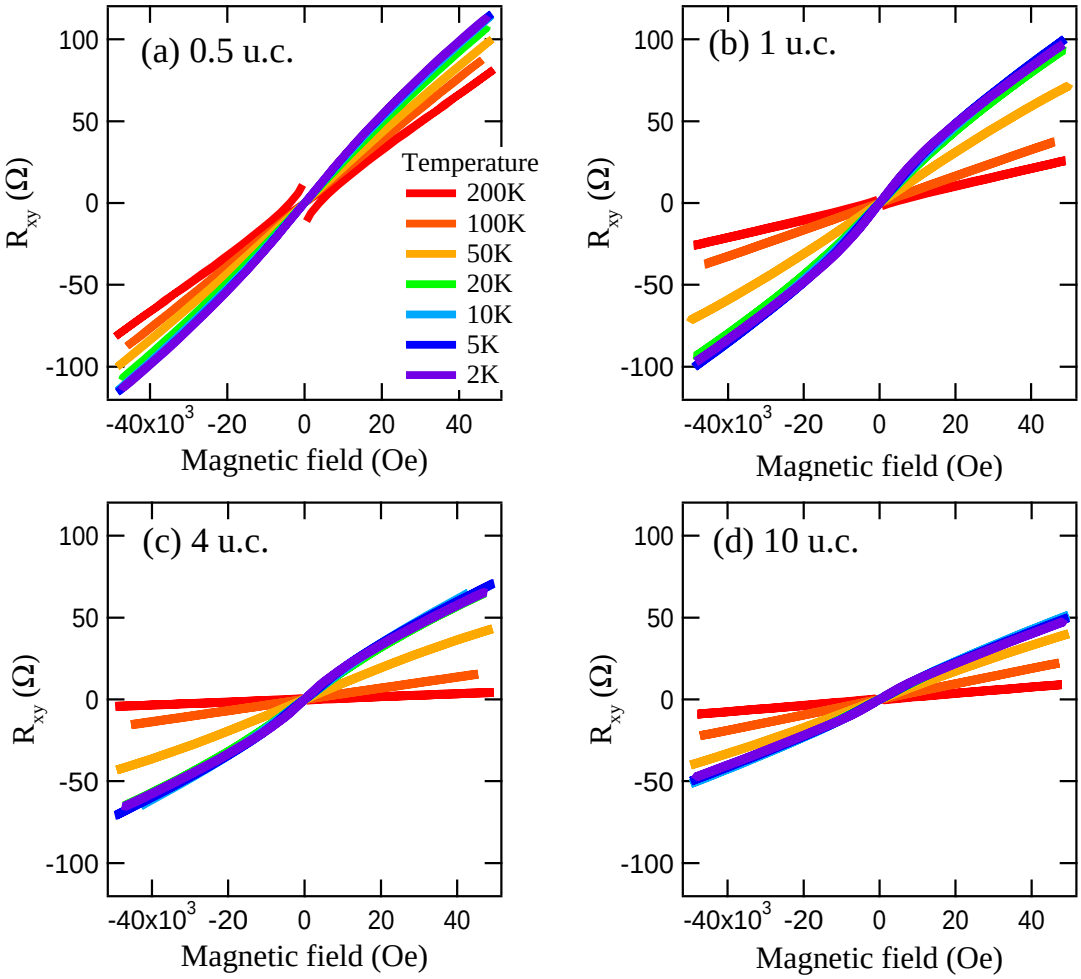

Figure 6.20: Temperature dependence of Hall resistance for different $LaTiO_3$ layer thicknesses in $SrTiO_3$

Hall resistance data of the $LaTiO_3$ / $SrTiO_3$ heterostructures were fitted by this model [14].

The equation for calculating the Hall resistance, R_H for two paralle conduction paths is

$$R_H = \frac{(\mu_1^2 n_1 + \mu_2^2 n_2) + (\mu_1\mu_2 B)^2(n_1 + n_2)}{e[(\mu_1|n_1| + \mu_2|n_2|)^2 + (\mu_1\mu_2 B)^2(n_1 + n_2)^2]}, \tag{6.4}$$

where n_1 and n_2 are the carrier densities in layers 1 and 2, and μ_1 and μ_2 are the corresponding mobilities. The sheet resistance is given by

$$R_s = \frac{1}{e\,(\mu_1 n_1 + \mu_2 n_2)}, \tag{6.5}$$

where R_s is the measured sheet resistance [14]. In the limiting cases of high and weak magnetic field these would simplify to

$$R_H \rightarrow \frac{({\mu_1}^2 n_1 + {\mu_2}^2 n_2)}{e\,(\mu_1|n_1| + \mu_2|n_2|)^2} \tag{6.6}$$

for the low field limit and

$$R_H \rightarrow \frac{1}{e\,(n_1 + n_2)} \tag{6.7}$$

for the high field limit.

The fitting results generally showed that the mobility of carriers transferred to $SrTiO_3$ dropped as the $LaTiO_3$ layer thickness was reduced.

The fitting parameters are listed in Table 6.1 and Table 6.2. The calculated curves are shown in Fig. 6.21. The fittings were performed without weighting using either a LabVIEW program developed by Dr. Bell (Table 6.2) or an Igor macro (Table 6.1).

Table 6.1 and Table 6.2 showed fitting results obtained with different initial numbers. As shown in the Tables, the resulting parameters were slightly different but reproduced the same trends. Many of the Hall resistance data sets showed only a slight nonlinearity and it was therefore difficult to perform accurate analysis with fitting ending with large error margins.

$LaTiO_3$	n_1 (cm^{-2})	μ_1 ($cm^2\ V^{-1}\ s^{-1}$)	n_2	μ_2
0.5 u.c.	$3.3 \times 10^{13} \pm 1.2 \times 10^{11}$	700 ± 10	$3.5 \times 10^{12} \pm 1.2 \times 10^{11}$	2600
1 u.c.	$2.3 \times 10^{13} \pm 1.0 \times 10^{11}$	2100 ± 26	$1.1 \times 10^{13} \pm 1.8 \times 10^{11}$	8100
4 u.c.	$3.4 \times 10^{13} \pm 1.8 \times 10^{11}$	1800 ± 40	$1.3 \times 10^{13} \pm 3.8 \times 10^{11}$	8000
10 u.c.	$3.4 \times 10^{13} \pm 2.1 \times 10^{13}$	3300 ± 200	$3.0 \times 10^{13} \pm 2.4 \times 10^{12}$	11000

Table 6.1: Carrier density and Hall mobility calculated by two carrier fitting for $LaTiO_3$ thickness dependence using an Igor macro.

In order to evaluate the reliability of the fitting results, three of the data sets, corresponding to $LaTiO_3$ thicknesses of 1, 4, and 10 unit cells, were fitted simultaneously while using the same n_1 and μ_1 values for all samples but different n_2 and μ_2 values. This model assumed that the carrier density and mobility of the interface layer is the same for all cases and only the number of deep carriers injected into the $SrTiO_3$ substrate would vary.

Table 6.3 shows the results of the simultaneous fitting procedure. The fitting curve is shown in Fig. 6.22. However, such a model resulted in $SrTiO_3$ mobilities that are

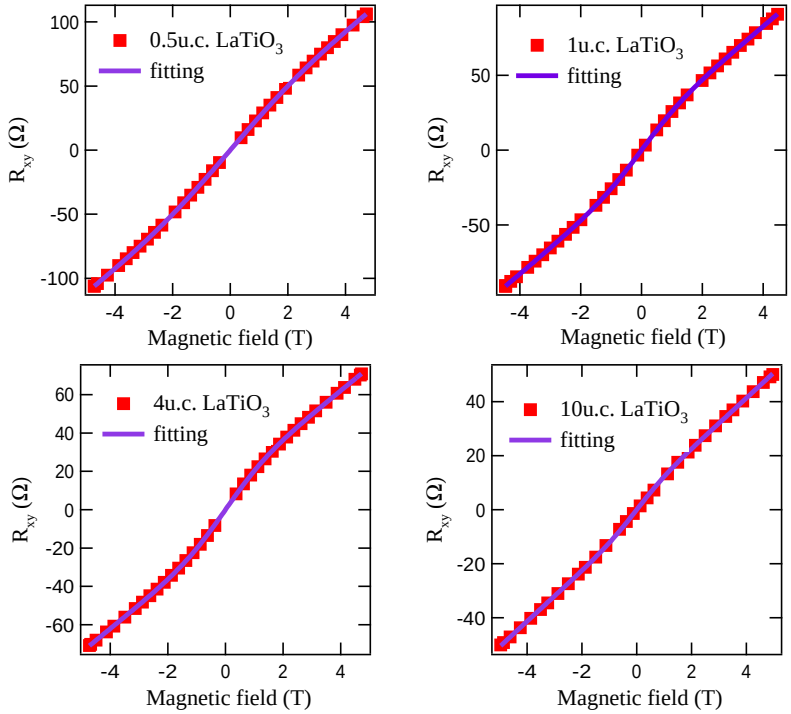

Figure 6.21: Two-layer fitting for different thicknesses of $LaTiO_3$ layers in $SrTiO_3$. Parameters are listed in Table 6.1.

$LaTiO_3$	n_1 (cm^{-2})	μ_1 ($cm^2\ V^{-1}\ s^{-1}$)	n_2 (cm^{-2})	μ_2 ($cm^2\ V^{-1}\ s^{-1}$)
0.5 u.c.	2.7×10^{13}	860	1.7×10^{12}	3300
1 u.c.	2.4×10^{13}	2100	9.2×10^{12}	9400
4 u.c.	3.8×10^{13}	2100	9.4×10^{12}	9100
10 u.c.	4.2×10^{13}	3500	2.2×10^{12}	13000

Table 6.2: Carrier density and Hall mobility calculated by two carrier fitting for $LaTiO_3$ thickness dependence using a LabVIEW program provided by Dr. Bell.

higher than 20,000, well above the known values for bulk $SrTiO_3$ and are thus unlikely to be true.

Comparison of this result with the independent fitting results in Table 6.1 can be used to draw some conclusions regarding the position of the conducting layer in the heterostructure. It is clear from both procedures that both the number of carriers and their mobilities increased in the high-mobility layer, reaching the low-temperature bulk value of about 10,000 $cm^2V^{-1}s^{-1}$ for the 10 unit cell $LaTiO_3$ layer. This appears to show that the width of the carrier spread from the $LaTiO_3$ doping layer into $SrTiO_3$ increases with the total number carriers in the doping layer. This behavior appears to be different from theoretical predictions, which have suggested that beyond a $LaTiO_3$ layer thickness of a few unit cells, the interface region width would not change.

Additionally, the mobility of the low-mobility layer is still quite high and also a function of the $LaTiO_3$ layer thickness. It is unlikely that the $LaTiO_3$ layer itself could support mobilities of 2000 to 3000 $cm^2V^{-1}s^{-1}$. It is thus reasonable to expect that the 'low-mobility' layer corresponds to the first monolayer of $SrTiO_3$, doped by the neighboring $LaTiO_3$ layer, as marked with the dashed arrows in Fig. 6.13.

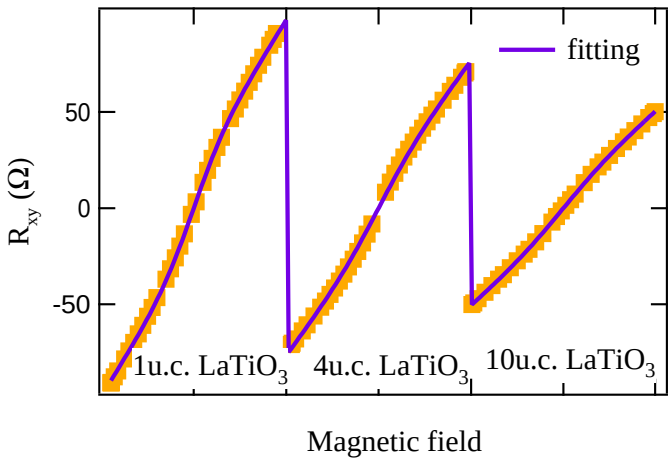

Figure 6.22: Hall resistance fitting for Fig. 6.19 with common n_1 and μ_1

Based on the two-layer fitting of the Hall resistance data, fitting of the magnetoresistance curves was also performed [15]. The equation used for fitting is

$$\frac{\Delta\rho}{\rho(0)} = \frac{(\mu_2 - \mu_1)^2 n_1 n_2 \mu_1 \mu_2 B^2}{(n_1\mu_1 + n_2\mu_2)^2 + (\mu_1\mu_2 B)^2(n_1 + n_2)^2}, \tag{6.8}$$

where parameters were the same as in Eq. 6.4.

$LaTiO_3$	n_1 (cm^{-2})	μ_1 ($cm^2\ V^{-1}\ s^{-1}$)	n_2	μ_2
1 u.c.	$2.4 \times 10^{13} \pm 5.5 \times 10^{11}$	1600 ± 170	$1.3 \times 10^{13} \pm 1.0 \times 10^{12}$	7800
4 u.c.			$2.2 \times 10^{13} \pm 1.0 \times 10^{12}$	6000
10 u.c.			$4.6 \times 10^{13} \pm 1.1 \times 10^{12}$	9100

Table 6.3: Carrier density and Hall mobility of Hall resistance in Fig.6.19 calculated by two carrier fitting.

By using this equation, MR results in Fig. 6.5 were fitted. The fitting result and parameters are shown in Fig. 6.23 and Table 6.4. Compared with the Hall resistance fitting parameters in Table 6.1, the numbers differed slightly and had larger error margins but showed the same general trends as was seen in the Hall resistance fitting. The carrier density for deep carriers in $SrTiO_3$ increased with $LaTiO_3$ thickness. A slight increase of carriers at the $LaTiO_3$ / $SrTiO_3$ interface layer was also observed. The numerical differences may reflect the difficulty of approximating the carrier distribution at the $LaTiO_3$ interface with a two-layer model, which assumes a sharp boundary between the two layers. In reality, a gradual drop of carrier density and increase of mobility should be assumed. Unfortunately, neither the Hall resistance data nor the magnetoresistance data has sufficient distinct features do statistically justify the addition of more fitting parameters.

The fitting results can be compared with the predictions made by Okamoto *et al.* based on first-principles calculation [3]. Ohtomo *et al.* have also shown experimental results for the spread of Ti^{3+} in $SrTiO_3$ for $LaTiO_3$ / $SrTiO_3$ superlattices [16]. This carrier spread limits the dimensionality of the $LaTiO_3$ heterostructures.

One possibility of controlling carrier confinement would be to attempt to deplete carriers from $SrTiO_3$ by field effect. Magnetoresistance and Hall resistance behavior under applied bias field is the subject of the next Section.

6.3.5 Back gate bias

Fig. 6.24, Fig. 6.25 and Fig. 6.28 show the MR behavior under electric field applied from a back gate electrode for a 10 unit cell $LaTiO_3$ sample. A copper plate was used as a back-gate electrode. Contact to the substrate was made with silver paste. Ohmic contacts to top electrodes were made by wirebonding Al wires through the capping layer to the $LaTiO_3$ heterostructures. The back-gate leak currents were 1 nA for all V_G values up to 100 V.

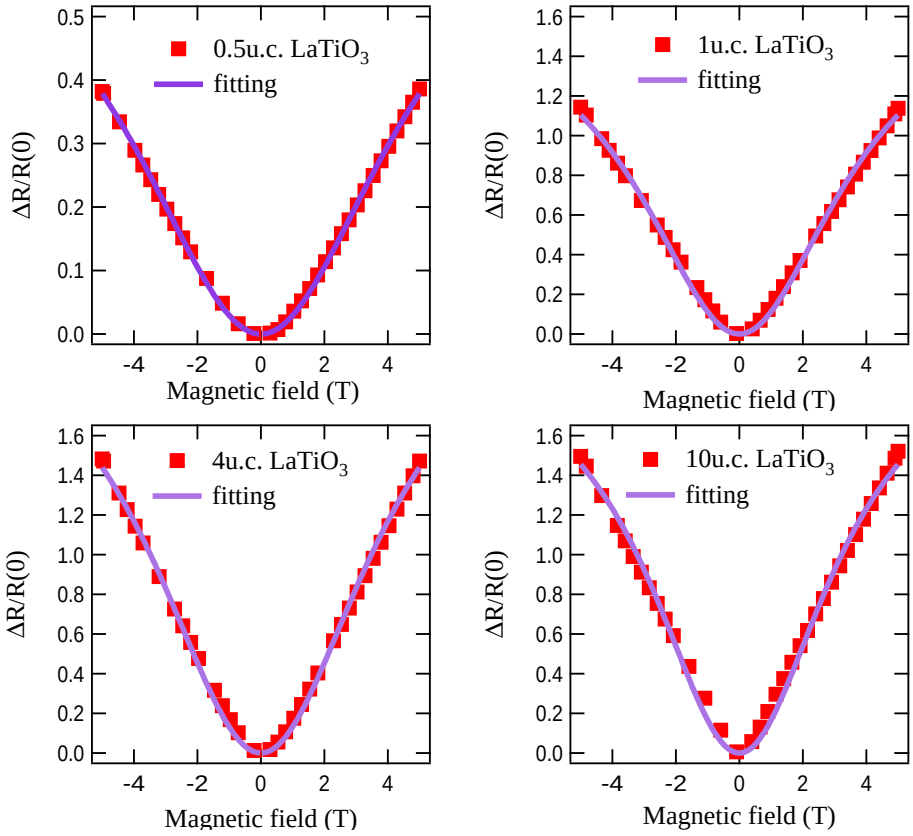

Figure 6.23: Two-layer fitting for MR for different thicknesses of $LaTiO_3$ layers in $SrTiO_3$

$LaTiO_3$ thickness	n_1 (cm^{-2})	μ_1 ($cm^2\ V^{-1}\ s^{-1}$)	n_2 (cm^{-2})	μ_2 ($cm^2\ V^{-1}\ s^{-1}$)
0.5 u.c.	1.5×10^{13}	710	4.4×10^{12}	4400
1 u.c.	1.1×10^{13}	1400	9.9×10^{12}	13000
4 u.c.	1.2×10^{13}	1200	1.1×10^{13}	15000
10 u.c.	3.0×10^{13}	1500	2.6×10^{13}	16000

Table 6.4: Carrier density and Hall mobility calculated by two-carrier fitting for $LaTiO_3$ thickness dependence of MR in Fig. 6.5. Initial numbers for parameters came from Table 6.1

$SrTiO_3$ is known for having a very high dielectric constant at low temperature [17]. Due to the large dielectric constant, it is possible to apply high enough fields for effective carrier modulation even for a substrate thickness of 0.5 mm. A rough estimate for carrier density modulation at the interface is 1 to 2×10^{11} V^{-1} cm^{-2} for 0.5 mm thick bulk $SrTiO_3$ at 10 K or less.

By applying a negative gate bias, it is possible to tune the potential at the interface [18], depleting high-mobility carriers from the $SrTiO_3$ substrate. Indeed, this type of behavior can be seen in Fig. 6.24. At zero gate bias, a sharp increase of resistance can be seen with magnetic field. Upon application of a negative gate bias, which would be expected to deplete carriers from the $SrTiO_3$ substrate, the MR slope drops to less than half at $V_G = -100$ V. This result is consistent with the removal of high-mobility carriers from the heterostructure. At high negative gate bias, the MR behavior resembles the magnetic field dependence of resistance seen in thinner $LaTiO_3$ samples [Fig. 6.5] that had fewer carriers distributed in $SrTiO_3$. By comparing the gating data in Fig. 6.24 and the $LaTiO_3$ layer thickness dependence data in Fig. 6.5, it is clear that gating has the same phenomenological effect as the doping layer thickness change. Due to the small carrier density modulation amplitude, it is also clear that only the low-density deep carriers in $SrTiO_3$ can be affected. As shown by the Hall resistance and MR field dependence fitting results, the mobile carrier density in the higly doped region is 10 to 100 times larger than the field-effect modulation. The gating bias cannot therefore change the highly-doped interface layer carrier density.

A similar conclusion can be drawn from looking at the in-plane magnetoresistance data in Fig. 6.25. Under zero gate bias, the MR behavior is similar to the data shown in Fig. 6.12. The in-plane field gating experiments were done in a geometry where the magnetic field was parallel to the current flow and also parallel to the step edges of the substrate. The data shown in Fig. 6.12 for a 10 unit cell $LaTiO_3$ sample measured for current flow parallel to steps shows a small negative MR peak at low fields. This was not seen for the same sample in the gating experiment likely because the sample was mounted on a rotator stage and thus it was difficult to guarantee that the sample was aligned accurately along the field. The data in Fig. 6.25 may thus have a small out-of-plane MR component.

By applying a -100 V gate bias, the behavior changed from positive MR to showing a pure negative MR component, comparable to the behavior of the thinnest, 1 unit cell $LaTiO_3$ layer sample under the same measurement geometry, shown in Fig. 6.12. This is consistent with the assumption that the gating field eliminated the high-mobility

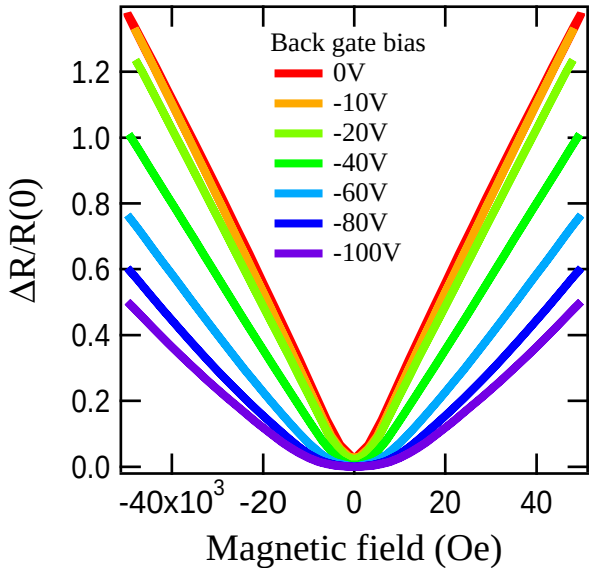

Figure 6.24: Magnetoresitance for the magnetic field applied out of plane for a 10 unit cell $LaTiO_3$ layer embedded in $SrTiO_3$ for various negative back gate bias values, measured at 5 K.

deep carriers from the heterostructure, essentially converting the 10 unit cell $LaTiO_3$ sample to a 1 unit cell $LaTiO_3$ case and thus significantly improving the confinement of carriers in the vicinity of the $LaTiO_3$ doping layer in the heterostructure.

A similar experiment has been done by Ngai *et al.* with a defect-rich Ar-bombarded $SrTiO_3$ surface [19] and Caviglia *et al.* at the $LaAlO_3$ / $SrTiO_3$ interace [20]. Both authors reported the presence of positive MR at low temperature. In the case of Nagi *et al.*, a crossover from positive to negative MR was also seen [Fig. 6.26], with explanations being either weak localization or Rashba spin orbit coupling near the surface, at around $V_G \sim -40V$. The $LaTiO_3$ heterostructures did not show a crossover to negative MR in out-of-plane measurements and in any case, this would not be expected, since no signature of weak localization like behavior was seen in thickness dependence measurements. This may be due to the very high carrier density in the $LaTiO_3$ layer even at $V_G = -100$ V. In the case of Caviglia *et al.*, the reported MR behavior is quite similar [Fig. 6.27]. The explanation that Caviglia offered is based on the assumption that the $LaAlO_3$ / $SrTiO_3$ interface is affected by Rashba spin-orbit interaction, which would be caused by the intrinsic asymmetry of the heterostructure. If the negative MR does indeed originate in the first $SrTiO_3$ monolayer at the $LaTiO_3$ /

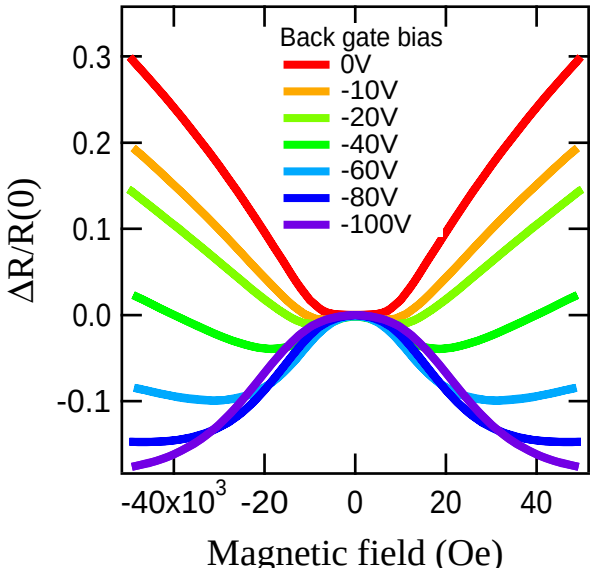

Figure 6.25: In plane field magnetoresitance for a 10 unit cell $LaTiO_3$ layer embedded in $SrTiO_3$ under geative back-gate bias at 5 K.

$SrTiO_3$ interface, inversion symmetry for the Ti atoms in that layer would be broken. There may also be a significant internal field in the heterostructure and possibly the effective mass of carriers would be a function of distance from the interface, as shown by the two-layer Hall resistance analysis.

Although the dielectric properties of $SrTiO_3$ would be expected to be identical for the $LaTiO_3$ heterostructures used in this work and the $LaAlO_3$ interfaces studied by Caviglia *et al.*, with Ti ions at the interface obtaining a formal valence of close to 3+ with a spin -1/2 local moment [21] and $SrTiO_3$ carrier mobility exceeding 10,000 $cm^2\ V^{-1}\ s^{-1}$ near the interface[22], there are also differences. Most importantly, the $LaAlO_3$ interfaces do not show nonlinear Hall resistance and thus the presence of multiple conduction layers has not been considered. While the possibility of Rashba spin-orbit interaction in $LaTiO_3$ / $SrTiO_3$ is possible, it is difficult to distinguish the effect from a simple electrostatic carrier density change in $SrTiO_3$ because the conduction of by carriers in deep $SrTiO_3$ might be predominant for the $LaTiO_3$ heterostructures.

Based on the gated MR measurements, it was thus not obvious whether negative MR was caused by spin-orbit effects or not. Further analysis would be necessary and possibly also a measurement where the angle dependence of the applied magnetic field can be measured more accurately.

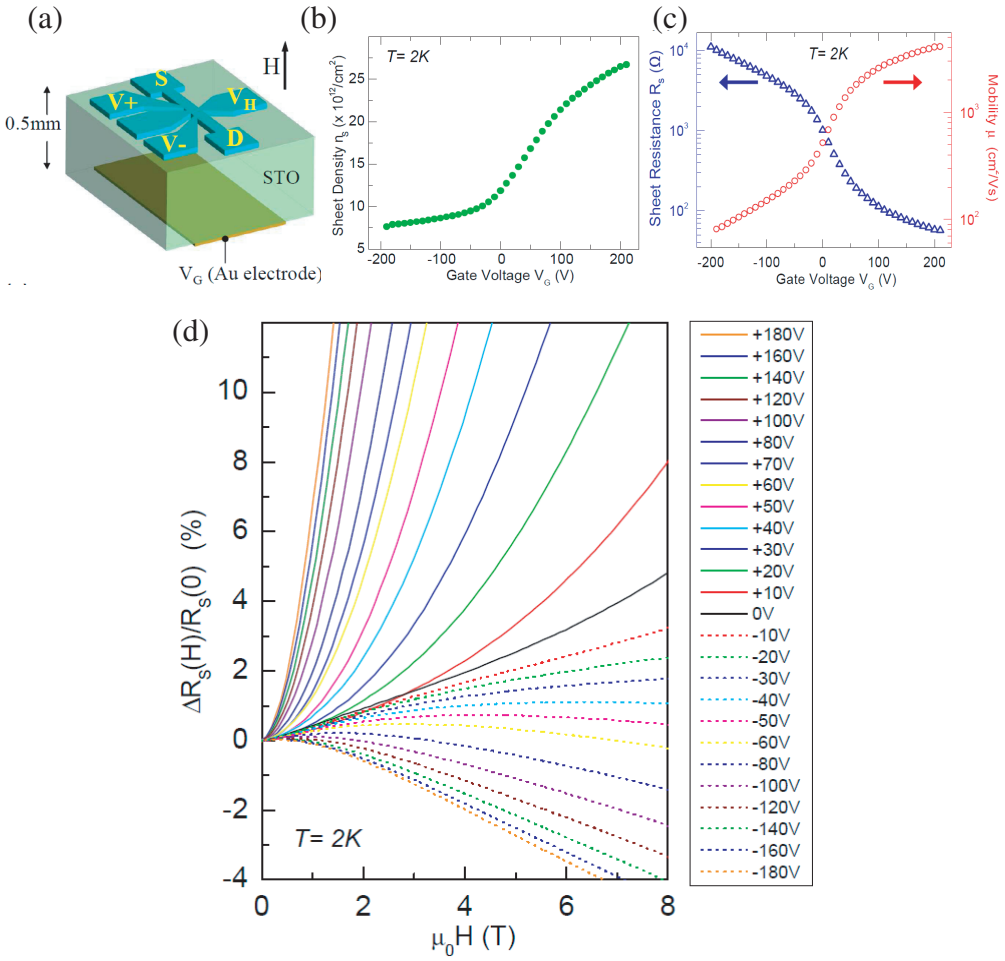

Figure 6.26: Electrical characterization of Ad-irradiated $SrTiO_3$ devices as a function of V_G at T=2 K. **(a)** Schematic of device. **(b)** Sheet carrier density versus V_G. **(c)** R_S and μ versus V_G. **(d)** Electric modulation of the MR. A crossover from positive to negative MR is observed going from high to low μ [19].

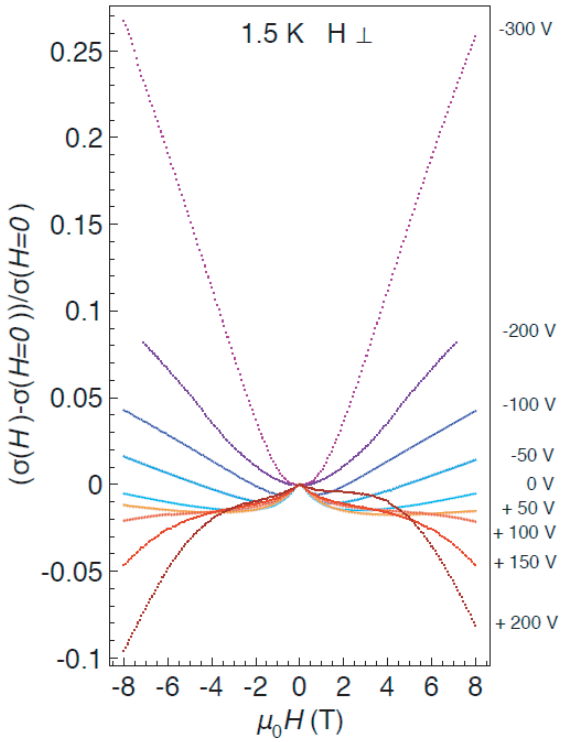

Figure 6.27: Magnetoconductance of the $LaAlO_3$ / $SrTiO_3$ interface under electric and magnetic fields measured at 1.5 K in perpendicular magnetic field for applied gate voltages [20].

The Hall resistance was also measured under electric field. The results are shown in Fig. 6.28. Generally, Hall resistance showed an increase with increasing negative back gate bias, which would correspond to a reduction of carrier density. The behavior was qualitatively similar to reducing the thickness of the $LaTiO_3$ layer, as shown in Fig. 6.19.

The gated Hall resistance measurement data were also fitted by the two carrier model, discussed in Section 6.4. The fitting parameters are shown in Table 6.5. Since all measurements were done with the same heterostructure, and it is impossible to change the carrier density of the heavily-doped interface layer by gating, the fitting was again done by assuming a single carrier density/mobility parameter pair, n_1, μ_1 for all of bias values. All hall resistance curves were fitted simultaneously, as shown in Fig. 6.29.

As shown in Table 6.5, the carrier density (n_2) and Hall mobility (μ_2) of doped $SrTiO_3$ gradually dropped by increasing the gate bias. Hall mobilities for the deep carriers were quite high, but still below 10,000 $cm^2V^{-1}s^{-1}$ and thus within reasonable range

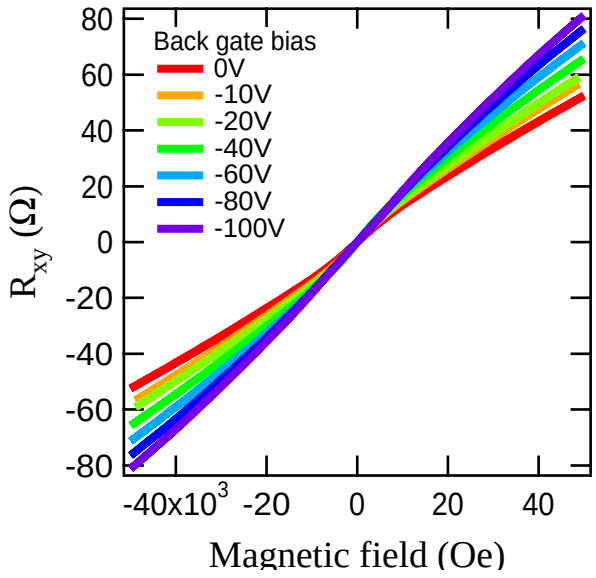

Figure 6.28: Hall resistance of a 10 unit cells of $LaTiO_3$ layer in $SrTiO_3$ under negative back gate bias at 5 K.

and similar to the two-layer tanalysis of $LaTiO_3$ layer thickness data. The drop of deep carrier density under bias was thus both qualitatively and quantitatively similar to reducing the $LaTiO_3$ doping layer thickness (Table 6.1). This appears to indicate that carrier density changes dominate the gating results.

If the gate voltage is switched to positive polarity, carriers would be accumulated in the Hall bar region. However, unlike the negative bias conditions, the $LaTiO_3$ / $SrTiO_3$ superlatttices did not show a big difference in MR behavior when a positive bias was applied, as shown in Fig. 6.30. This was probably due to the large carrier desity present in the $LaTiO_3$ layer. For the $SrTiO_3$ inetrface, the estimated carrier density was 3.3×10^{13} cm^{-2} while the expected field-effect modulation is of the order of 2×10^{11} cm^{-2}. While the back-side gate bias can make the potential well at the interface sharper, and thus limit the distribution of existing carriers in the substrate, it is not possible to increase the density of carriers by more than about 1 % at the densities present in these $LaTiO_3$ heterostructures. The situation may be quite different for lower donor-density systems, like the $SrTiO_3$ interface described by Ngai *et al.* [19], where carrier accumulation was apparently seen.

In terms of determining the effective thickness of the heterostructures, comparison of the thickness dependence of $LaTiO_3$ layer with the back gate experiments, it is

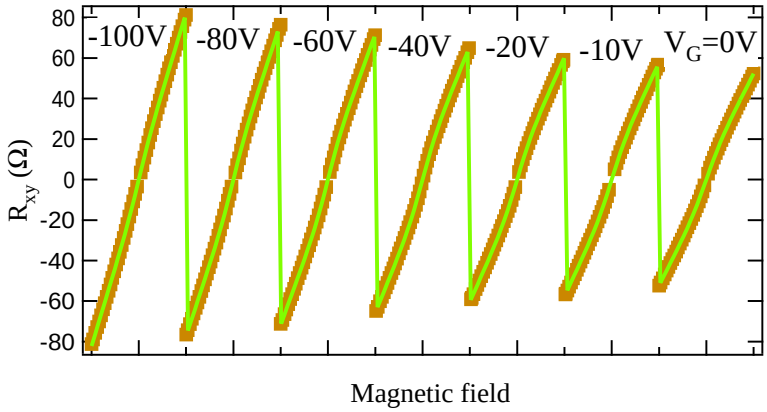

Figure 6.29: Two carrier fitting results according to Eq. 6.4 with identical n_1 and μ_1 used for all bias values.

quite clear that carriers exist not only in the $LaTiO_3$ layer but also deep in the $SrTiO_3$ substrate. Unless additional confining potential adjustments are made, for example by applying an electric field, the carrier spread strongly affect the transport properties of the heterostructures.

Gate bias	n_1 (cm^{-2})	μ_1 ($cm^2\ V^{-1}\ s^{-1}$)	n_2	μ_2
0 V	$3.3 \times 10^{13} \pm 3.6 \times 10^{11}$	2200 ± 30	$3.1 \times 10^{13} \pm 8.1 \times 10^{11}$	8200
-10 V			$2.5 \times 10^{13} \pm 7.4 \times 10^{11}$	7800
-20 V			$2.2 \times 10^{13} \pm 7.1 \times 10^{11}$	7700
-40 V			$1.7 \times 10^{13} \pm 6.6 \times 10^{11}$	7300
-60 V			$1.3 \times 10^{13} \pm 6.1 \times 10^{11}$	6800
-80 V			$9.7 \times 10^{12} \pm 5.8 \times 10^{11}$	6800
-100 V			$6.3 \times 10^{12} \pm 5.7 \times 10^{11}$	6000

Table 6.5: Carrier density and Hall mobility of Hall resistance in Fig. 6.28 calculated by two carrier fitting.

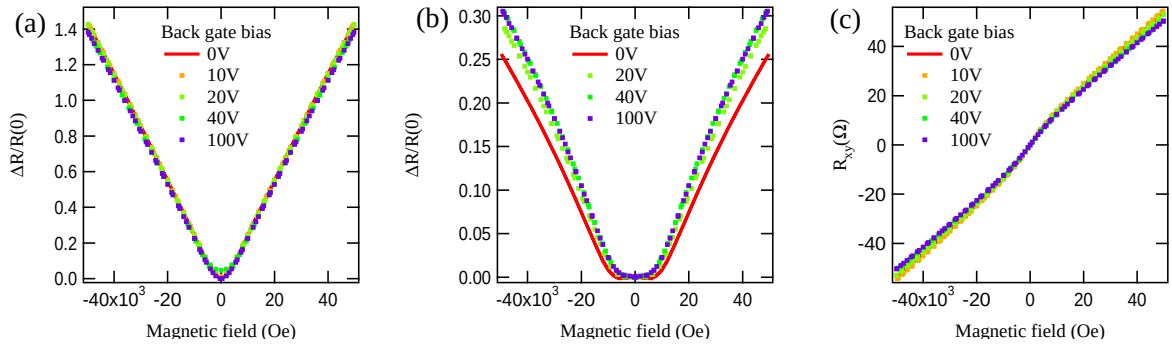

Figure 6.30: Magnetoresitance of a 10 unit cell of $LaTiO_3$ layer under positive back-gate bias, **(a)** out-of-plane field, **(b)** in-plane field, and **(c)** Hall resistance

.

6.4 Summary

As a summery for this Chapter, magnetoresistance and Hall resistance were measured for different $LaTiO_3$ doping layer thicknesses embedded in $SrTiO_3$. A strong $LaTiO_3$ layer thickness dependence was found for MR of both out of plane and in plane field directions. The cause for the appearance of negative MR was not determined, although based on literature references, spin-orbit coupling may be an important contributing factor, considering the intrinsic asymmetry of the heterostructures. The possibility of charge or spin order at $LaTiO_3$ / $SrTiO_3$ interface, as has been predicted by Pentcheva *et al.* [4] cannot be ruled out either, but would require additional experiments to confirm. For very low $LaTiO_3$ coverages, below 1 unit cells, it is also important to consider percolation effects.

Signatures of ferromagnetic ordering was sought, but no evidence for the existence of magnetic order, that is non-symmetric field dependence, could be seen in the magnetoresistance data. For the lowest doping densities of about 0.3 unit cells of $LaTiO_3$, a metal-insulator transition was seen, but this loss of conductivity could not be regained under a magnetic field. [Fig. 5.10 and Fig. 5.11].

Based on the Hall measurements, it was concluded that the $LaTiO_3$ / $SrTiO_3$ heterostructures contain multiple parallel conducting layers with quite different carrier densities and mobilities. Specifically, the data supports a model where a high-density / low-mobility layer exists at the immediate interface, possibly consisting of the first $SrTiO_3$ unit cell layer, as suggested by the dramatic effect of surface step orientation on the magnetoresistance behavior. Another layer consists of deep high-mobility carriers

at very low carrier densities in $SrTiO_3$. These carriers can be eliminated by applying a depleting electric field. A two-layer model was used to analyze the Hall resistance and magnetoresistance data. Fitting of all data resulted in a consistent model for the behavior of carriers in these heterostructures. The carrier spread, which distributes Ti^{3+} states deep in $SrTiO_3$ may explain Shubnikov-de Haas oscillations were seen at fields of up to 7 T. The case might be similar to the $LaAlO_3$ / $SrTiO_3$ system reported by Siemons *et al.* [23].

Moreover, tuning the carrier density on the $SrTiO_3$ side of the $LaTiO_3$ / $SrTiO_3$ interface by back gate bias, magnetoresistance and Hall resistance showed similar behavior which could be interpreted as being caused by a reduction of carriers spread into $SrTiO_3$. It was found that sharpening the confining potential in $LaTiO_3$ heterostructure by electric field is functionally equivalent to reducing the thickness of the $LaTiO_3$ layer. Unlike theoretical predictions of $SrTiO_3$ / $LaTiO_3$ / $SrTiO_3$ heterostructures, it was found that increasing the $LaTiO_3$ layer thickness, even in the 4 to 10 unit cell range, strongly affect the carrier spread into $SrTiO_3$.

References

[1] T. Mihara, K. Shibuya, T. Ohnishi, H. Koinuma and M. Lippmaa *Thin Solid Films* **486**, 63 (2005).

[2] A. Brinkman, M. Huijben, M. Van Zalk, J. Huijben, U. Zeitler, J. C. Maan, W. G. Van Der Wiel, G. Rijnders, D. H. A. Blank and H. Hijgenkamp *Nature* **6**, 493 (2007).

[3] S. Okamoto, A. J. Mills and N. A. Spaldin *Physical Review Letters* **97**, 056802 (2006).

[4] R. Pentcheva and W. E. Pickett *Physical Review Letters* **99**, 016802 (2007).

[5] J. Inaba and T. Katsufuji *Physical Review B* **72**, 052408 (2005).

[6] O. N. Tufte and P. W. Cahpman *Physical Review* **155**, 796 (1967).

[7] D. Olaya, F. Pan, C. T. Rogers and J. C. Price *Applied Physics Letters* **80**, 2928 (2002).

[8] Y. Kawaguchi, H. Kitahara and S. Kawaji *Surface Science* **73**, 520 (1978).

[9] G. Herranz, M. Basletic, M. Bibes, C. Carretero, E. Tafra, E. Jacquet, K. Bouzehouane, C. Deranlot, A. Hamzic, J. -M. Broto, A. Barthelemy and A. Fert *Physical Review Letters* **98**, 216803 (2007).

[10] Y. Kozuka, H. Hikita T. Susaki and H. Y. Hwang *Physical Review B* **76**, 085129 (2007).

[11] M. B. Shalom, C.W. Tai, Y. Lereah, M. Sachs, D. Rakhmilevitch, A. Palevski and Y. Dagan *Physical Review B* **80**, 140403(R) (2009).

[12] C. Bell, S. Harashima, Y. Kozuka, M. Kim, B. G. Kim, Y. Hikita and H. Y. Hwang *Physical Review Letters* **103**, 226802 (2009).

[13] T. Manago, N. Nishizaki, S. Ishiba, H. Geka and I. Shibasaki *Journal of Crystal Growth* **311**, 1711 (2009).

[14] D. K. Schroder *Semiconductor Material And Device Characterization, 2nd ed* (1998).

[15] H. H. Wieder *Applied Physics Letters* **25**, 206 (1974).

[16] A. Ohtomo, D. A. Muller, J. L. Grazul and H. Y. Hwang *Nature* **419**, 378 (2002).

[17] T. Sakudo and H. Unoki *Physical Review Letters* **26**, 851 (1971).

[18] K. Hirakawa, H. Sakaki and J. Yoshino *Physical Review Letters* **54**, 1279 (1985).

[19] J. H. Nagi, Y. Segal, F. J. Walker, S. Ismail-Beigi, K. Le Hur and C. H. Ahn *Condmat material*, arXiv:0909.2834v1 (2009).

[20] A. D. Caviglia, M. Gabay, S. Gariglio, N. Reyren, C. Cancellieri and J. M. Triscone *Condmat material*, arXiv:0912.3731v1 (2009).

[21] Y. Tokura, Y. Taguchi, Y. Okada, Y. Fujimori and T. Arima *Physical Review Letters* **70**, 2126 (1993).

[22] O. Copie, V. Garacia, C. Bodefeld, C. Carretero, M. Bibes, G. Herranz, E. Jacquest, J. -L. Maurice, B. Vinter, S. Fusil, K/ Bouzehouane, H. Jaffres and A. Barthelemy *Physical Review Letters* **102**, 216804 (2009).

[23] W. Siemons, G. Koster, H. Yamamoto, W. A. Harrison, G. Lucovsky, T. H. Geballe, D. H. A. Blank and M. R. Beasley *Physical Review Letters* **98**, 196802 (2007).

Chapter 7

Capping layer effect on $LaTiO_3$ / $SrTiO_3$

The transport properties of $LaTiO_3$ / $SrTiO_3$ heterostructures were discussed in Chapters 5 and 6. However, a remaining issue is the possibility of conductivity at the interface between the $LaTiO_3$ layer and the $SrTiO_3$ capping layer, mostly in the $SrTiO_3$ capping layer itself. The capping layer is necessary to prevent surface depletion effects from affecting the transport properties of the $LaTiO_3$ layer. In this Chapter, conductivity at the interface between $LaTiO_3$ and $SrTiO_3$ capping layer and in the capping layer itself are discussed.

7.1 $CaHfO_3$

As was discussed in Chapter 2, $CaHfO_3$ is known as wide gap insulator, with a band gap above 5 eV [1]. Due to its excellent insulator properties, it has been used as gate insulator in $SrTiO_3$-based field-effect transistors[2].

In order to check the effect of the capping layer on the heterostructure transport, some samples were prepared where $CaHfO_3$ was used as a capping layer instead of $SrTiO_3$. As a first step, a $CaHfO_3$ capping layer was grown directly on a clean $SrTiO_3$ surface. The resistance of a 25 unit cell thick $CaHfO_3$ layer on a pre-annealed $SrTiO_3$ substrate is shown in Fig. 7.1. The $CaHfO_3$ film was deposited under 10^{-6} Torr of oxygen. The substrate temperature was 500 °C, which is the same growth temperature and pressure as was used for $SrTiO_3$ capping layers. As expected, the as-deposited $CaHfO_3$ / $SrTiO_3$ film showed a metallic resistance behavior before post-annealing. The large resistance ration between 300 K and 4 K resistances shows that the conductivity is due to oxygen vacancies doping the surface layer of the $SrTiO_3$ substrate. Indeed, after post-annealing, the resistivity behavior changed completely, and an insulating

temperature dependence was seen instead. It is interesting that there was still an initial drop of resistance down to about 100 K before a sharp upturn was seen. This is likely due to an insufficient annealing time and the relatively large thickness of the insulator layer. It is known that a $CaHfO_3$ film is an excellent oxygen diffusion barrier, so it is difficult to fully oxygenate the underlying interface by air annealing, even at 400 °C.

One way to solve this problem is to grow the $CaHfO_3$ at a higher oxygen pressure, thereby reducing the density of oxygen vacancies that form in the $SrTIO_3$ substrate during film growth. Following the example of earlier FET work, $CaHfO_3$ cap layer films were grown at 7×10^{-3} Torr of oxygen but still at 500 °C. For $CaHfO_3$ films grown under similar conditions, insulating behavior has been seen before. Fig. 7.2 shows the resistance behavior of approximately 25 unit cell thick $CaHfO_3$ film grown at 7×10^{-3} Torr on top of a 1 unit cell $LaTiO_3$ / $SrTiO_3$ heterostructure. Surprisingly, the resistance behavior was insulating. Even when the thickness of the $LaTiO_3$ layer was increased to well above 1 unit cell, the resistance behaved remained insulating. This may be caused by band bending at the interface [Fig. 7.3] or change of the $LaTiO_3$ phase to an insulator. Experiments by hard-xray photoemission angle profiling are planned to find an answer to this problem.

It is interesting to note that the number of dopands introduced at the interface for a 1 u.c. $LaTiO_3$ layer is similar to what has been proposed for the $LaAlO_3$ / $SrTiO_3$ system. The band gap of $CaHfO_3$ is similar to $LaAlO_3$. Since $CaHfO_3$ is a 2/4 oxide, i.e. Ca is in 2+ state and Hf is in 4+ state, there is no polarity change at this interface. It is therefore an open question why the $LaAlO_3$ / $SrTiO_3$ interface supports metallic conductivity, while the $CaHfO_3$ / $LaTiO_3$ / $SrTiO_3$ system does not, even for thick $LaTiO_3$ layers.

7.2 $BaTiO_3$

As shown in the previous section, $CaHfO_3$ had a strong effect on the transport properties, and presumably the band structure of the $LaTiO_3$ / $SrTiO_3$ heterostructure. Another attempt was therefore made to find another capping layer material that would have a narrower band gap and would not affect the heterostructure as much as $CaHfO_3$ did.

Another simple choice was to use $BaTiO_3$ as capping layer. The physical properties of $BaTiO_3$ have been presented in in Chapter 2. $BaTiO_3$ has a similar band gap to $SrTiO_3$ and it has the additional advantage that it does not break the *B*-site titania sublattice.

As before, an approximately 25 unit cell thick capping layer was grown. The

thickness was estimated from RHEED oscillations and separate deposition rate measurements. $BaTiO_3$ was grown on $SrTiO_3$ under at 10^{-6} Torr of oxygen and 500 °C. The growth conditions were the same as for $SrTiO_3$ capping layer to preserve the $LaTiO_3$ phase. These samples also showed an insulating behavior, even though the cap layer was grown at a relatively low temperature and low oxygen pressure. Then, $BaTiO_3$ was deposited on a 1 unit cell $LaTiO_3$ / $SrTiO_3$ heterostructure. The final film still showed an insulator behavior, which was unexpected.

An appropriate answer why heterostructure conductivity was lost is not yet available. It is clear from the very high mobilities observed in the $LaTiO_3$ / $SrTiO_3$ system that the contribution of the cap layer is minor, if it is detectable at all. the solution to this problem will hopefully be found once the photoemission data for these samples becomes available.

7.3 Summary

The effect of $CaHfO_3$ and $BaTiO_3$ capping layers on the transport properties of $LaTiO_3$ / $SrTiO_3$ heterostructures was studied. In both cases, an unexpected insulating behavior was observed. For $CaHfO_3$ this may be due to large band offsets, considering the $\sim$ 5.5 eV band gap of $CaHfO_3$.

In order to select another nonconducting but narrower gap cap layer material, a $BaTiO_3$ cap layer was grown on a $LaTiO_3$ / $SrTiO_3$ heterostructure. Regardless of the thickness of the $LaTiO_3$ layer, the $BaTiO_3$ / $LaTiO_3$ / $SrTiO_3$ heterostructures showed insulating behavior. The contribution of the $SrTiO_3$ capping layer to the conductivity of the heterostructures thus remains an open question. however, the capping layer material tests opened up new interesting questions regarding the conductivity of an interface between $SrTiO_3$ and a wide-gap insulator, even when the interface is deliberately doped with La, which would normally introduce carriers into $SrTiO_3$.

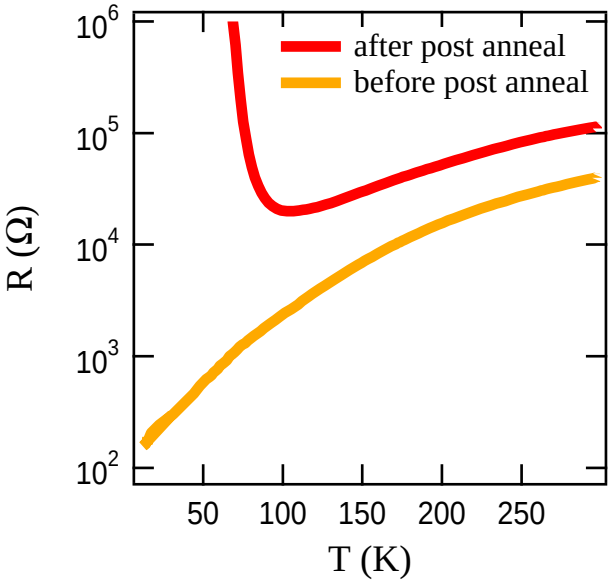

Figure 7.1: Temperature dependence of resistance for a 25 unit cell $CaHfO_3$ capping layer grown directly on a pre-annealed $SrTiO_3$ after deposition and after post-annealing at 400 °C in air.

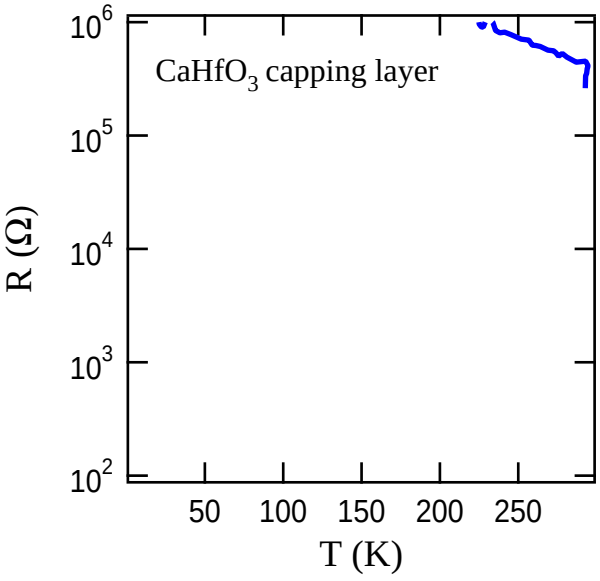

Figure 7.2: Temperature dependence of resistance of a 25 unit cell $CaHfO_3$ capping layer on a 1 unit cell $LaTiO_3$ / $SrTiO_3$ heterostructure.

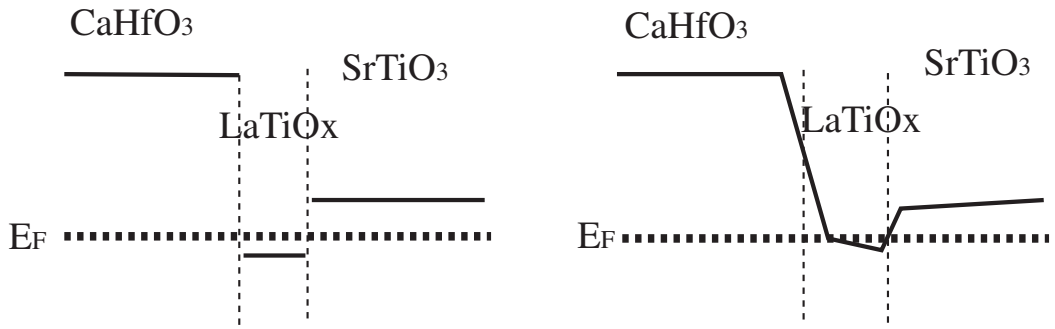

Figure 7.3: Illustration of possible band bending in a $CaHfO_3$ / $LaTiO_3$ / $SrTiO_3$ heterostructure, assuming that the $LaTiO_3$ layer is Sr doped and can be approximated as heavily n-type $SrTiO_3$.

References

[1] J. Robertso *Journal of Vacuum Science and Technology B* **18**, 1785 (2000).

[2] K. Shibuya, T. Ohnishi, T. Uozumi, T. Sato, M. Lippmaa, M. Kawasaki, K. Nakajima T. Chikyow and H. Koinuma *Applied Physics Letters* **88**, 212116 (2006).

Chapter 8

Conclusion

In this study, the focus was on the $LaTiO_3$ / $SrTiO_3$ system with an original aim of finding evidence for the existence of various forms of electronic ordering at these interfaces, as has been predicted by theory. The main task was to make grow epitaxial oxide heterostructures and to study the possibility of tuning the carrier density and electronic phases in $LaTiO_3$ / $SrTiO_3$ heterostructures by changing the doping layer thickness, temperature or by applying magnetic or electric fields.

$LaTiO_3$ heterostructures were grown by pulsed laser deposition and various forms of transport characterization were performed. A metal-insulator transition was observed at low temperature when the $LaTiO_3$ layer thickness in a $SrTiO_3$ / $LaTiO_3$ / $SrTiO_3$ heterostructure was reduced to below 0.5 unit cells. Several mechanisms that might be responsible for the MIT were considered but no clear signature of magnetic or charge ordering phenomena was found based on transport measurements. Other techniques, such as linear or circular dichroism measurements have been suggested as possible solutions to detecting ordered phases in interface layers.

Magnetoresistance and Hall resistance were also measured for different $LaTiO_3$ layer thicknesses. A strong doping layer thickness dependence was found for magnetoresistance. The magnetoresistance behavior was also anisotropic, with out-of-plane MR being positive and in-plane MR showing a crossover between positive and negative behavior depending on the density and distribution of carriers in the heterostructures. The heterostructures were therefore considered to be two-dimensional. Several mechanisms for the negative in-plane MR response were considered, including the possibility of a charge-ordered occurring at the $LaTiO_3$ / $SrTiO_3$ interface and the influence of spin-orbit coupling in the strongly nonsymmetric structure of the $LaTiO_3$ / $SrTiO_3$ interface. No hysteretic or nonsymmetric behavior was seen in the magnetoresistance

measurements, which appear to rule out ferromagnetic ordering of the $3d^1$ electrons at the interface.

All transport data supported a model of multiple parallel conducting layers at the interface, one being a low-carrier-density and high-mobility layer and the other a high-carrier-density and low-mobility interface layer. This conclusion was made based on the observation of non-linear Hall resistance for all $LaTiO_3$ thickness. The Hall and magnetoresistance data was successfully fitted with the multiple conducting layer model. Typical carrier density and mobility numbers were extracted and found to be consistent between samples and between measurements. It was found that carrier spread deep into the $SrTiO_3$ substrate explaining the presence of a very high-mobility layer. A gradual change of carrier density and mobility in the heterostructure explains why the heterostructures did not show Shubnikov-de Haas oscillations.

$SrTiO_3$ / $LaTiO_3$ /$SrTiO_3$ heterostructures were grown with different LaTiO3 thicknesses and transport properties were studied under magnetic and electric fields. Thinner $LaTiO_3$ layers showed strong negative MR, and a nonlinear Hall resistance. No direct evidence of ordered phases was seen in MR measurements. Moreover, tuning the carrier density in $SrTiO_3$ was successful. The deep carrier tail in the $SrTiO_3$ substrate could be eliminated by a negative back gate bias. Magnetoresistance and Hall resistance showed similar behavior under a gating field as for decreasing $LaTiO_3$ layer thickness.

In this study, quasi-2D behavior was seen, but it was also recognized that spilling of carriers into SrTiO3 limits the carrier confinement.

List of Figures

List of Tables

Acknowledgments

At the top of the list, I would like to express my deepest gratitude to my advisor, Prof. Mikk Lippmaa in the Department of Advanced Materials Science, University of Tokyo for his continuing support and education and giving me great opportunities in my master course. Without his particular patience and courtesy, this thesis would have never finished. Through daily discussion and his attitude to the research, I learned a lot of things, physics, experimental techniques and especially how interesting the science is. And let me express my appreciation to the members of our lab, Dr. Ryota Takahashi, Dr. Mikko Matvejeff, Ms. Junko Kawamura, Mr. Kazunori Nishio, Mr. Tatsuya Kikuzuki, as well as the former members Dr. Tsuyoshi Ohnishi and Mr. Takuya Abe. Dr. R. Takahashi , Dr. M. Matvejeff and Mr. K. Nishio were supporting me in the tough stage of the experiments and always giving me important suggestions. Without their support, this thesis would not have taken shape either. And I cannot express my gratitude by words to my colleague, Mr. T. Kikuzuki, for his kind supports and encouragement. Also, let me express my special appreciations to Ms. J. Kawamura. She gave me infinite support in every aspect of the research and always encourage me. I express my sincere gratitude for her being a secretary of our laboratory.

Outside the lab, I appreciate Prof. Komori and his group members for their kind support of STM measurement. Also, I would like to thank Prof. Hasegawa and his group members for permission to use their AFM. For supporting magnetoresistance measurement in ISSP, I am really grateful to Dr. Toru Yamauchi and Dr. Hiroaki Ueda. I also appreciate Dr. Endo for helping with the angle-dependent magnetoresistance measurements. I would like to thank Dr. Christopher Bell and Mr. Yusuke Kozuka for helping with magnetoresistance measurements in their lab and for useful discussions. And I really would like to thank all my friends and people in ISSP for their kind support and encouragement.

Finally, I would like to express my deepest appreciation to all my family. Especially, my mother has always been supportive and encouraging me. I have learned many

things and received kindness from her. She made me what I am today. In addition, I cannot finish this thesis without appreciating to father, brother, grandmother and other family members. It would be impossible to have such a fruitful life in the graduate school without their warm encouragements and endless support.